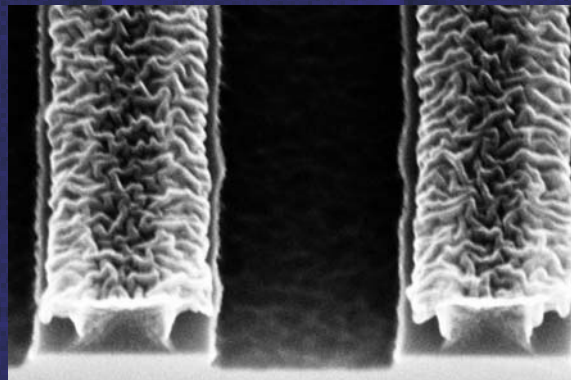
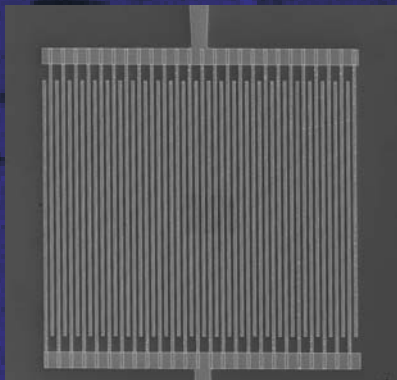


Lorenz Meier

Diss. ETH 17243
2007

Manipulation of electron spins in quantum wells with magnetic and electric fields



Diss. ETH No. 17243

Manipulation of electron spins in quantum wells with magnetic and electric fields

A dissertation submitted to

ETH ZÜRICH

for the degree of
Doctor of Sciences

presented by

Lorenz Meier

Dipl. Phys. ETH
born 11.03.1977
citizen of Bülach (ZH)

accepted on the recommendation of:

Prof. Dr. Klaus Ensslin, examiner
Prof. Dr. Atac Imamoglu, co-examiner
Dr. Gian Salis, co-examiner

2007

Zusammenfassung

Diese Doktorarbeit behandelt die Beeinflussung von Elektronenspins in einem GaAs/InGaAs Quantentopf. Die hier beschriebenen Experimente wurden im Rahmen eines gemeinsamen Forschungsprojekts zwischen dem IBM Forschungslaboratorium in Rüschlikon und der Gruppe für Nanophysik am Laboratorium für Festkörperphysik der ETH Zürich durchgeführt. Alle optischen Experimente wurden im IBM-Labor ausgeführt, Transportmessungen und die Probenherstellung an der ETH.

Die Arbeit beginnt mit einer Einführung in das Gebiet der ‘Spintronik’ und einer kurzen Übersicht über bisherige Erkenntnisse (Kapitel 1). In Kapitel 2 wird der experimentelle Aufbau samt dessen physikalischen Grundlagen sowie die Probenherstellung erläutert. Die Resultate sind aufgeteilt in drei Kapitel: Elektronenspinmanipulation mit magnetischen Feldern (Kapitel 3), mit magnetischen und elektrischen Feldern (Kapitel 4) und mit ausschliesslich elektrischen Feldern (Kapitel 5).

Kapitel 3 beschreibt die kohärente Präzession von Elektronenspins im magnetischen Streufeld unter einem Gitter aus Eisenstreifen in einem veränderlichen, externen Magnetfeld. Verglichen mit unter Streifen aus nichtmagnetischem Gold ist die Präzessionsfrequenz proportional zur Magnetisierung des Eisens erhöht, was wir auf das magnetische Streufeld der Eisenstreifen zurückführen. Indem wir benachbarte Eisenstreifen auf ein gegensätzliches elektrisches Potential setzen, bewegen wir die Elektronen im inhomogenen magnetischen Streufeld und können dadurch deren Präzessionsfrequenz verändern. Die Abstimmbarkeit beträgt ungefähr 0.5 GHz/V. Wenn wir die Spannung mit Gigahertz-Frequenzen modulieren, können wir die Spinpräzessionsfrequenz auf der Zeitskala von einer Nanosekunde beeinflussen.

In Kapitel 5 stellen wir eine neue Methode vor, welche die separate Bestimmung der Rashba- und Dresselhaus-Beiträge zum Spin-Bahn-Magnetfeld ermöglicht. Mittels eines externen elektrischen Wechselfeldes bringen wir die Elektronen in eine oszillierende Bewegung in der Ebene des Quantentopfs. Das Spin-Bahn-Magnetfeld, welches die Elektronen aufgrund ihrer Bewegung erfahren, hängt vom Winkel zwischen dieser Bewegung und dem Kristallgitter ab. Indem wir die Elektronenspinpräzessionsfrequenz als Funktion dieses Winkels messen, können wir das Spin-Bahnfeld und dessen Rashba- und Dresselhaus-Komponenten ermitteln. In einem weiteren Experiment verwenden wir Spin-Bahn-Felder, um Elektronenspinresonanz mit ausschliesslich elektrischen Feldern zu erzeugen.

Abstract

This thesis reports on the manipulation of electron spins confined in a GaAs/InGaAs quantum well. The experiments were performed in the frame of a joint-research project between the IBM Zurich Research Laboratory and the nanophysics group at the Laboratory for Solid State Physics at ETH Zürich. All optical experiments were conducted at the IBM lab, while transport measurements and sample processing were done at ETH.

After a general introduction into the field of spintronics and an overview on previous achievements (chapter 1), the experimental set-up including the underlying physical principles of the measurement techniques and the fabrication of the samples are described in chapter 2. The results of this thesis are split into three chapters, describing electron spin manipulation with only magnetic fields (chapter 3), with magnetic and electric fields (chapter 4) and with solely electric fields (chapter 5).

In chapter 3, the coherent precession of electron spins in the magnetic stray field below an array of Fe stripes is measured for varying external magnetic fields and stripe sizes. Comparing with reference stripes made of non-magnetic Au, we find an enhancement of the spin precession frequency proportional to the Fe magnetization, which we can attribute to the effect of the magnetic stray field emanating from the magnetized Fe bars. By applying a gate voltage to an interdigitated grating of Fe stripes (chapter 4), the electrons are moved within the inhomogeneous magnetic stray field and we achieve electrical control of the spin precession frequency, with a tunability on the order of 0.5 GHz/V. Modulating the gate voltage at gigahertz frequencies allows the spin precession to be controlled on a nanosecond timescale.

In chapter 5, we present a novel method that allows the separate determination of both Rashba and Dresselhaus contributions to the effective spin-orbit magnetic field. We use an external a.c. electric field to bring the electrons into an in-plane oscillatory motion. Depending on the orientation of this motion with respect to the crystal lattice, the electrons are subject to a varying spin-orbit magnetic field. By investigating the electron spin precession frequency as a function of their movement direction, the strength of the Rashba and Dresselhaus spin-orbit magnetic fields, and their coupling constants, can be extracted. In another experiment, we use these spin-orbit fields to trigger electron spin resonance with solely electric fields, in this context referred to as ‘electric-dipole-induced spin resonance’.

Contents

1	Introduction	1
1.1	Spintronics	1
1.2	Spin polarization	2
1.2.1	Optical spin orientation	2
1.2.2	Electrical spin injection	5
1.3	Spin detection	5
1.4	Spin relaxation mechanisms	6
1.4.1	Elliott–Yafet (EY)	6
1.4.2	D’yakonov–Perel’ (DP)	7
1.4.3	Bir–Aronov–Pikus (BAP)	8
1.4.4	Hyperfine interaction	8
1.4.5	Spin relaxation in GaAs	8
1.5	Spin manipulation	9
1.5.1	Spin manipulation with local magnetic fields	9
1.5.2	Spin manipulation with electric fields	10
2	Experimental techniques	11
2.1	Time-resolved Faraday rotation	11
2.1.1	Pumping the spins	11
2.1.2	Probing the spins	12
2.1.3	Time-resolved technique	14
2.2	Optical setup	15
2.2.1	Laser system	16
2.2.2	Delay line	16
2.2.3	Obtaining the polarizations	16
2.2.4	Detecting the rotated polarization	17
2.3	Electronics	20

2.3.1	Photodiode box	20
2.3.2	Auto-balancing the bridge	20
2.4	Cryogenics	22
2.4.1	Cryostat	22
2.4.2	Auto-centering the sample	22
2.5	Quantum well samples	23
2.5.1	Basic wafer layer sequence	24
2.5.2	MOCVD-samples	24
2.5.3	MBE-samples	29
2.5.4	Van der Pauw technique	31
2.6	Sample processing	32
2.6.1	Electron beam lithography	32
2.6.2	Gate evaporation	33
2.6.3	Etching	34
3	Spin manipulation with magnetic fields	36
3.1	Introduction and motivation	36
3.2	Previous work on magnetic stray fields	38
3.2.1	Detection of magnetic stray fields	38
3.2.2	Electrical control of spin dynamics	38
3.3	Numerical field simulations	39
3.3.1	Magnetization simulations	41
3.3.2	Stray field simulations	41
3.4	Stray field measurements on ferromagnetic gratings	43
3.4.1	Measurement setup	43
3.4.2	Expectations from numerical simulations	45
3.4.3	Measurement of stray-field-induced modification of spin dynamics	47
3.4.4	Effects of nuclear polarization and nuclear imprinting	50
3.4.5	Optical diffraction at the grating	53
3.4.6	Gratings with larger gap than bar size	54
3.4.7	Horizontal and vertical gratings	57
3.4.8	Spatially resolved measurements	58
3.5	Stray field measurements on etched gratings	58
4	Spin manipulation with magnetic and electric fields	62
4.1	Gated gratings	62

4.1.1	Overview	62
4.1.2	Sweeps of B_{ext} at different gate voltages	63
4.1.3	Gate sweeps at constant magnetic field	65
4.1.4	Horizontal and vertical gratings	70
4.1.5	Spatially resolved measurements on gated gratings	70
4.2	Oscillating gate voltages	73
4.2.1	Introduction and electronic set-up	73
4.2.2	Electron precession frequency as a function of laser-gate delay	75
4.2.3	Dependence on d.c. gate voltage	75
4.2.4	A.c. effects beside a grating	78
5	Spin manipulation with electric fields	80
5.1	Introduction to spin-orbit interaction	80
5.1.1	Rashba spin-orbit term (SIA)	81
5.1.2	Dresselhaus spin-orbit term (BIA)	82
5.2	Measurement of Rashba and Dresselhaus fields	83
5.2.1	Geometrical properties of Rashba and Dresselhaus spin-orbit fields	83
5.2.2	Measurement set-up	84
5.2.3	ν as a function of time	86
5.2.4	ν as a function of φ and θ	86
5.2.5	Determination of the electric field between the gate electrodes	90
5.3	Spatially resolved measurements	92
5.3.1	Large-area scans	92
5.3.2	Scans with a rotating electric field	95
5.4	Electric-dipole-induced spin resonance	97
5.4.1	Introduction and results	97
5.4.2	Comparison with Bloch equations	99
6	Outlook	100
6.1	Summary	100
6.2	Open questions	100
6.3	Suggestions for further experiments	101
6.3.1	Imaging magnetic stray fields	101
6.3.2	Spin-orbit-interaction-related experiments	101
	Appendices	105

A	Time-resolved photoluminescence measurements	105
B	Spin-orbit splitting with k^3 -dependence	108
C	Tunability of the spin-orbit interaction?	109
D	Verification of the sample magnetization	112
E	List of samples	114
Publications		116
Bibliography		118
Acknowledgements		125
Curriculum Vitae		127

List of symbols

Symbol	Explanation
α	Rashba coupling constant
β	Dresselhaus linear coupling constant
γ	Dresselhaus cubic coupling constant
B	magnetic field
B_{ext}	external magnetic field
B_n	effective nuclear magnetic field
B_s	magnetic stray field
B_{so}	effective spin-orbit magnetic field
B_{BIA}	bulk inversion asymmetry effective magnetic field
B_{SIA}	structure inversion asymmetry effective magnetic field
c	velocity of light (299 792 458 m/s)
\mathcal{E}	‘intrinsic’ electric field
e	electron charge (1.6022×10^{-19} C)
E	external electric field
E_g	band gap energy
ϵ_0	dielectric constant (8.8542×10^{-12} F/m)
ϵ	relative dielectric constant (13 for GaAs)
f	frequency of an external field
g	effective Landé g -factor (-0.44 in GaAs)
$h = 2\pi\hbar$	Planck’s constant (6.6261×10^{-19} Js)
I	current
λ	(laser) wavelength
m	electron mass (9.1094×10^{-31} kg)
m^*	effective electron mass in GaAs ($0.067m$)
μ	electron mobility
μ_B	Bohr magneton (927.40×10^{-26} J/T)
n	refractive index
P	power
R	resistance
t	time
T	temperature
T_1	(longitudinal) spin lifetime
T_2	spin coherence time
T_2^*	spin coherence time of a spin ensemble
$\Delta\tau$	pump-probe delay
τ_r (τ_h)	electron (hole) recombination time
τ_s	spin lifetime (T_1 or T_2)
θ_F	Faraday rotation angle
V_g	gate voltage
ν	spin precession frequency

Chapter 1

Introduction

This introductory chapter presents major achievements and future visions within the field of spin electronics (Sect. 1.1) and it introduces important methods for the manipulation of electron spins, such as spin polarization (Sect. 1.2) and spin detection (Sect. 1.3). The processes leading to spin relaxation are described in Sect. 1.4, and the two basic concepts for spin manipulation pursued in this thesis are introduced in Sect. 1.5.

1.1 Spintronics

In present computers, information is processed by the use of charge currents. Usually, electrons carry this charge. An additional quantum-mechanical property of the electron, the spin, remains unused, since the computation relies only on classical physics. With the ongoing miniaturization of integrated circuits in the semiconductor industry [1], the need for alternative technologies is obvious, if the progress in computational power and reduction in size, often illustrated by Moore's law [2], is to be continued in the upcoming decades.

Since the discovery of the electron spin, first mentioned by Pauli in the formulation of his exclusion principle [3] in 1925, physicists have been fascinated by this quantum-mechanical property of particles, in particular of electrons. The prospect of potential applications in future quantum computers [4, 5] has led to exciting research, predominantly of fundamental nature. The term 'spintronics' has evolved from the words 'spin' and 'electronics' and describes the use of the electron spin degree of freedom in a solid-state environment. While most experiments still deal with spin ensembles of 10^3 to 10^5 electrons, electrical [6–8] and optical [9, 10] access to single electron spins confined in quantum dots has recently been reported.

Already today, spintronic devices are widely employed in read-heads of hard-disk drives. The discovery of the giant magnetoresistance effect (GMR) [11–13] in 1988 has led to an increase of the information storage density in hard-disk drives by

more than one order of magnitude. In a GMR–device, a non-magnetic, conducting layer is embedded between two magnetized layers. The in-plane resistance depends on whether the two magnetic layers are magnetized in a parallel or an anti-parallel configuration. A difference of up to a factor 2 has been found. If the magnetic layers have different coercive fields, an external magnetic field, e.g. from a magnetized domain on the hard disk, can switch the device into the parallel or anti-parallel state. This operation is also referred to as ‘spin valve’. Another readily available application is the ‘magneto-resistive random access memory’ (MRAM) that uses the tunneling magnetoresistance effect (TMR) [14, 15], which is similar to GMR, except that the middle layer is non-conducting. In that case, a current is passed perpendicularly through the layers, and quantum-mechanical tunneling through the non-conducting layer occurs. Also here, the tunneling resistance changes if the magnetic layers are aligned parallel or anti-parallel.

Future applications of spintronic devices include the use of single electron spins as quantum–bits (qubits) for a quantum-computer [16]. Such a computer could perform certain operations exponentially faster than a classical computer, like the factorization of integer numbers [17]. Because of their potentially long coherence times [18], much larger than the charge (orbital) coherence time, such qubits could fulfill the requirement of retaining their coherence over at least 10^4 computation cycles [19]. At the same time, this is also their Achilles’ heel: interacting only weakly with the environment, the manipulation and state–preparation of a spin–qubit is difficult.

In the following sections, we give a short introduction on how to polarize, manipulate, and detect electron spins. More detailed reviews can be found in [20–22].

1.2 Spin polarization

In ferromagnetic materials, an equilibrium spin polarization exists. Spintronic applications, however, often require the generation of a non–equilibrium spin polarization. Historically, such a spin pumping was achieved with optical techniques. For solid–state applications, however, electrical spin injection without the need for optics might be advantageous.

1.2.1 Optical spin orientation

The first experimental proof of optical spin orientation in a semiconductor (Si) was reported in 1968 by Lampel [23]. Since then, this process has been extensively studied and is well understood [24]. In the process of optical excitation, a photon creates an electron in the conduction band and leaves a hole in the valence band. What kind of optical polarization is needed and which amount of spin polarization

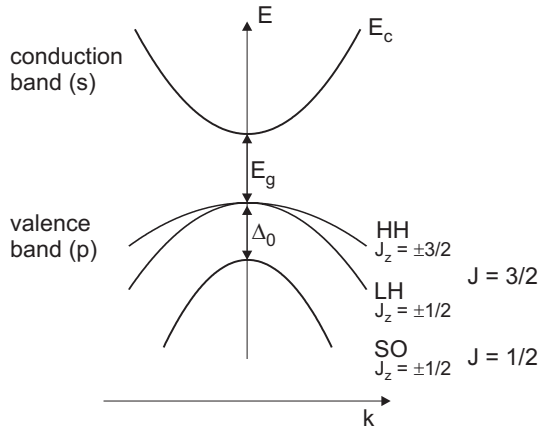


Figure 1.1: Band structure of GaAs with simplified parabolic bands near the Γ -point. HH, LH and SO denote the heavy-hole, light-hole and split-off bands. E_g is the band gap, Δ_0 the spin-orbit splitting.

can be achieved is governed by the semiconductor's band structure and the selection rules. In a GaAs system as studied in this thesis, a spin polarization of 50% (100% if the system is two-dimensional) can be achieved using circularly polarized light. Since the electric field of the photon does not interact directly with the spin but with the electron's orbital motion, spin polarization is only possible with the help of spin-orbit coupling. From the band structure of GaAs in Fig. 1.1 this coupling is visible in the valence band. Contrary to the conduction band, which has s -orbital symmetry, the orbital momentum of the p -type valence band is $L = 1$. Together with the spin $S = 1/2$, the total angular momentum is $J = 3/2$ in the light- (LH) and heavy-hole (HH) bands and $J = 1/2$ in the split-off (SO) band. Electrons are preferably excited from the HH band to the conduction band with circularly polarized light tuned to the band-gap energy E_g . Since HH and LH bands are degenerate at $k = 0$ (this degeneracy is lifted in reduced dimensions), electrons from both bands are excited, resulting in a spin polarization of less than 100% (see Sect. 2.1.1). If the energy of the exciting radiation exceeds $E_g + \Delta_0$, also electrons from the SO band contribute. These transitions lead to a spin polarization opposite in sign of the HH transition and therefore, the spin polarization in the conduction band vanishes.

Optically excited carriers have a finite lifetime, also called recombination time, τ_r . The number of recombining electron-hole pairs per time is given by

$$\dot{N}(t) = \frac{dN(t)}{dt} = -\frac{N(t)}{\tau_r}, \quad (1.1)$$

where $N(t)$ is the total number of optically excited electrons at time t and $N_0 = N(t = 0)$. Then, $N(t)$ decays exponentially

$$N(t) = N_0 \exp\left(-\frac{t}{\tau_r}\right). \quad (1.2)$$

A spin polarized population N_s decays in a similar way, but now there are two decay channels available. A spin can either recombine to 'leave' the ensemble N_s , or it can

lose its spin orientation after a spin relaxation time τ_s . Both losses add up to yield

$$\frac{dN_s(t)}{dt} = - \left(\frac{N_s(t)}{\tau_r} + \frac{N_s(t)}{\tau_s} \right), \quad (1.3)$$

and

$$N_s(t) = N_{s,0} \exp \left(- \left(\frac{1}{\tau_r} + \frac{1}{\tau_s} \right) t \right) = N_{s,0} \exp \left(- \frac{t}{\tau} \right), \quad (1.4)$$

with $N_{s,0} = N_s(t=0)$ the number of spin polarized electrons at $t=0$ and the new lifetime

$$\tau = \left(\frac{1}{\tau_r} + \frac{1}{\tau_s} \right)^{-1}. \quad (1.5)$$

In an undoped semiconductor, the measurement of spin dynamics is thus limited by the recombination time τ_r .

This limitation can be overcome by using n -doped samples, where an equilibrium electron concentration N_d is present in the conduction band. Up to now, we have only considered spin-polarized electrons. However, for every optically excited electron, a spin-polarized hole with opposite spin is created in the valence band. As explained in [25], the hole spin relaxes quickly on the time scale of the momentum relaxation time, due to the strong spin-orbit coupling in the valence band¹. Therefore, we can safely assume that electron-hole recombination is independent of the electron spin. Assuming 100% electron polarization by the optical excitation, at $t=0$, $N_{h,0} = N_{s,0}$ holes are created and their decay is solely governed by τ_r , such that $N_h(t) = N_{s,0} \exp(-t/\tau_r)$. We split the population of the conduction band in unpolarized electrons N_u and spin-polarized electrons N_s . At $t=0$, $N_u = N_d$, and N_s is determined by the pump-pulse power and wavelength according to Eq. (2.7) below. The decay rates are then given by

$$\begin{aligned} \dot{N}_s(t) &= \frac{N_s(t)}{N_s(t) + N_u(t)} \dot{N}_h(t) - \frac{N_s(t)}{\tau_s}, \text{ and} \\ \dot{N}_u(t) &= \frac{N_u(t)}{N_s(t) + N_u(t)} \dot{N}_h(t) + \frac{N_s(t)}{\tau_s}. \end{aligned} \quad (1.6)$$

We have assumed that polarized and unpolarized electrons recombine proportionally to their occurrence in the conduction band and that the polarized electrons additionally decay with their spin relaxation rate – in which case they become unpolarized and have to be added to N_u . Additionally, charge has to be conserved,

$$N_u(t) + N_s(t) - N_h(t) = N_d. \quad (1.7)$$

By solving Eq. (1.7) for $N_u(t)$ and substituting it into either expression of Eq. (1.6),

¹This relaxation can be suppressed in deformed GaAs crystals.

we obtain together with the exponential decay of N_h given above,

$$\begin{aligned}\dot{N}_s(t) &= \frac{N_s(t)}{N_d + N_h(t)} \dot{N}_h(t) - \frac{N_s(t)}{\tau_s} \\ &= -\frac{N_s(t)}{\tau_r} \left(1 + \frac{N_d}{N_{s,0}} \exp\left(\frac{t}{\tau_r}\right) \right)^{-1} - \frac{N_s(t)}{\tau_s}.\end{aligned}\tag{1.8}$$

Comparing with Eq. (1.3), the relaxation rate due to recombination is effectively reduced by a factor $1 + \exp(t/\tau_r)N_d/N_{s,0} > 1$. In our experiments, $N_d/N_{s,0} = 10^2 \dots 10^3$ and the spin relaxation is not limited by the recombination time $\tau_r \approx 400$ ps (see appendix A).

1.2.2 Electrical spin injection

In a ferromagnet, electrons are partially spin-polarized. Therefore, a ferromagnetic contact could serve as a spin injector into a semiconductor, as proposed in 1976 [26].

The most straight-forward approach might be spin-injection via an Ohmic contact. This, however, has proven difficult. Polarizations of only a few percent have been observed [27], which was attributed to spin-flip scattering at the interface [28].

As a solution to this, a magnetic semiconductor layer was introduced as spin aligner between the Ohmic contact to a metal and the semiconductor. Magnetic semiconductors are usually grown by a diluted doping (a few percent) of II-VI-semiconductors (e.g., CdTe or ZnSe) with Mn. This results in a large Zeeman-splitting due to a high electron g -factor (up to ≈ 100) and leads to spin-polarization in the conductance band already at small external magnetic fields. With this approach, much higher injection efficiencies were reported [29, 30]. A similar approach has also been realized [31] with GaMnAs, a ferromagnetic p -type semiconductor [32].

The most efficient spin injection today, however, has been achieved by tunneling. Already in 1992, spin injection from a ferromagnetic STM-tip into GaAs has been observed [33]. Today, injection efficiencies of up to 70% have been reported by tunneling from a ferromagnet (CoFe) via a MgO tunnel barrier into GaAs [34, 35].

1.3 Spin detection

As a means of reading out the spin state of a qubit or in order to verify the amount of injected spin polarization, a spin detection scheme has to be implemented. Again, both optical and electrical detection mechanisms can be adopted. Optical detection relies on the analysis of the polarization state of the radiation emitted by recombining electrons. If a recombining electron is spin-polarized, the radiation in general is circularly polarized. Such an optical detection, however, requires the recombination

time to be shorter than the spin relaxation time. Otherwise (e.g. in indirect-band semiconductors), the spin has already relaxed at the time the radiation is emitted. Optical detection can be combined with electrical injection, as demonstrated in a ‘spin-LED’ [30]. Such a light-emitting diode produces circularly polarized light. Another method of optical spin detection is the Hanle effect, where the spins precess in a magnetic field transverse to their orientation (first semiconductor measurement in 1969 on GaSb [36]). This method has the advantage that also τ_s can be determined. Electrical spin detection relies on the TMR principle mentioned above in Sect. 1.1 [37].

Of course, there are many other paths that lead to the detection of polarized electrons. In the pioneering work by Lampel [23], the optically induced electron polarization was revealed by nuclear magnetic resonance (NMR). As explained below (Sect. 3.4.4), the interaction between polarized electrons and nuclear spins can lead to polarization of the nuclei, which in turn can generate large nuclear magnetic fields.

1.4 Spin relaxation mechanisms

Spin manipulation has to occur within a time when the spin is still oriented. Therefore, before introducing spin manipulation techniques, we briefly discuss the main spin relaxation mechanisms. Detailed calculations can be found in [24], a well comprehensible overview in [38]. Spin relaxation and decoherence are complex processes, but for most applications, they can be summarized by the two parameters T_1 and T_2 , which appear in the phenomenological Bloch equations, Eq. (5.19). T_1 is the time it takes for the spin to reach thermal equilibrium by aligning with the longitudinal magnetization. In this process, energy is exchanged with the lattice. In contrast, T_2 is the transverse spin relaxation or spin coherence time and describes the time over which the phase of a superposition of two states $|0\rangle$ and $|1\rangle$, usually spin-up and spin-down, is well defined and the off-diagonal matrix elements in the density matrix are non-zero. When measuring spin ensembles, T_2 is further reduced by averaging effects, such as fluctuating microscopic magnetic fields from nuclei or from spin-orbit coupling, that can all be summarized in a distribution of g -factors with nonzero width Δg . The additional decoherence is on the order of $\tau^{-1} \approx \Delta g \mu_B B / \hbar$. The observed spin coherence time of an ensemble is often denoted by T_2^* , with $T_2^* \leq T_2$ and $T_2 \leq 2T_1$ [39]. In the following, we will denote the spin relaxation by τ_s . Depending on the experiment and the geometry, τ_s corresponds to T_1 or (in most cases) T_2 .

1.4.1 Elliott–Yafet (EY)

The Elliott–Yafet relaxation mechanism was pointed out by Elliott in 1954 [40] and Yafet in 1963 [39]. It was shown that spin-orbit interaction in crystals causes a

mixing of wave functions with spin-up and spin-down orientations, i.e. that the wave function for a spin-up electron also contains (usually small) contributions of a spin-down wave function. Therefore, spin-independent momentum scattering with impurities (at low T), interfaces and phonons (at high T) can also lead to spin relaxation. The spin relaxation rate τ_s^{-1} due to the EY-mechanism is therefore proportional to the momentum relaxation rate τ_p^{-1} ,

$$\frac{1}{\tau_s} \propto \frac{1}{\tau_p}.$$

1.4.2 D'yakonov–Perel' (DP)

Another spin relaxation mechanism was discovered by D'Yakonov and Perel' in 1971 [41]. Due to spin-orbit coupling in the conduction band (see Sect. 5.1), in crystals without an inversion center (for example in GaAs), the spin degeneracy at $\mathbf{k} \neq 0$ is lifted, since the electrons feel a \mathbf{k} -dependent magnetic field, which couples to their spin. The spin starts to precess about a \mathbf{k} -dependent axis $\mathbf{\Omega}(\mathbf{k})$. Both the direction and the magnitude of $\mathbf{\Omega}$ depend on the electron momentum \mathbf{k} , as described later in Eq. (5.4). Because \mathbf{k} changes after the momentum scattering time τ_p , also $\mathbf{\Omega}(\mathbf{k})$ will be modified and we consider two limiting cases.

If the average spin precession Ω_{avg} about $\mathbf{\Omega}$ is faster than the momentum scattering, i.e. $1/\Omega_{\text{avg}} < \tau_p$, the transverse spin component of a spin ensemble vanishes before the first momentum scattering event, since all electron spins precess about different $\mathbf{\Omega}$, due to randomly distributed \mathbf{k} in the ensemble. In this case, the spin relaxation rate is proportional to the width $\Delta\Omega$ of the distribution, $\tau_s^{-1} \approx \Delta\Omega$.

The opposite limit $1/\Omega_{\text{avg}} > \tau_p$ considers the case that momentum scattering occurs faster than spin precession. In general, this is the important limit for GaAs. In this case, the spins start to precess about $\mathbf{\Omega}(\mathbf{k})$, but before having rotated considerably ($\Omega_{\text{avg}}\tau_p < 1$), the electron scatters into a new momentum state \mathbf{k}' and the spin precesses about a new $\mathbf{\Omega}(\mathbf{k}')$. This is equivalent to a random walk in two dimensions, with step size $\delta\phi = \Omega_{\text{avg}}\tau_p$. After a time t and t/τ_p steps, $\Delta\phi_{\text{rms}}(t) \approx \delta\phi\sqrt{t/\tau_p}$, like in a diffusive process. With the usual definition $\Delta\phi_{\text{rms}}(\tau_s) = 1$, we find $\tau_s^{-1} = \Omega_{\text{avg}}^2\tau_p$. This effect is also called ‘motional narrowing’. In summary, the spin relaxation by the D'yakonov–Perel' mechanism is inversely proportional to the momentum relaxation rate,

$$\frac{1}{\tau_s} \propto \tau_p.$$

1.4.3 Bir–Aronov–Pikus (BAP)

The Bir–Aronov–Pikus relaxation mechanism [42] (1975) is important in semiconductors where electron and hole wave functions have large overlap. Due to the exchange interaction between electron and hole, the electron spin perceives an effective magnetic field about which it starts to precess. As mentioned above, hole spins relax much faster than electron spins and therefore, the electron spin feels a fluctuating field and again the effect of ‘motional narrowing’ reduces the relaxation rate induced by this mechanism, and the spin relaxation rate is proportional to the hole relaxation time, $\tau_s^{-1} \propto \tau_h$.

1.4.4 Hyperfine interaction

Electron and nuclear spins interact via the contact hyperfine interaction, which leads to an effective magnetic field B_n proportional to the magnitude squared of the electron wave function at the positions of the nuclei. While this interaction is too weak to cause considerable relaxation of free electrons in bulk semiconductors, it is important for localized electrons confined in quantum dots. In GaAs, where the nuclei carry a spin of $3/2$, these electrons typically interact with $10^4 - 10^6$ nuclei [20]. Fluctuations of B_n in space and time lead to decoherence of both spin ensembles and single spins.

1.4.5 Spin relaxation in GaAs

In bulk n -type GaAs, it is agreed that EY and DP are the dominant spin relaxation mechanisms. Since their relaxation efficiencies are proportional to τ_p^{-1} for EY and to τ_p for DP, their contributions can be distinguished in the experiment by deriving τ_p from, for example, mobility measurements. It was found [43] that EY is dominant at low T and DP at high T , with a transition around $T = 30$ K. Moreover, a strong dependence of the spin lifetime on doping density and magnetic field was reported. The lifetime was found to be largest for doping densities between 3×10^{15} and $2 \times 10^{16} \text{ cm}^{-3}$, the upper limit was associated with a metal–insulator transition [44]. The BAP relaxation mechanism is only relevant in p -type GaAs.

In quantum wells, the situation is more complicated due to higher mobilities, smaller electron–hole separation and a more complicated band structure. Generally, the spin relaxation time is lower than in bulk GaAs [45], but theoretical explanations are controversial (see [38] for an overview). Long τ_s on the order of nanoseconds were observed up to room temperature [46] in (110)-grown GaAs. This was ascribed to a suppression of the DP-mechanism in this geometry.

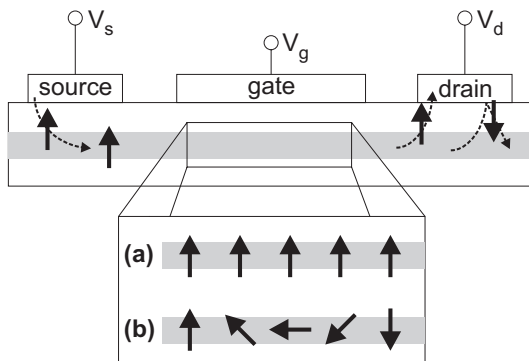


Figure 1.2: A spin transistor is thought to work similarly to a field-effect transistor. A spin-polarized current is injected via the source electrode. Below the gate, the spin polarization remains (a) unchanged or is (b) rotated. Only the spin-up orientation can pass the drain contact, spin-down is reflected back.

1.5 Spin manipulation

By the term ‘spin manipulation’ we name the intentional change of the orientation of one or several spins. Figure 1.2 shows a ‘spin transistor’, proposed by [Datta and Das \(1990\)](#) [47] and yet unrealized. An electron spin is polarized and injected from a ferromagnetic source contact into a one-dimensional channel. In the channel, the spin is manipulated and at the drain contact, the spin is detected by another ferromagnet. Only one spin orientation can pass the interface to the contact, the other orientation is reflected back into the channel (analogous to a TMR-device). In the original proposal, the spin orientation in the channel was manipulated using spin-orbit fields. Besides spin-orbit effects, other approaches for spin manipulation are considered, as described in the next section.

In the following, we give short introductions to spin manipulation, for example in the channel of a spin transistor, using magnetic and electric fields. We focus on magnetic stray fields and on spin-orbit interaction. In both cases, the aim is to control the electron spin by electric fields, since they are easy to apply locally using gate electrodes.

1.5.1 Spin manipulation with local magnetic fields

The most straight-forward approach to manipulate an electron spin is the use of a magnetic field, since the magnetic moment of a spin, $\mu = g\mu_B\mathbf{S}$ couples directly to the magnetic field \mathbf{B} via a Zeemann-term $\mathbf{S} \cdot \mathbf{B}$ in the Hamiltonian. With g -factor-engineered heterostructures [48, 49], spins can be selectively transferred into an area of high g -factor and manipulated there.

If the magnetic field \mathbf{B} is a local field, for example confined to the size of a quantum dot, only the spin(s) in this dot are influenced by \mathbf{B} . This is the case for magnetic stray fields of, for example, ferromagnetic gate electrodes. This approach has the advantage of rather high magnetic fields (up to ≈ 1 T), which are confined to small length scales, since the stray field is strongly inhomogeneous and decays

on the length scale of the magnetized gate electrode. In chapter 3, we present investigations on the magnitude and spatial distribution of magnetic stray fields and on their influence on the electron spin precession. By spatially displacing the electrons within the inhomogeneous stray field, the spin precession frequency changes and electrical control on the spin precession is achieved. This is demonstrated in the chapter 4.

1.5.2 Spin manipulation with electric fields

It is even possible to manipulate electron spins without the use of magnetic fields. Owing to a relativistic effect, magnetic and electric fields transform into each other by the Lorentz transformation. In the frame of an observer at rest, a moving charge will generate a magnetic field. If, however, the observer moves together with the charge, only an electric field is measured. For a charge moving at a velocity \mathbf{v} , an electric field \mathcal{E} will transform into a magnetic field [50]

$$\mathbf{B} = \mathbf{v} \times \frac{1}{c^2} \mathcal{E} \quad (1.9)$$

In a semiconductor, the electric field \mathcal{E} either originates from the asymmetric arrangement of atoms in the crystal (Dresselhaus term [51]) or from the interface of heterostructures and externally applied fields perpendicular to the layers (Rashba term [52, 53]). The interaction of the resulting magnetic field with a spin is called spin-orbit interaction. The magnetic fields resulting from Dresselhaus and Rashba terms have a different dependence on \mathbf{v} and are usually different in magnitude. Depending on the direction of \mathbf{v} with respect to the crystal lattice, both fields add up to a total field and the Dresselhaus and Rashba components can be extracted, as shown in chapter 5. Due to their similar magnitude in the samples used, both spin-orbit fields virtually cancel for some directions of \mathbf{v} , allowing for spin manipulation by controlling the electron direction of movement [54]. If the movement is oscillatory, also the spin-orbit magnetic fields oscillate and can be used to induce spin resonance, see Sect. 5.4.

Chapter 2

Experimental techniques

This chapter describes the experimental techniques and the samples used in the experiments. We start with an introduction to time-resolved Faraday rotation (Sect. 2.1) and continue with a detailed description of the optical setup (Sect. 2.2). In Sect. 2.3 we describe the electronic devices that were built to perform the measurements and in Sect. 2.4 we introduce the cryogenic equipment. The chapter ends with a detailed description and characterization of the samples that were grown in the course of this work (Sect. 2.5) and the clean-room processes used (Sect. 2.6).

2.1 Time-resolved Faraday rotation

The ‘working horse’ used in most of the experiments presented in this thesis is the technique of time-resolved Faraday rotation (TRFR). This pump-probe tool allows the observation of spin dynamics in semiconductors. Most of the time, we use it in the *Voigt* geometry, where an external magnetic field \mathbf{B}_{ext} is in-plane with the probed quantum well (QW), and perpendicular to the laser beam. If the laser is parallel to the magnetic field and perpendicular to the sample surface, this is called the *Faraday* geometry (see Sect. 5.4).

2.1.1 Pumping the spins

Optically generating a spin polarization in the conduction band of a semiconductor is simple, as long as optical selection rules allow the addressing of spin polarized states by polarized light. In GaAs, the band structure is well known (Fig. 1.1): a *s*-type conduction band and a *p*-type valence band. The latter consists of three (in the vicinity of the Γ -point parabolic) subbands, the heavy- and light-hole bands, which are degenerate at $k = 0$ and the split-off band, which is lowered in energy by the spin-orbit splitting Δ_0 .

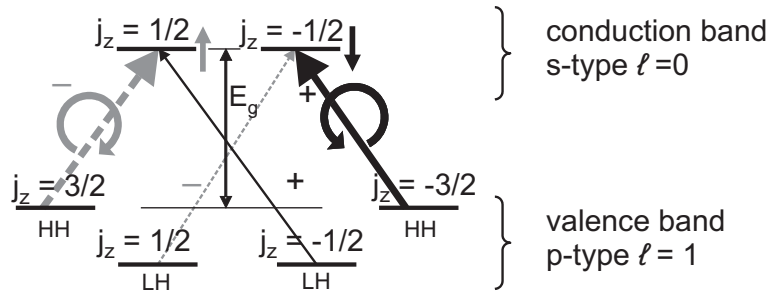


Figure 2.1: Simplified QW band structure with the transitions induced by right- (σ^+) and left- (σ^-) circularly polarized light, allowed by optical selection rules. E_g denotes the band gap, j_z the projection of the total angular momentum J on the z -axis. HH = heavy-hole band, LH = light-hole band. The transitions indicated by thin arrows are 3 times less likely than those shown by bold arrows.

In a GaAs QW, even light and heavy hole states are split (Fig. 2.1). For the heavy-hole band, the projection of the angular momentum on the z -direction is $j_z = \pm 3/2$. Since the valence band is p -type, the orbital angular momentum is $L = 1$ and in the heavy-hole subband, spin ($S_z = \pm 1/2$) and orbital angular momentum ($m = \pm 1$) are parallel. The optical selection rules demand $\Delta m = \pm 1$ (for the circular polarizations σ^{\pm}) so that the $j_z = \pm 1/2$ states in the conduction band can be populated by exciting carriers from the heavy-hole band with right- or left circularly polarized light. The spin polarization amounts to 100% and is ‘spin up’ ($S_z = j_z = 1/2$) for left circularly polarized light and ‘spin down’ ($S_z = j_z = -1/2$) for right circularly polarized light.

Even in bulk samples, an optically induced spin polarization is possible. However, since light- and heavy-hole states at zero wave vector are degenerate, also electrons from the light-hole band with $j_z = \pm 1/2$ are excited. These states are each a superposition of the two states $(m, S_z) = (0, \pm 1/2)$ and $(\pm 1, \mp 1/2)$, and therefore, a σ^- -excitation also reaches the $j_z = -1/2$ state in the conduction band (and σ^+ the $j_z = 1/2$ state). However, these transitions are by a factor 3 less likely than the transitions from the heavy-hole band and a spin polarization of $(3-1)/(3+1) = 50\%$ can be achieved.

2.1.2 Probing the spins

If an additional electron-spin of the majority spin orientation (spin-up in Fig. 2.2) is added to a polarized spin ensemble, it has to be added to a state higher in energy than an additional electron spin belonging to the minority spin-orientation, because of the Pauli principle. Hence, two Fermi energies exist for spin-up and spin-down electrons, also called ‘selective state-filling’. Therefore, the absorption edge for an incoming photon is split in energy for σ^+ and σ^- -polarizations [55] (Fig. 2.3a), and

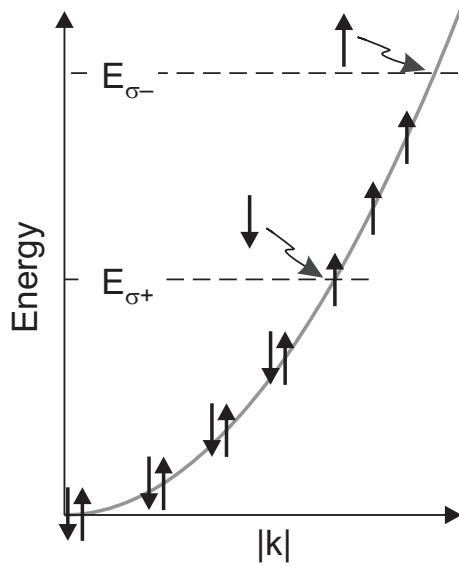


Figure 2.2: Different absorption energies originate from the fact that free states are available at different energies for spin-up and spin-down electrons. Hence, σ^- -polarized light, which excites a spin-up electron, experiences a higher absorption edge than σ^+ -polarized light, whose excited spin-down electrons can fill up states at lower energies.

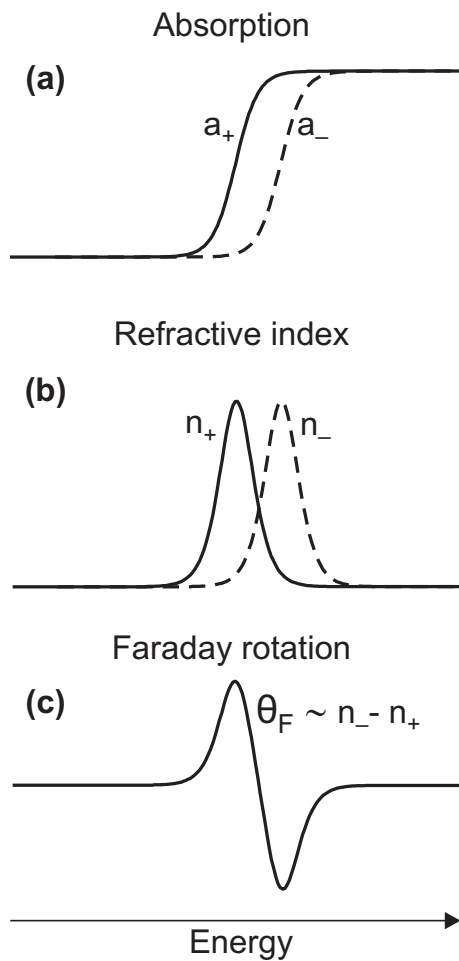


Figure 2.3: Absorption, refractive index and Faraday rotation as a function of exciting energy. (a) Right and left circularly polarized light experience a different absorption edge, and therefore, (b), a different refractive index. (c) The Faraday rotation angle θ_F is proportional to $n_- - n_+$.

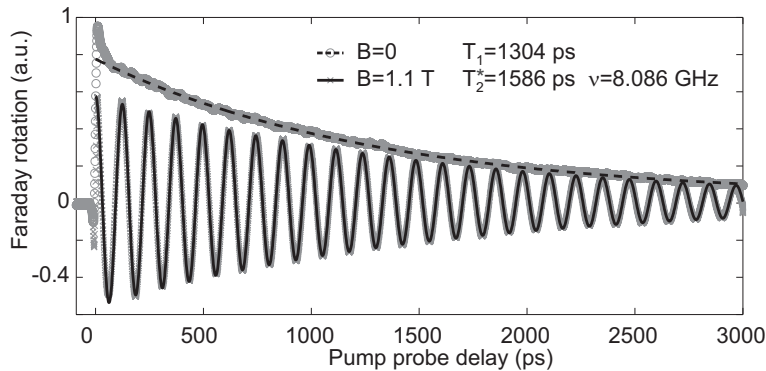


Figure 2.4: Faraday rotation measurement in the Voigt geometry on a GaAs/InGaAs QW with and without an in-plane magnetic field. Solid and dashed lines are fits to the data.

with it also the refractive index¹ (Fig. 2.3b). Linearly polarized light can be written as a superposition of σ^+ and σ^- , and therefore each component acquires a different phase shift due to this circular birefringence, resulting in elliptically polarized light. For small phase shifts, the ellipticity is small and the polarization plane of the linearly polarized light is rotated [56]. The rotation angle θ_F is proportional to the spin polarization along the laser direction.

2.1.3 Time-resolved technique

With a pulsed laser, the pumping and probing of the spins can be performed in a repetitive measurement, where the delay between pump- and probe-pulse is varied. A first, circularly polarized pump pulse creates a spin polarization S_z in the conduction band, perpendicular to the sample surface and in direction of the laser beam. A second, linearly polarized probe pulse arrives with a time delay $\Delta\tau$ on the sample and is rotated by $\theta_F \propto S_z$. Monitoring $\theta_F(\Delta\tau)$ reveals two essential properties of the spin polarized electron ensemble:

- In the Voigt geometry, the spin coherence time T_2^* (also called transverse spin lifetime) or the longitudinal spin lifetime T_1 in Faraday geometry. For $B = 0$, also T_1 is measured.
- The spin precession frequency ν in a magnetic field perpendicular to the spin polarization.

Both numbers can be extracted by fitting $\theta_F(\Delta\tau)$ to

$$\theta_F(\Delta\tau) = \theta_0 e^{-\Delta\tau/\tau_s} \cos(2\pi\nu\Delta\tau), \quad (2.1)$$

¹Absorption and refractive index are connected by the *Kramers-Kronig* relation [50].

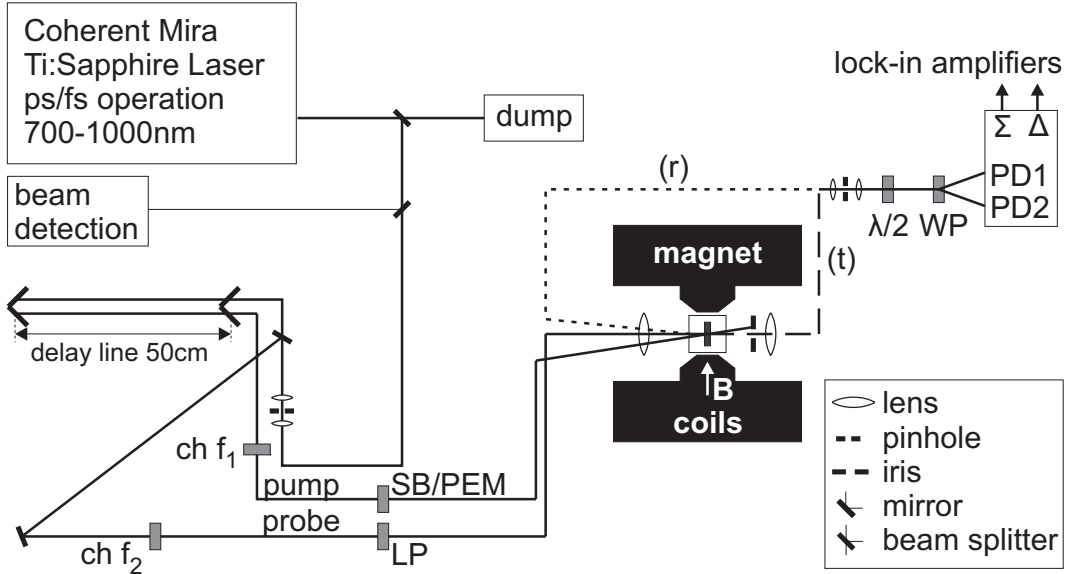


Figure 2.5: Optical setup, see text for details. LP = linear polarizer, PEM = photoelastic modulator, SB = Soleil-Babinet circular polarizer, ch = chopper at frequency f_1 or f_2 , WP = Wollstone prism.

where τ_s stands for T_2^* or T_1 , depending on the geometry and the oscillatory term is only included in the Voigt geometry at $B \neq 0$. Figure 2.4 shows two TRFR scans with and without magnetic field and the corresponding fits to Eq. (2.1). From ν , the magnitude of the magnetic field can be extracted via

$$\nu = \frac{g\mu_B B}{h}, \quad (2.2)$$

where g is the (effective) electron g -factor, μ_B Bohr's magneton and $h = 2\pi\hbar$ Planck's constant.

2.2 Optical setup

A simplified view from above on our optical table is shown in Figure 2.5. The laser beam from a Ti:Sapphire laser (see Sect. 2.2.1) is directed through two beam splitters that branch off parts of the beam for dumping and for beam analysis. The remaining beam is 'purified' by two lenses and a pinhole and then splits up into two paths, the pump and the probe beam. In the pump path, a variable delay is introduced by a mechanical delay line. Using mechanical choppers, both beams can be switched on and off at frequencies f_1 and f_2 . The pump (probe) beam is circularly (linearly) polarized, and both beams are focused onto the same spot on the sample. After the sample, the pump pulse is blocked and the probe pulse is either reflected (r) or transmitted (t) into the detection, where the angle of the linear polarization plane is determined.

2.2.1 Laser system

We use a commercial pulsed Ti:Sapphire laser system (Coherent Mira). It consists of a diode laser array that pumps a solid state laser (Nd:YVO₄), whose output at $\lambda = 532$ nm and a power of 10 W in turn pumps the Ti:Sapphire laser. This laser's wavelength is tunable between 700 and 1000 nm and it can be pulsed in the pico- or femtosecond regime with a repetition rate of 80 MHz. Shorter pulses mean a wider spread in the wavelength domain. As the Faraday rotation signal changes sign when changing the excitation energy (Fig. 2.3c), a large spread in laser wavelength will reduce the signal. Therefore, we mainly use the laser in ps-mode, where the pulse width is less than 1 nm.

The output power of the laser is between 1 and 2 W, but since only powers of the order of 1 mW are needed on the sample, most of the power is dumped directly after the laser, also to minimize noise from scattered laser light. Further reductions in laser power are achieved using a polarizer-analyzer pair and metallic absorptive filters (ND filters, not shown in Fig. 2.5).

A diagnose system is available to monitor the pulse width in time using auto-correlation techniques and a spectrometer to adjust the laser wavelength.

Additionally, the laser's repetition rate can be locked with a variable phase delay to a reference signal at 80 MHz, which can originate from another laser or from an electronic function generator.

2.2.2 Delay line

The laser beam is split up into a pump and a probe beam. To introduce a time delay between the pump and the probe pulse, we use a linear stage (Schneeberger, later Aerotech) that can move a retroreflector over a distance of $d = 50$ cm. Since the light has to pass this path twice, the maximum delay introduced is $\Delta\tau_{\max} = 2d/c = 3.3$ ns. In our setup, instead of delaying the probe pulse, we reduce the path traveled by the pump pulse.

2.2.3 Obtaining the polarizations

The laser beam from the Mira is already linearly polarized, therefore a linear polarizer for the probe pulse is not necessary. It can, however, reduce deviations from perfect linear polarization.

The circular polarization is obtained either with a Soleil-Babinet compensator (a wavelength tunable $\lambda/4$ -plate) or a photoelastic modulator (PEM) that switches between right- and left circularly polarized light at a frequency of 50 kHz.

2.2.4 Detecting the rotated polarization

Balanced photodiode bridge

The linear polarization of the probe beam is expected to be rotated by an angle θ_F on the order of μrad to mrad .

A simple method of measuring the rotation angle of the polarization plane of linearly polarized light is to use a polarization analyzer oriented at an angle $90^\circ + \varphi$ to the non-rotated polarization plane, φ being small. With a photodiode, the amount of light that can pass the analyzer is measured. The power reaching the photodiode is given by (assuming $\theta_F \ll \varphi$)

$$P_{PD} = P_0 \sin^2(\varphi + \theta_F) \approx P_0(2\varphi\theta_F + \varphi^2). \quad (2.3)$$

With $P_0 = 10 \mu\text{W}$, $\varphi = 1^\circ$ and $\theta_F = 1 \mu\text{rad}$, we measure a background signal on the photodiode of $P_{PD}^\varphi = 3 \times 10^{-9} \text{ W}$ and a signal due to the rotation θ_F of $P_{PD}^{\theta_F} = 3 \times 10^{-13} \text{ W}$. Such a small power is hard to measure with a photodiode. In fact, the shot noise power of the background signal P_{PD}^φ already amounts to $P_{\text{NEP}} = \sqrt{2hcP_{PD}^\varphi/\lambda} \approx 4 \times 10^{-14} \text{ W}/\sqrt{\text{Hz}}$ at $\lambda = 870 \text{ nm}$. The maximal bandwidth would thus be on the order of 10 Hz.

A more sophisticated method is the use of a *balanced photodiode bridge*. Here, the initially vertical polarization of the probe beam is rotated by an angle of 45° using a $\lambda/2$ -plate and then passed through a Wollstone prism. This bi-refracting prism has two different refractive indices for vertically and horizontally polarized light, resulting in two separate beams. Each beam is focused onto a photodiode whose output currents are proportional to the power of the vertical and horizontal polarization component P_v and P_h . We find for their ratio

$$\begin{aligned} \frac{P_v}{P_h} &= \tan^2(\theta_F + 45^\circ) \\ &= \frac{\sin^2(\theta_F + 45^\circ)}{\cos^2(\theta_F + 45^\circ)} \\ &= \frac{2}{1 - \sin(2\theta_F)} - 1, \end{aligned} \quad (2.4)$$

and from this the angle

$$\theta_F = \frac{1}{2} \arcsin\left(\frac{P_v - P_h}{P_v + P_h}\right) \propto P_v - P_h. \quad (2.5)$$

For small angles, θ_F is thus directly proportional to the difference of the photodiode currents ΔI . Comparing with Eq. (2.3), the measured quantity $\Delta I \propto P_v - P_h$ is proportional to θ_F and no background signal is present. With the same assumptions as above, we have to detect $P_v - P_h = 10^{-11} \text{ W}$, a value almost two orders of

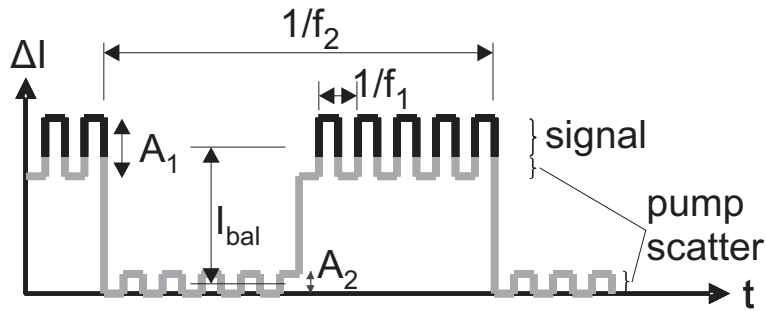


Figure 2.6: Photodiode difference current ΔI as a function of time. The pump beam is chopped at a frequency f_1 , the probe beam at a frequency f_2 .

magnitude larger than when using a polarization analyzer and within reach using the photodiodes described later in Sect. 2.3.1.

For most measurements, it is sufficient to know the angle in arbitrary units and therefore, $P_v + P_h$ need not be measured. A description of the photodiodes and the electronics is given later in Sect. 2.3.1.

Cascaded lock-in technique

Pump modulation

The balanced photodiode bridge is very sensitive to changes in the linear polarization plane, but it is not sensitive to where those changes originate from. To ensure that the rotation θ_F is only ascribed to effects induced by the pump pulse, the pump beam is chopped at a frequency $f_1 \approx 2$ kHz, and changes in ΔI are detected by a lock-in amplifier on that frequency. If using a PEM instead of a Soleil-Babinet circular polarizer, the beam is not chopped but the PEM's internal frequency of 50 kHz is used as a reference frequency.

Probe modulation

The scattering of pump pulses into the probe detection is a serious problem in pump-probe experiments. There are a variety of reasons, why pump light can end up on the detector photodiodes: scattering on lenses and mirrors, scattering on the sample or at the iris, where the pump beam is blocked. As long as the circular polarization of the pump pulse is maintained during these scattering events, the measurement is not disturbed, because the Wollstone prism will route half of the scattered power onto each photodiode and the contributions cancel in ΔI . As soon as the circular polarization is altered, however, pump scatter can make an experiment impossible, since pump powers usually are an order of magnitude higher than probe powers and already a small fraction of scattered light on one photodiode easily induces a current larger than the one induced by θ_F . While the pinhole in the detection line already

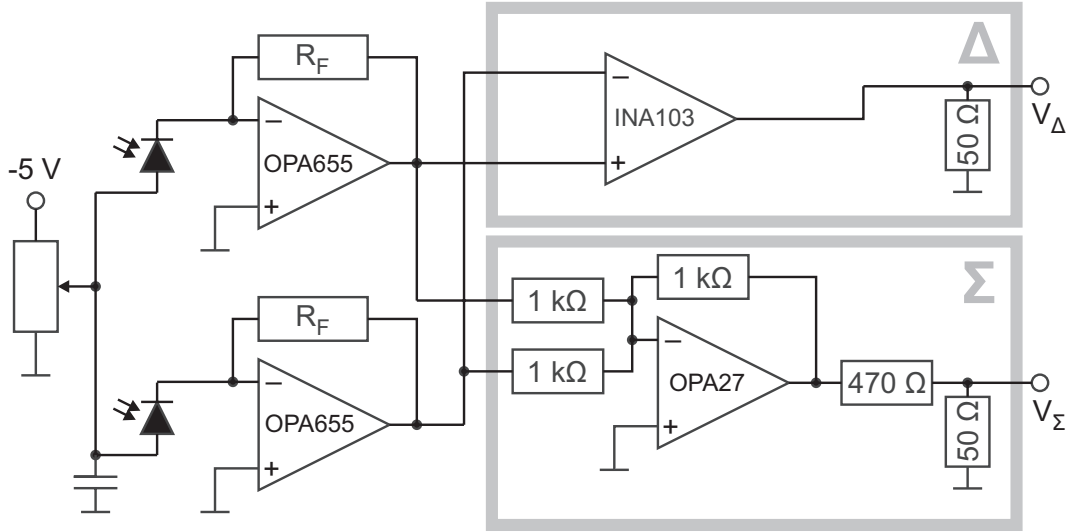


Figure 2.7: Schematics of the circuit converting the photodiode currents to voltages. The output voltage V_{Δ} is proportional to the difference of the photodiode currents ΔI , the output V_{Σ} is proportional to their sum. With a variable resistance, the photodiodes can be reverse biased to speed up their response. Feedback resistors R_F of 330 k Ω , 1 M Ω or 3.3 M Ω are used.

filters out a good amount of pump scatter, on most samples another method needs to be applied for measuring low-noise Faraday rotation.

By chopping the probe pulse at a frequency $f_2 \approx 300 \text{ Hz} \ll f_1$, it is possible to remove virtually all pump scatter from the signal ΔI . The principle is illustrated in Fig. 2.6. Note that for a perfectly balanced bridge (see Sect. 2.3.2), the averaged ΔI and with it I_{bal} will be zero. The difference photodiode current is first fed into a lock-in amplifier with reference frequency f_1 . Its output will periodically oscillate between A_1 and A_2 . When the probe beam is off, A_2 is measured due to pump scatter. When the probe beam is on, A_1 is the pump-induced signal on the sample superimposed on pump scatter. The desired signal thus is $A_1 - A_2$, which a second lock-in amplifier with reference frequency f_2 can readily detect.

The only requirement for this technique to work is the use of a lock-in amplifier that is capable of providing an analog output signal faster than f_2 . We use a Signal Recovery 7265 device, which updates its fast output at 166 kHz, thus fulfilling this requirement easily.

2.3 Electronics

2.3.1 Photodiode box

To measure θ_F with ample precision, care has to be taken also when converting the optical into an electric signal. We use photodiodes (Hamamatsu S7836-01) to transform the intensity of the laser beam into an electric current. Even though this current could be measured directly using the current input of a lock-in amplifier, we convert it into a voltage with an operational-amplifier-based I/V-converter. With this approach, we can produce a voltage signal V_Δ , proportional to the difference photodiode current ΔI and a signal V_Σ , proportional to the sum of the photodiode currents. Secondly, the signal can be amplified to voltages on the order of some ten millivolts, reducing the influence of noise that is picked up from electromagnetic interference on the way to the lock-in. A sketch of the electronics of our *photodiode box* is shown in Fig. 2.7.

The noise-sensitive high-impedance part of the circuit is restricted to both photodiodes and their connections to an opamp each, including its feedback resistor, all shielded inside a grounded metal case. The photo diodes have a noise-equivalent power $P_{\text{NEP}} = 3.9 \times 10^{-15} \text{ W}/\sqrt{\text{Hz}}$, which corresponds to the shot noise level at an optical power of $P_{\text{opt}} = P_{\text{NEP}}^2 \lambda / 2hc \approx 3 \times 10^{-11} \text{ W}$ ($\lambda = 870 \text{ nm}$). The photodiode converts this optical power to a current $I_{\text{opt}} = aP_{\text{opt}} \approx 20 \text{ pA}$ with a responsivity $a \approx 0.65 \text{ A/W}$. At the output of the opamp, I_{opt} translates to a voltage $V_{\text{opt}} = R_F I_{\text{opt}} \approx 14 \mu\text{V}$ (with $R_F = 1 \text{ M}\Omega$). The Johnson noise from R_F , $V_j = \sqrt{4k_B T R} \approx 0.12 \mu\text{V}/\sqrt{\text{Hz}}$, is small compared to V_{opt} . Neglecting the opamp input voltage noise, measurements above P_{opt} are shot-noise limited.

2.3.2 Auto-balancing the bridge

The $\lambda/2$ -plate should rotate the linear polarization plane of the probe beam to exactly 45° with respect to the optical axes of the Wollstone prism. This can be done manually by rotating the $\lambda/2$ -plate. However, when automatically scanning the laser spot over a sample area of several mm^2 , background effects of the sample substrate and/or the surface can induce a polarization rotation of the probe beam that is independent of the pump beam. Theoretically, the cascaded lock-in technique presented in Sect. 2.2.4 can cope with a non-balanced bridge ($I_{\text{bal}} > 0$ in Fig. 2.6), however, the first lock-in amplifier at frequency f_1 will have to be set to a high input voltage range, thereby losing sensitivity.

To be able to operate this lock-in amplifier in an optimal range, the bridge can be balanced automatically with the circuit shown in Fig. 2.8. This device incorporates a controller that aims at zeroing the averaged ΔI by rotating a motor-driven $\lambda/2$ -plate. It consists of three circuits:

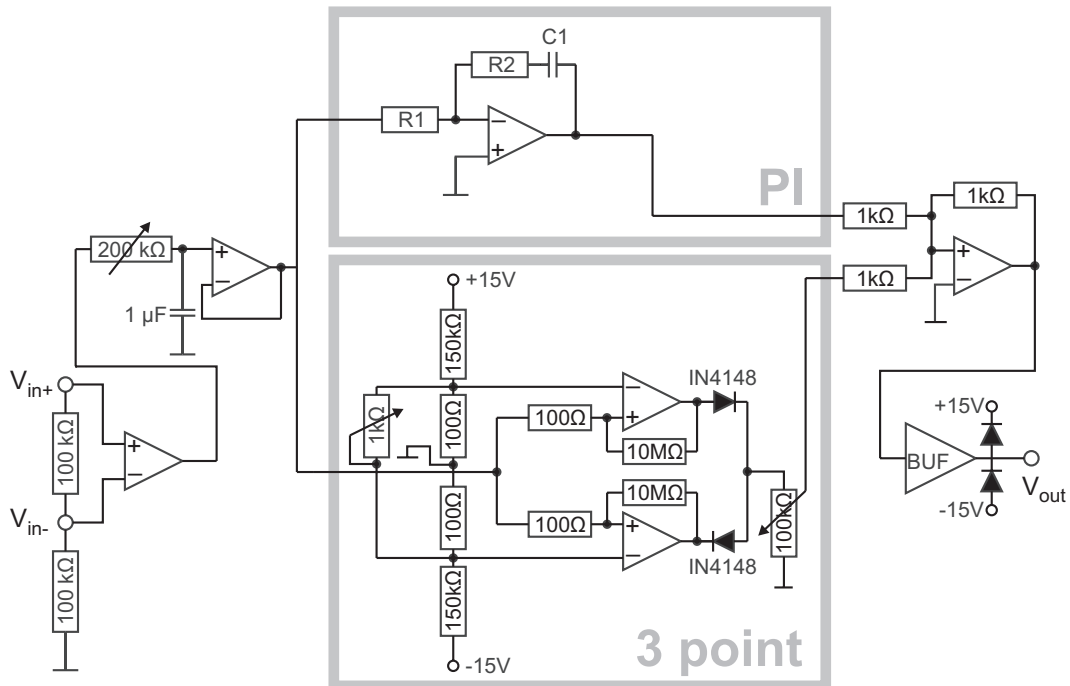


Figure 2.8: Schematics of the electronics that drive a d.c. motor which rotates the $\lambda/2$ -plate such that the time averaged signal V_{in} vanishes, using a PI controller. Since the d.c. motor requires a minimum voltage to start rotating, a 3-point controller compensating for this offset is implemented and its output is added to the PI controller.

low-pass filter The incoming voltage $V_{in} = V_{\Delta} \sim \Delta I$ is buffered and low-pass filtered (cutoff frequency 1 Hz)

PI controller A proportional plus integral controller monitors the deviation of V_{in} from zero and multiplies it by a value of ≈ 50 .

3-point controller To compensate for the offset of around 3 V that is needed to start the motor, a 3-point controller outputs ± 2.6 V as soon as the V_{in} exceeds a tolerance of $\approx \pm 8$ mV.

The outputs of the PI controller and the 3-point controller are added, buffered by an opamp capable of delivering a few 100 mA, and drive the motor, a Newport rotation stage SR50 CC.

2.4 Cryogenics

2.4.1 Cryostat

All experiments are performed below room temperature in an optical continuous flow cryostat ('Janis Research Supertran System'). Liquid helium ($T = 4.2$ K) flows from a dewar through an isolated transfer tube and then through the cryostat, where it cools the cold finger, a Cu block on which the sample is mounted in a chip socket. The cold part of the cryostat is in vacuum and protected by a metallic radiation shield. Four holes in this shield and four quartz windows give access to the sample from all four directions in the plane of the table. In addition, the cold finger can be rotated around the vertical y -axis. The cryostat itself can be moved in all three dimensions with three linear motors. Two motors can be used for scanning the laser beam over the sample surface in the x/y -plane, the third motor is used to adjust the sample surface into the focal plane of the focusing lens in z -direction. A heater and a temperature sensor are attached to the cold finger and connected to a PID-controller (LakeShore Model 331), allowing for measurements at temperatures between 4.2 and 325 K.

The samples are glued with silver epoxy into a ceramic chip carrier. Electrical contacts to the samples are bonded with Al or Au wires from the sample pad to the Au chip carrier pad. In the cryostat, two coax cables (LakeShore Type C) connect to two external BNC connectors, enabling measurements up to frequencies around 2 GHz. Additionally, 12 twisted-pair wires are available, whereof one suitable for applying up to at least 250 Volts.

Before cool-down, the cryostat is pumped to a vacuum on the order of 10^{-6} mbar. An electromagnet can be used to apply 'horizontal' magnetic fields along the x -axis up to 1.2 T.

2.4.2 Auto-centering the sample

Many experiments presented in the following chapters took several hours to several days of measurement time. Nevertheless, it was necessary that the laser focus spot remains at the same location on the sample during this time. In a cold-finger cryostat, the sample position changes with time as the cryostat cools down and the cold finger contracts. During cool-down, this leads to a sample movement (mainly) in y -direction of around 100-200 μm lasting for a few hours, even if the cryostat has reached base temperature already after around one hour. During the measurement, fluctuations in He flow or heater power change the sample position on the order of 10 μm .

Therefore, the laser spot is realigned periodically using the motorized x - and y -stages. Figure 2.9a shows the transmitted laser power through a sample used in

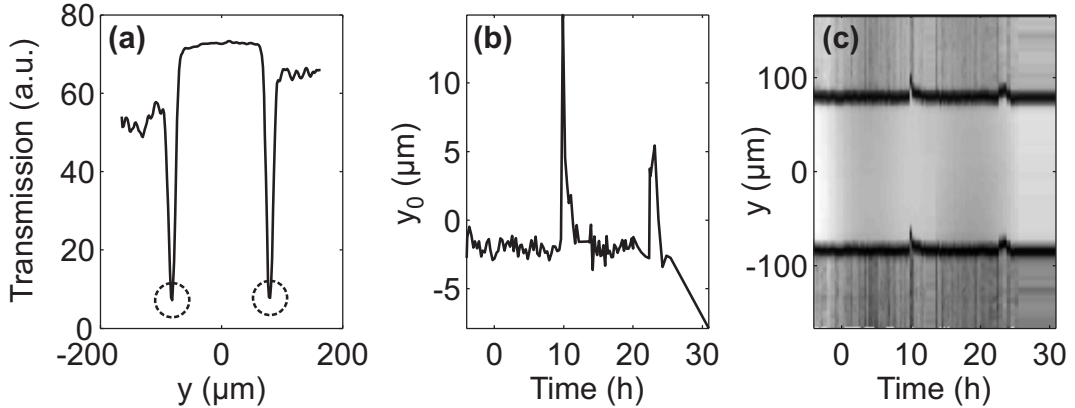


Figure 2.9: **(a)** Transmission through the sample as a function of y . Two horizontal gates (see Fig. 5.2 for an image of the sample used here) lead to two minima in the transmission, indicated by dashed circles. **(b)** Center position y_0 as a function of measurement time. The two peaks result from a change in He flow through the cryostat. **(c)** Transmission as a function of y and measurement time. During the measurements, the laser spot is always centered at $y = 0$.

chapter 5 as a function of y . The laser has to be centered between the two horizontal gates that each lead to a minimum in transmission. These minima are automatically determined and a new center position y_0 is calculated (Fig. 2.9b). This way, the laser spot stays centered over the whole measurement, as visible in Fig. 2.9c.

2.5 Quantum well samples

In the course of this work it became clear that carefully designed QW samples were crucial for the project. While the very first sample was grown by Danny Driscoll in the group of Art Gossard at the University of California in Santa Barbara, subsequent samples could be obtained from Emilio Gini's MOCVD and Silke Schön's MBE at the ETH cleanroom ('FIRST').

Requirements for the GaAs/InGaAs/GaAs QW samples were

- Spin coherence times on the order of a few nanoseconds to be able to determine the spin precession frequency with good accuracy.
- A sharp absorption edge that assures a high Faraday signal (Fig. 2.3).
- The possibility to contact the QW electrically to determine carrier density and mobility via Hall measurements, and to gate the QW.
- A 'high' g -factor to be able to measure many spin oscillations within the spin lifetime and a given magnetic field range.

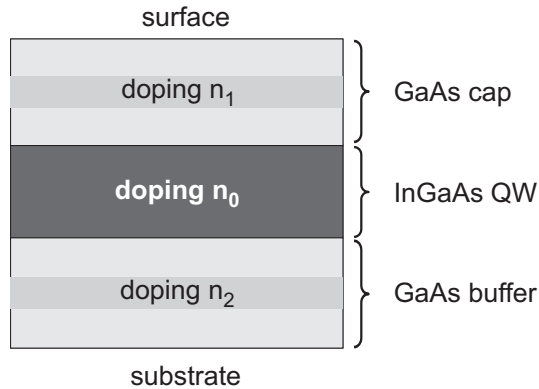


Figure 2.10: General structure of the GaAs/InGaAs QW samples.

- A laterally homogeneous g -factor over the wafer.

2.5.1 Basic wafer layer sequence

All wafers were grown in (001)-direction according to the scheme shown in Fig. 2.10: a GaAs buffer layer on the substrate with a n -doped layer incorporated, then a InGaAs QW layer n -doped over the whole width (In content between 7 and 10%) and finally a GaAs cap layer, again with a n -doping layer included.

Long spin coherence times in bulk GaAs have been found at doping densities around $3 \times 10^{16} \text{cm}^{-3}$ [43], therefore we aim the doping in the QW n_0 at this value. For a filled QW, the spin coherence time is not limited by the carrier recombination time (Sect. 1.2.1), therefore we introduce n -doping layers in the GaAs cap n_1 and in the GaAs buffer layer n_2 below the QW.

Band structure simulations for different doping densities $n_{0,1,2}$ are shown in Fig. 2.11. While the doping density in the QW n_0 has only limited influence on the band structure (Fig. 2.11a), variations in n_1 on the order of 10% can already lead to an empty QW, or, if the conduction band lies below E_F , to occupied states in the doping layer (Fig. 2.11b). When annealing Ohmic contacts, these states lead to parallel conductance and make the measurement of mobility and carrier density in the QW impossible. By adding a background doping n_2 below the QW, the range of acceptable cap dopings is increased and variations on the order of 20% become tolerable (Fig. 2.11c).

2.5.2 MOCVD-samples

On the MOCVD, the samples in the following table were grown. *Italic* print indicates that the values are design values which were not verified by another experimental technique.

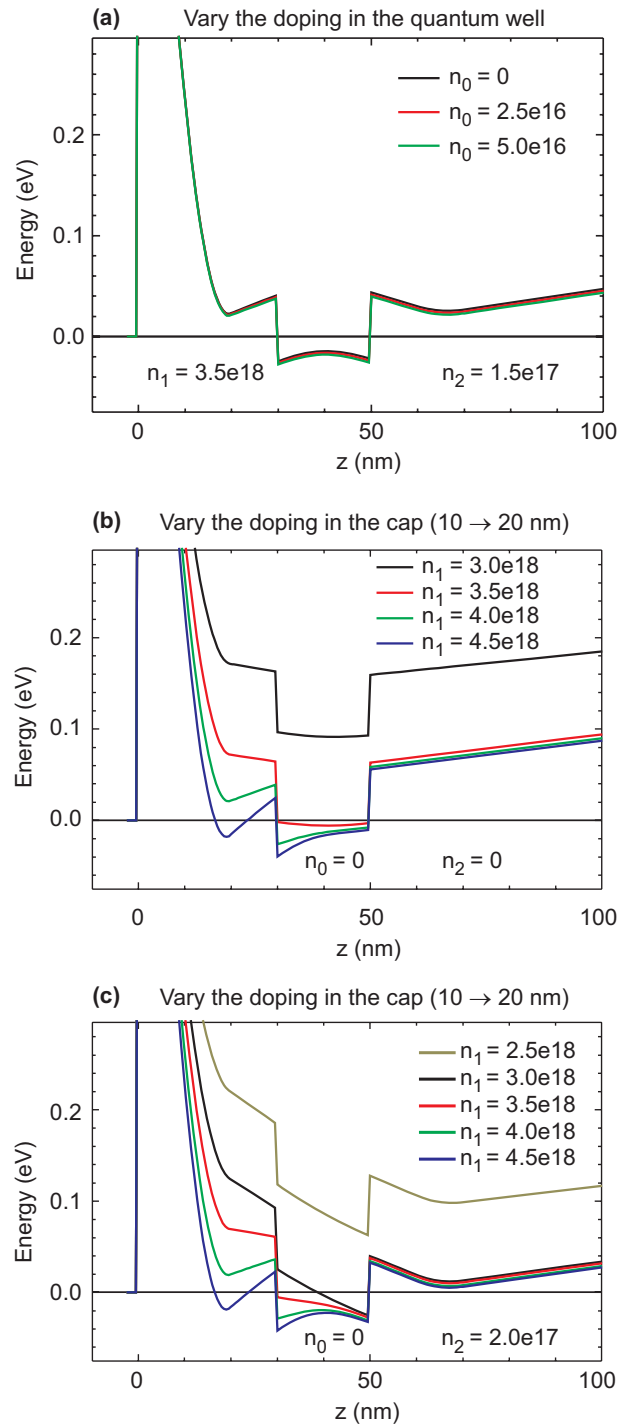


Figure 2.11: Band structure simulations with the Poisson-Schrödinger solver by Greg Snider. All doping densities are per cm³. We show only the conduction band with the Fermi energy E_F set to 0. **(a)** Changing the doping in the QW has only very little influence on the band structure. **(b)** Already small variations of the doping in the cap can lead to parallel conductivity in the doping layer or to a depleted QW. **(c)** A background doping below the QW can extend the cap doping range within which the QW is filled and no parallel conductivity occurs.

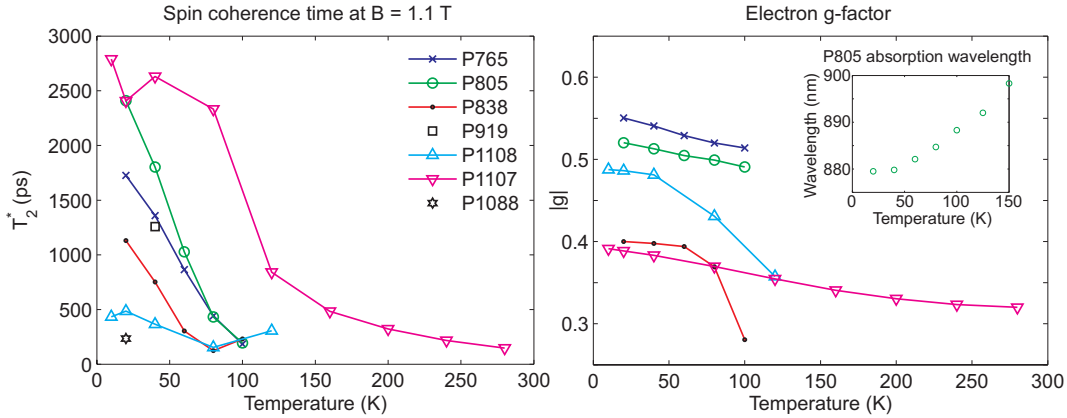


Figure 2.12: Optical characterization of the MOCVD samples. Spin coherence time (left), electron g -factor (right), and absorption edge wavelength (inset) as a function of temperature.

Wafer number	P765	P805	P838	P919	P1108
In content (%)	8.8	8.8	8.6	8.5	10
QW thickness (nm)	41	43	27	20	20
Cap thickness (nm)	21	19	20	20	30
QW doping n_0 (cm^{-3})	$1e16$	$5e16$	$2e17$	$5e16$	$5e16$
Cap doping n_1 (cm^{-3})	$5e18$	$5e18$	$5e18$	$5e18$	$3.5e18$
Background doping n_2 (cm^{-3})	0	0	0	0	$3e17$
Max. spin coherence time (ps)	1700	2500	1200	1500	500
Max. $ g $ -factor	0.55	0.53	0.40	0.52	0.48

To calibrate the doping densities, two n -doped GaAs epilayers were grown and characterized at $T = 4.2$ K:

A strongly doped layer (P1088, 277 nm thick) aimed at a doping density $5.0 \times 10^{18} \text{ cm}^{-3}$. Hall measurements yielded $n = 3.9 \times 10^{18} \text{ cm}^{-3}$ and a mobility $\mu = 1760 \text{ cm}^2/\text{Vs}$.

A weakly doped layer (P1107, 1980 nm thick) aimed at $5.0 \times 10^{16} \text{ cm}^{-3}$. Hall measurements showed $n = 5.1 \times 10^{16} \text{ cm}^{-3}$.

With this calibration, wafer P1108 was grown. However, optical measurements on this sample showed a short spin coherence time of less than 500 ps. An optical characterization of all MOCVD grown wafers is shown in Fig. 2.12. Spin coherence times of the QW samples decreased rapidly with increasing temperature, only the weakly doped epilayer (P1107) allowed measurement of the spin precession up to room temperature.

Note that the g -factor is expected to be negative, but since the sign cannot be determined by TRFR, we plot $|g|$. Assuming a negative g , the g -factor increases

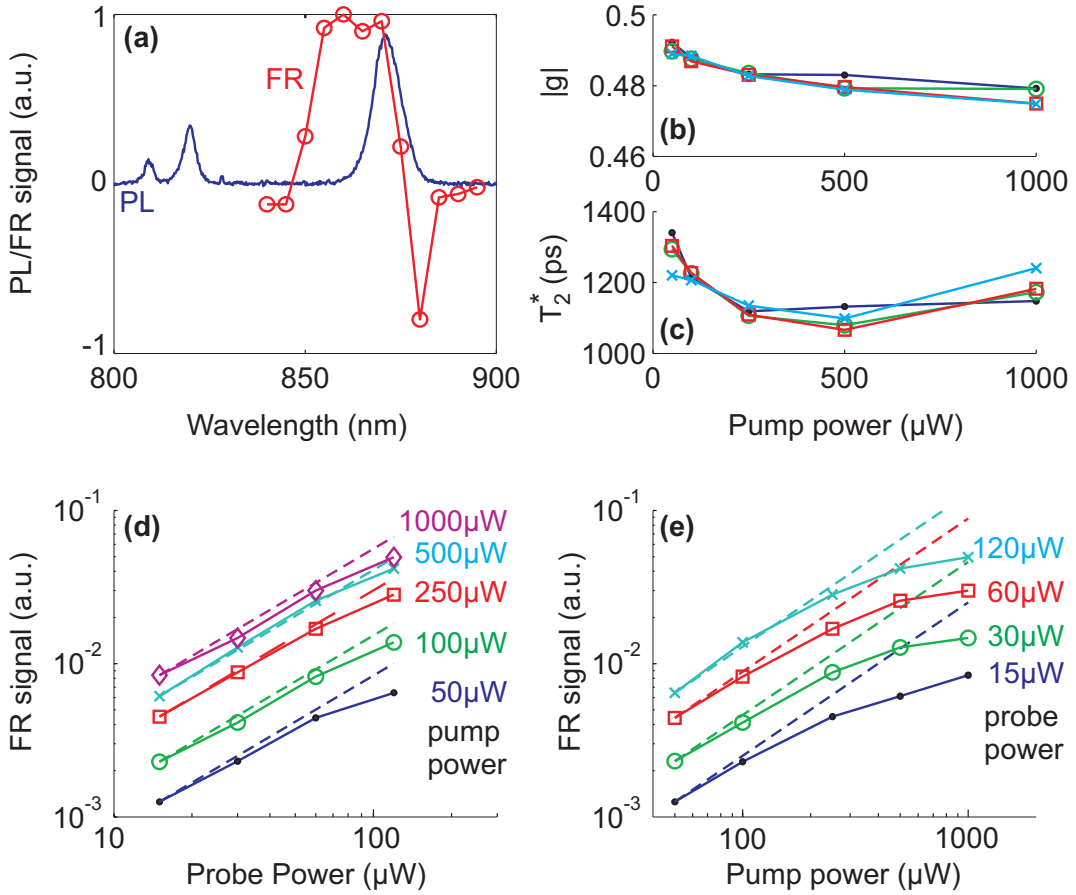


Figure 2.13: Optical characterization of wafer P919. (a) Photoluminescence (PL) and Faraday rotation (FR) as a function of wavelength. For the PL-measurements, the excitation was at 750 nm. Two GaAs-peaks are visible around 820 nm, the QW-peak is centered around 880 nm. (b) Dependence of the g -factor, and, (c) the spin coherence time T_2^* on the pump power in a TRFR-measurement. (d) FR signal as a function of probe power measured at different pump powers. (e) FR signal as a function of pump power measured at different probe powers. Dashed lines in both (d) and (e) indicate a linear relation between FR signal and pump/probe power.

towards the free electron value of $g \approx +2$ when increasing the temperature, consistent with findings in [57]. In Fig. 2.13a, the photoluminescence (PL) and Faraday rotation (FR) signal are plotted as a function of wavelength for wafer P919. As seen in Fig. 2.3, the FR signal is highest on the rising edge of the absorption edge (corresponding to the rising flank of the PL peak). In Fig. 2.13b and c, the g -factor and T_2^* -dependence on the pump power are given. Both quantities change slightly, which we attribute to the occupation of higher states in k -space with increasing power. Those states do not necessarily have the same g -factor and lifetime as the lower states [20].

The FR signal θ_F as a function of pump and probe power is shown in Fig. 2.13d and e. In a simple picture, it is expected to increase linearly with each the pump and the probe power, as indicated by the dashed lines. In the experiment, the increase is less pronounced especially for large pump powers. This can be explained by the optically excited electrons, which raise the absorption peak and move it out of the energy window accessible by the pump pulse. The number of electrons N per area A is given by

$$\frac{N}{A} = \int_{E_0}^E g(E) dE, \quad (2.6)$$

where $g(E) = m^*/\pi\hbar^2$ is the density of states, in two dimensions independent of the energy. E_0 is the energy at which the first of the N electrons is filled in, E the energy of the state that accommodates the N th electron. As long as the laser pulse (≈ 2 ps) is short compared to the recombination time τ_r of the excited electrons ($\tau_r \approx 300$ ps, see appendix A) and the laser repetition rate slow compared to τ_r , we can assume that a constant number of photons per laser pulse each excites one electron. Then, the number N is determined by the laser power P , the laser's repetition rate $f_{\text{rep}} = 80$ MHz, the laser wavelength $\lambda = 870$ nm and a dimensionless parameter p that describes the probability for a photon to be absorbed in the QW:

$$N = p \frac{P}{f_{\text{rep}}} \frac{\lambda}{hc}. \quad (2.7)$$

Solving Eq. (2.6) for $E - E_0$ we obtain together with Eq. (2.7)

$$E - E_0 = \frac{N}{A \frac{m}{\pi\hbar^2}} = p \frac{P}{f_{\text{rep}}} \frac{\hbar\lambda}{2Acm^*}. \quad (2.8)$$

With p between 10^{-2} and 10^{-3} [58], $P = 1$ mW and the size of the laser focus spot $A = (10 \mu\text{m})^2$ we find $E - E_0 = 2 \dots 20$ meV, which is larger than the laser spectral width of $\Delta E \approx 1$ meV. Thus at high pump powers, the excited electrons increase the position in energy of the QW's absorption edge by an amount larger than the laser's pulse width ΔE , resulting in a flattening of the FR signal as a function of pump power, as well observed in Fig. 2.13e

On every wafer, we tried to determine the mobility and carrier density in the QW, either by the Van-der-Pauw method (see Sect. 2.5.4) or by etching a Hall bar. Ohmic contacts were either In or a AuGe alloy. Unfortunately, none of the experiments yielded satisfying results. The Hall density amounted to values on the order of 10^{16} m^{-2} and varied only little when increasing n_1 by factors of 5 and 25. This suggests that the Hall effect is dominated by a parallel conductivity in the doping layer. The doping layer is characterized by strongly localized states and inhomogeneities that could account for the non-vanishing R_{xy} at $B = 0$ in Fig. 2.14a. Also, no Shubnikov–de-Haas (SdH) oscillations were observed in R_{xx} and a top gate could not substantially tune the electron density in the QW (see Fig. 2.14b).

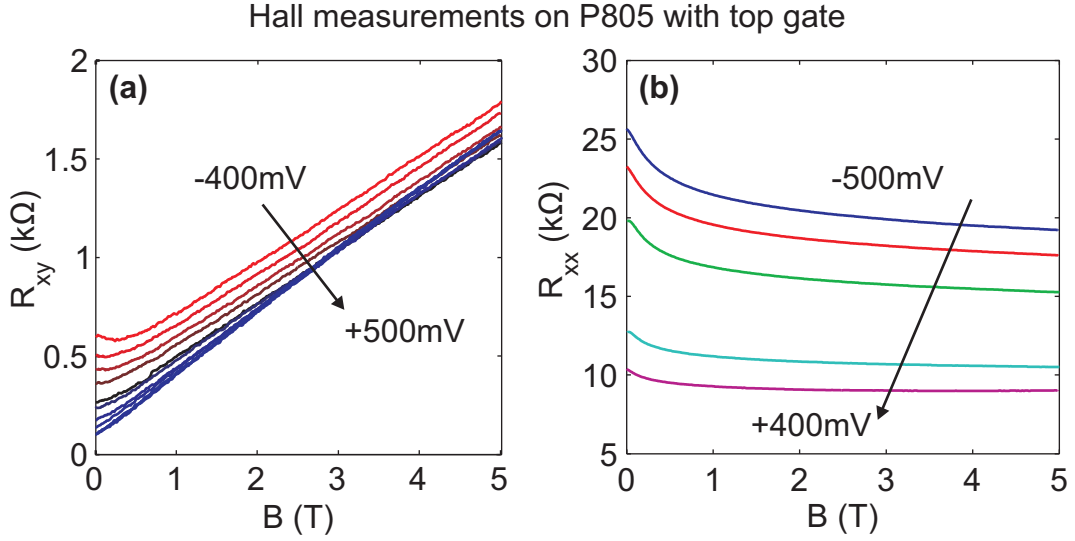


Figure 2.14: Electrical characterization of the MOCVD-sample P805. A Hall bar was etched and a metallic top gate (Au) evaporated on top of the Hall bar. Different curves represent different top gate voltages.

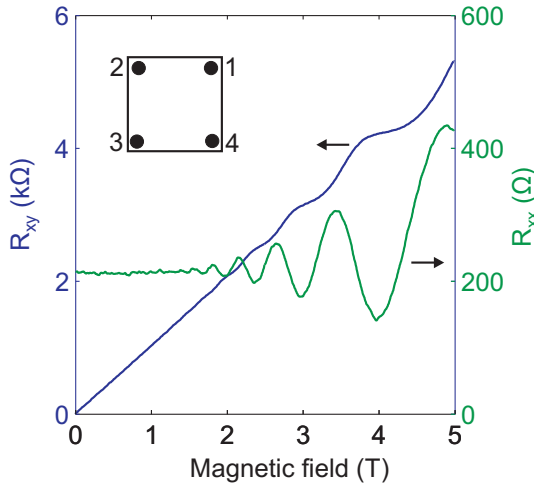


Figure 2.15: Van-der-Pauw measurements of sample ES887. From the slope in R_{xy} , a density of $6.0 \times 10^{15} \text{ m}^{-2}$ was extracted. The periodicity of the SdH-oscillations in R_{xx} yielded a density of $5.6 \times 10^{15} \text{ m}^{-2}$. Inset: numbering of the contacts.

2.5.3 MBE-samples

On the search for sample substrates that were suitable for both optical and transport measurements, Silke Schön was kind enough to provide us with QW samples grown on the MBE. While the first sample, ES823, could not be contacted with In or AuGe contacts, Hall measurements could be performed on all subsequent MBE samples. SdH-oscillations were observed in R_{xx} and densities on the order of $5 \times 10^{15} \text{ m}^{-2}$ as well as mobilities of around $\mu = 10\,000 \text{ cm}^2/\text{Vs}$ could be determined. The densities extracted from SdH and from classical Hall effect were in good agreement, indicating that no parallel conductivity influenced the QW transport properties (Fig. 2.15).

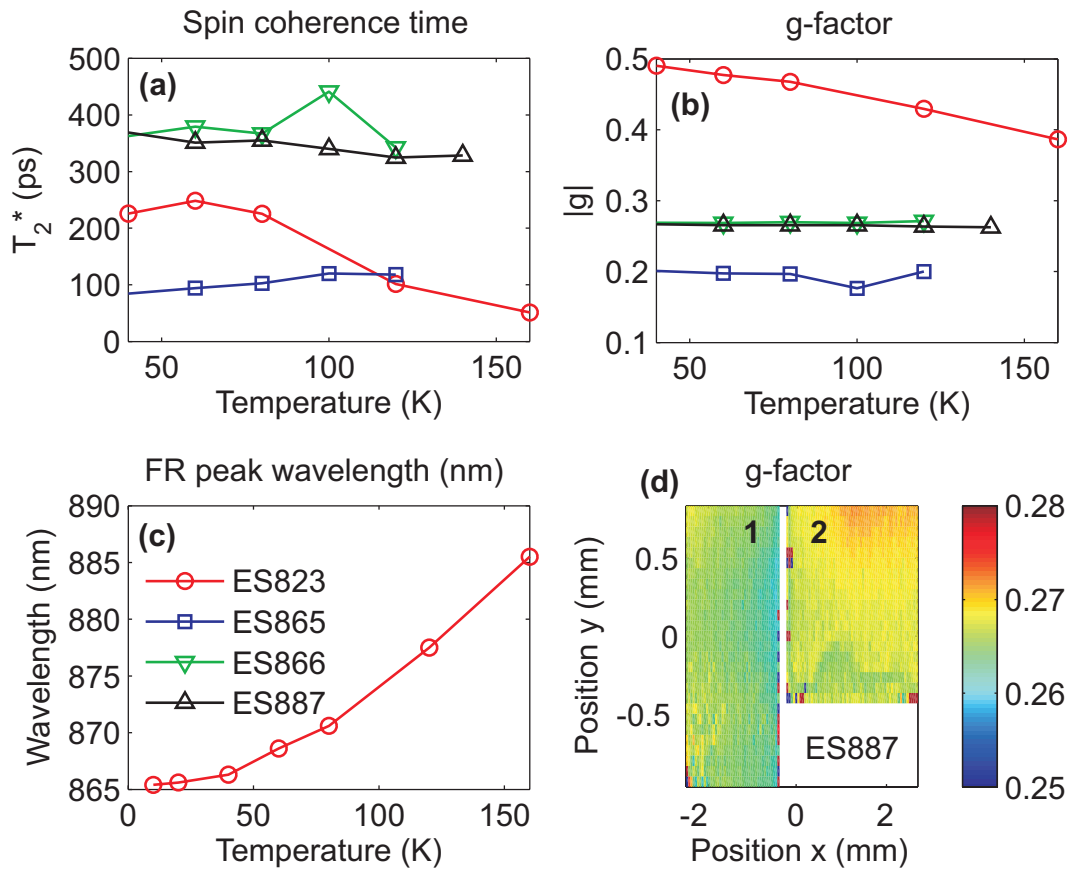


Figure 2.16: Optical characterization of the MBE samples. (a) Spin coherence time, (b) electron g -factor, and (c) FR peak wavelength as a function of temperature. In (d), a 2D-scan on two samples from wafer ES887 shows that the g -factor is homogeneous with deviations on the order of a few percent. Sample 2 is rotated by 90° with respect to sample 1.

The optical experiments, however, were less promising: As seen from Fig. 2.16, the spin coherence time was on the order of only a few 100 ps, and the g -factor, except for ES823, reduced to values between 0.2 and 0.3. Even though both spin coherence time and g -factor could be slightly enhanced when applying a negative voltage to a transparent top gate (Fig. 2.17), both values stayed below the corresponding values of the MOCVD-samples.

An overview of all MBE-samples is given in the following table:

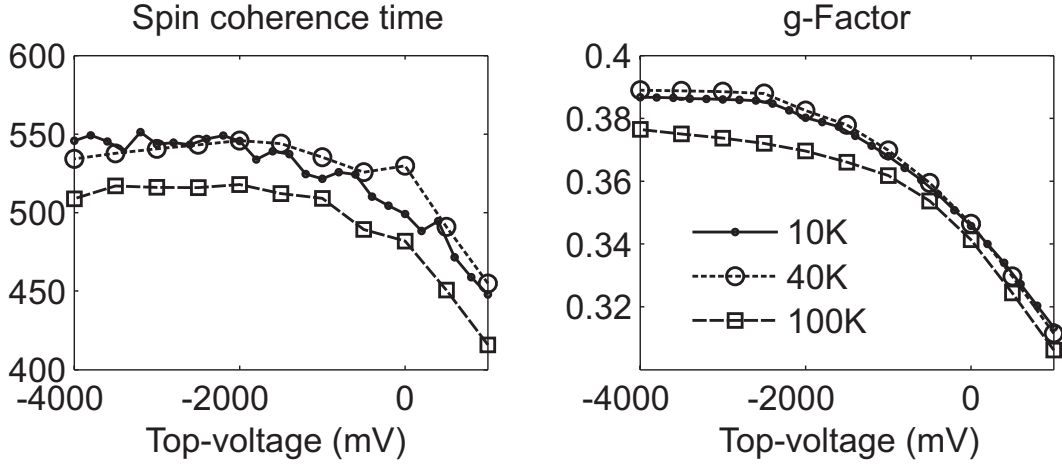


Figure 2.17: Spin coherence time and g -factor as a function of the voltage applied between QW and a transparent top gate (3 nm Ti + 7 nm Au) for three temperatures, wafer ES866.

Wafer number	ES823	ES865 ¹	ES866	ES887 ²
In content (%)	10	10	10	10
QW thickness (nm)	20	20	20	20
Cap thickness (nm)	30	30	30	30
QW doping n_0 (cm ⁻³)	3e16	3e16	3e16	3e16
Cap doping n_1 (cm ⁻³)	3.5e18	4e18	4e18	4e18
Background doping n_2 (cm ⁻³)	1.5e17	1.5e17	1.5e17	1.5e17
Max. spin coherence time (ps)	250	150	400	400
Max. $ g $ -factor	0.5	0.2	0.28	0.28
Density from Hall (m ⁻²)		4.2e15	5.0e15	6.0e15
Density from SdH (m ⁻²)		4.0e15	5.3e15	5.6e15
Mobility (cm ² /Vs)		10'100	9'700	10'600

¹ For ES865, the lower 25 nm of the 30 nm cap were AlGaAs with 10% Al content in order to prevent parallel conductivity.

² ES887 was a replica of ES866, which was contaminated with dirt during growth.

2.5.4 Van der Pauw technique

A convenient technique to determine the carrier density and mobility without the need for etching Hall bar structures was described 50 years ago by van der Pauw [59]. In principle, an arbitrarily shaped sample can be used, as long as no non-conducting islands are enclosed. We used rectangularly shaped samples (approximately 4 by 4 mm) with one small In Ohmic contact in each corner, circularly numbered from 1 to 4, see the inset of Fig. 2.15.

First, the carrier density is determined by the following two measurements: a current I_{12} is passed from contact 1 to 2 and the voltage V_{43} over the opposite edge is measured, giving $R_A = V_{43}/I_{12}$. A similar measurement yields $R_B = V_{14}/I_{23}$. The van der Pauw equation

$$e^{-\pi R_A/R_S} + e^{-\pi R_B/R_S} = 1 \quad (2.9)$$

can be numerically solved for the 2D sheet resistance R_S .

Secondly, a Hall measurement is performed by applying a diagonal current I_{13} and measuring V_{24} in a perpendicular magnetic field B . Now, the 2D density n and the mobility μ can be calculated from

$$n = \frac{I_{13}}{eV_{24}}B, \text{ and}$$

$$\mu = \frac{1}{enR_S}.$$

2.6 Sample processing

In the following short overview, the main clean-room processing steps are described. Almost all samples feature evaporated top gate structures that were fabricated using electron beam lithography.

2.6.1 Electron beam lithography

Sample cleaning

Samples were cleaned in an ultrasonic bath (42 kHz) with 7/9 power, during 3 minutes in first acetone, then isopropanol (also called isopropyl alcohol, IPA) and finally water. At the end, samples were dried by blowing N_2 onto them.

Resist deposition

After drying the samples at 180°C for about one minute, two layers of e-beam resist were spinned on:

A first ‘soft’ layer of P(MMA/MAA) in ethyl lactate 2:1.

A second ‘hard’ layer of PMMA 950K in chlorobenzene 1:1.

Both layers were spinned on at a speed of 6000 rpm during 60 seconds and then baked on the hotplate during 2 minutes at a temperature of 180°C .

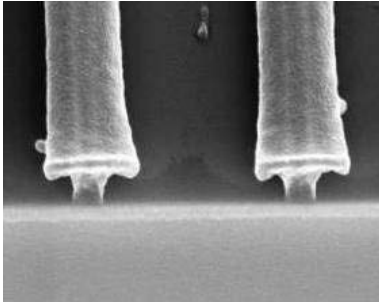


Figure 2.18: Scanning electron micrograph of the two-layer resist used with e-beam lithography. The horizontal bar of the ‘T’ is 500 nm wide. Sample is tilted by 30° and has been sputtered with 5 nm Pt for better contrast.

The first, soft layer is exposed and modified by the electron beam more easily than the second, hard layer. Therefore, an ‘undercut’ is created, well visible in Fig. 2.18. The first layer has a thickness of about 200 nm, the second layer of about 100 nm. When evaporating metals with a thickness smaller than that of the first layer, the lift-off process is eased, since the acetone that dissolves the resist can more easily creep below the metallization layer.

Samples are exposed on a Raith 150 electron-beam-lithography system. Especially for the small gratings with 1 μm period presented in chapter 3 (see Fig. 3.4 for an SEM-image of a grating), extensive dose test runs were necessary. For such large structures (100 \times 100 μm), proximity effects have to be accounted for, i.e. the dose inside the grating far away from an edge has to be reduced. Doses around 100 $\mu\text{C}/\text{cm}^2$ were used and already variations on the order of 5 % could either short a grating or interrupt an originally conducting metal bar.

After exposure, the samples were developed in IPA:MiBK 3:1 during 60 seconds and rinsed in IPA.

2.6.2 Gate evaporation

For non-magnetic gates, 80 nm of Au was evaporated on a 10 nm Ti adhesion layer. For magnetic gates, Fe was used instead of Au and in addition, a 10 nm Al layer was added on top in order to prevent oxidation of the Fe. The lift-off process especially for Fe gratings was often rather delicate, since only very weak ultrasonic power (1-2/9, 42 kHz) could be used. If too much ultrasonic power was applied, the Fe bars started to fall off. As a solution to this, the following steps were taken

- Increased adhesion layer thickness. The initially only 2 nm thick Ti layer was changed to 10 nm.
- Short oxygen plasma ash before evaporation (\sim 30 seconds / 200 W).
- Inspection of the sample while in acetone with the microscope. This way, the sample was only taken out of the acetone bath if the lift-off was successful. Otherwise, the ultrasonic power was increased.

The magnetic quality of the evaporated Fe was verified by measuring its magnetization in an external magnetic field, see appendix D.

2.6.3 Etching

To increase the magnetic stray field and to reduce effects of optical diffraction described in chapter 3, we put the Fe grating originally evaporated on top of the sample inside the QW by etching away stripes of GaAs/InGaAs. The task was thus to find a process capable of etching a PMMA-defined pattern into GaAs and subsequently evaporate Fe into the etched structure. While a wet etch with $\text{H}_2\text{O} + \text{H}_2\text{SO}_4 + \text{H}_2\text{O}_2$ (100:3:1) did not harm the PMMA-mask, it was unsuitable for our purpose due to the homogeneous nature of a wet etching process (Fig. 2.19a). Reactive ion etching (RIE) is a direction-sensitive technique. However, in the *Oxford RIE76*, the temperature of the sample could not be controlled satisfactorily and the PMMA-mask degraded (Fig. 2.19b). Adapting the RIE-process on the *Oxford ICP180* yielded already a much better result (Fig. 2.19c). The addition of Ar and Cl_2 to the originally CH_4/H_2 -based process further improved the result (Fig. 2.19d). To etch to a depth of 100 nm, the following process was found to work best (sccm = standard cubic centimeters per minute):

CH_4	H_2	Ar	Cl_2	Temperature	RF Power	Time
7 sccm	50 sccm	5 sccm	3 sccm	95° C	135 W	25 s

This process step was repeated twice, with 5 minutes N_2 flushing in between.

A more detailed description of the process can be found in [60].

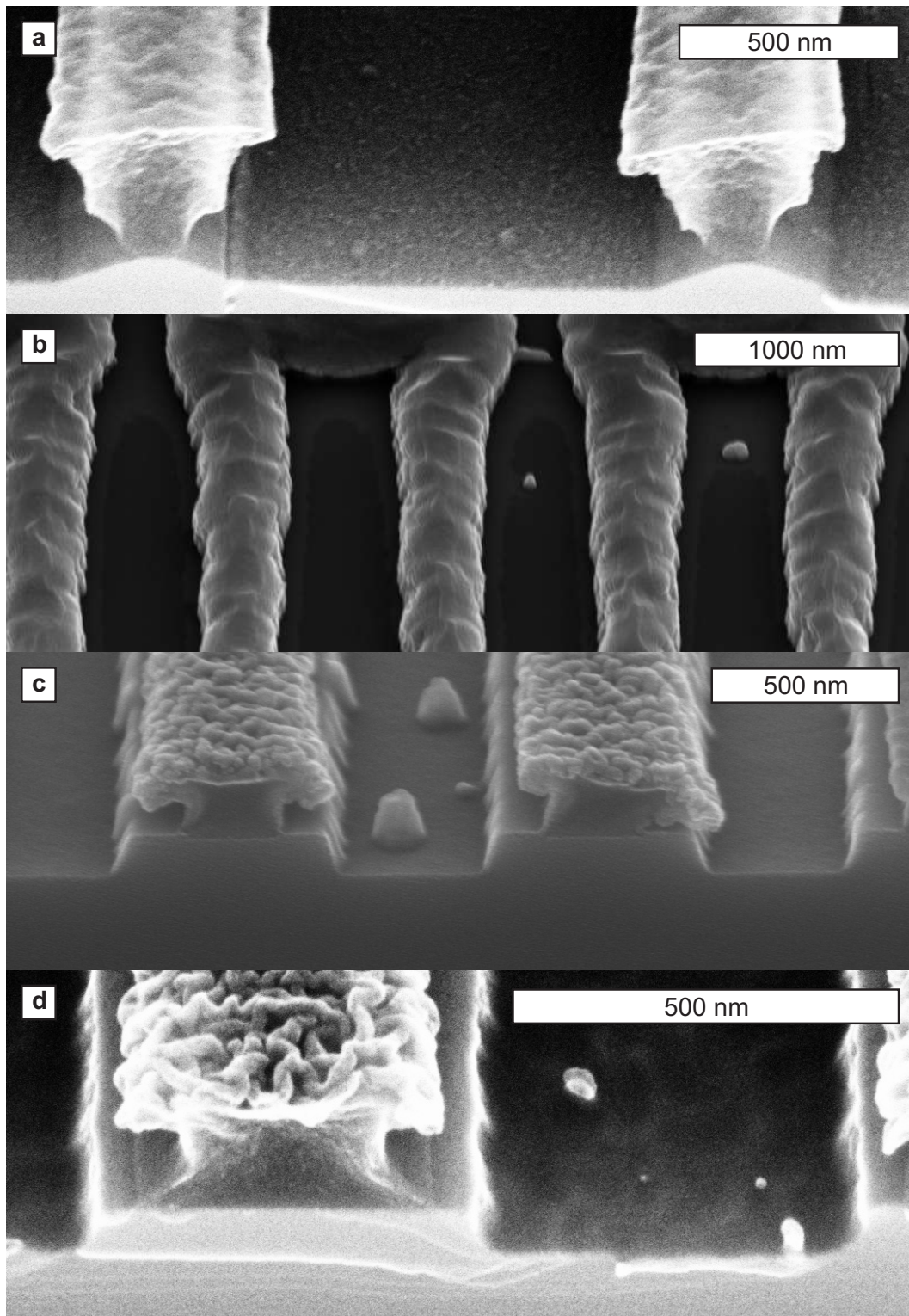


Figure 2.19: Scanning electron micrograph of etched bars by (a) wet etching with sulfuric acid and hydrogen peroxide, (b) RIE, (c) ICP, and (d) ICP with an optimized process. In a, c, and d, the 'T'-shaped PMMA and the underlying, etched GaAs is well visible. In b, the sample was not cleaved and only the (damaged) PMMA mask is visible. Samples are tilted by 30°.

Chapter 3

Spin manipulation with magnetic fields

This chapter reports on the stray-field-induced manipulation of electron spins. In Sect. 3.1, the use of magnetic stray fields for spin manipulation is motivated, followed by a brief review of previous achievements in the field (Sect. 3.2). In Sect. 3.3, the magnitude and geometrical dependence of magnetic stray fields are discussed. Section 3.4 describes the measurement of electron spins precessing in the magnetic stray field of ferromagnetic gratings, evaporated on top of the QW samples. These measurements are extended to etched gratings in Sect. 3.5.¹

3.1 Introduction and motivation

Since the electron spin couples directly to the magnetic field, spin manipulation with magnetic fields is the most straight-forward approach. Classically, the interaction of a spin \mathbf{S} (or in general a magnetic moment) with a magnetic field \mathbf{B} is governed by the Bloch equations,

$$\frac{d}{dt}\mathbf{S} = \frac{g\mu_B}{\hbar}\mathbf{S} \times \mathbf{B}. \quad (3.1)$$

Note that spin relaxation has been neglected for the moment. If a static magnetic field is applied in the direction of the spin polarization and an oscillating field in the plane perpendicular to this direction, electron spin resonance (ESR) is observed, if the frequency of the oscillating field matches the Larmor precession frequency of the static field. In this case, the spin can be flipped from a parallel alignment with the static field to an antiparallel orientation. More details on the calculation of the spin motion in this configuration with Bloch equations are given in Sect. 5.4.2.

¹Parts of this chapter have been published in L. Meier *et al.*, Appl. Phys. Lett. **88**, 172501 (2006)

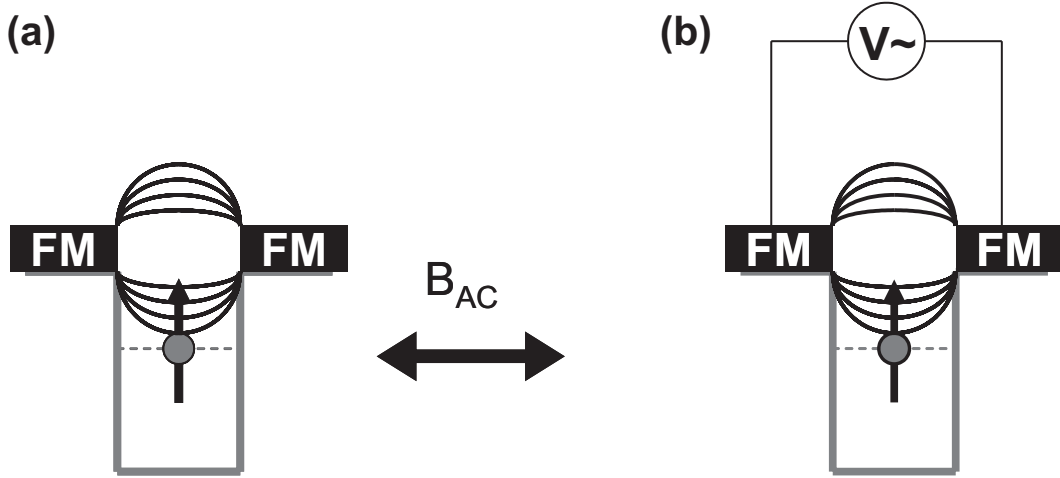


Figure 3.1: (a) An electron spin in a local magnetic stray field can be brought into resonance with a globally oscillating magnetic field. (b) By applying an a.c. voltage to the ferromagnetic gates, the confined electron oscillates in space and feels an oscillating magnetic field.

Here, we just want to point out the problem associated with this method when dealing with spin qubits: when the static field as well as the oscillating field are global, they act equally on all qubits. In a practical application, however, one would like to selectively prepare spin states in one particular qubit, for example a single electron spin in a quantum dot [16]. One possibility of being able to address a single spin would be the use of a slanting static field, so that the resonance condition with the oscillating field is only met at one particular location.

Another approach is the use of magnetic stray fields. Any magnetized piece of material exhibits a stray field that originates from the finite divergence of the magnetization at its boundary (see, e.g., [50] and [61]). For a given magnetization $\mathbf{M}(\mathbf{x})$, the scalar magnetostatic potential

$$\Phi_M(\mathbf{x}) = -\frac{1}{4\pi} \nabla \cdot \int \frac{\mathbf{M}(\mathbf{x}')}{|\mathbf{x} - \mathbf{x}'|} d^3x' \quad (3.2)$$

is calculated. From $\Phi_M(\mathbf{x})$, the magnetic (stray) field is obtained analogously to the electric field from the electric potential

$$\mathbf{H}(\mathbf{x}) = -\nabla\Phi_M(\mathbf{x}). \quad (3.3)$$

The length scale on which we expect a non-vanishing stray field is thus determined by $\mathbf{M}(\mathbf{x})$. Indeed, as shown later in Fig. 3.3, the magnetic stray fields of a ‘small’ and a ‘large’ piece of Fe look similar and decay on the length scale of the magnetized sample.

By bringing ferromagnetic gates close to a quantum dot, their stray field provides a static magnetic field. By changing the dimensions of the gates, the magnitude of

this static magnetic field is modified and could be individually tuned for each dot, enabling an external oscillating field to address a single spin, as schematically shown in Fig. 3.1a. A more elaborate scheme is shown in Fig. 3.1b, where no external magnetic field is needed. An a.c. gate voltage applied to the ferromagnetic gates brings the electron in the quantum dot into an oscillatory movement. Since the stray field is inhomogeneous, the spin feels an oscillating magnetic field. Combining this with a static stray field from other ferromagnetic gates could in principle allow for ESR solely with magnetic stray fields.

In this chapter, the interaction of magnetic stray fields from ferromagnetic gates with electron spins is studied. Since the investigation of single electrons in quantum dots is rather sophisticated, the manipulation of quantum well electrons below ferromagnetic gates is studied. The gates are evaporated (see Sect. 2.6.2) on the QW samples described in Sect. 2.5.

3.2 Previous work on magnetic stray fields

3.2.1 Detection of magnetic stray fields

Different approaches have been taken to characterize and detect magnetic stray fields. Magnetic-force microscopes [62] or scanning Hall probes [63] provide spatially mapped field distributions. The influence of stray fields on nearby semiconductor spin-states has been investigated by photoluminescence [64, 65], spin-flip light scattering [66] and cathodoluminescence [67] in semiconductor QWs. Since the Zeeman splitting in a QW is typically much smaller than the photoluminescence linewidth, experiments have focused on diluted magnetic semiconductors that exhibit a very large electron g -factor and correspondingly a large Zeeman splitting. The spatially varying Zeeman-splitting induced by a magnetic stray field has also been considered for spin-selective confinement of electrons [68]. Attempts to directly monitor the influence of stray fields on the dynamics of electron-spins have so far remained elusive [69].

3.2.2 Electrical control of spin dynamics

To address individual spins in an array of localized spins, either an a.c. magnetic field has to be applied locally, or the array has to be exposed to a magnetic-field gradient, whereby individual spins are addressed by changing the frequency of a global a.c. field. The latter approach might be facilitated by locally tuning the electron g -factor with an electric field [48, 49]. Also, effective a.c. magnetic fields can be provided locally using electric gates, as has been demonstrated for systems with anisotropic g -factor tensors [70] and for systems with strain-induced spin-orbit coupling [71].

The use of magnetic stray fields to manipulate single electron spins in a quantum dot [72] via a spatial displacement in the large and inhomogeneous magnetic field has been suggested. Such a spatial displacement can be induced by applying an electric field to metallic gates, which is technically easier to achieve than providing an a.c. magnetic field at the high frequencies (GHz) involved. Experiments that spatially displace electron spins within an inhomogeneous stray field are presented in the following chapter 4.

3.3 Numerical field simulations

To estimate the magnetic stray field that emanates from a magnetized structure, we use the numerical simulation tool OOMMF v1.2.0.3 (‘Object Oriented Micro-Magnetic Framework’) [73]. This tool requires Tcl/Tk, which is freely available for Windows as ‘ActiveTcl’ [74]. It numerically solves the Landau-Lifshitz Equation [75]

$$\frac{\partial \mathbf{M}(\mathbf{r}, t)}{\partial t} = -\gamma \mathbf{M}(\mathbf{r}, t) \times \mathbf{H}_{\text{eff}}(\mathbf{r}, t) - \frac{\alpha \gamma}{M_s} [\mathbf{M}(\mathbf{r}, t) \times (\mathbf{M}(\mathbf{r}, t) \times \mathbf{H}_{\text{eff}}(\mathbf{r}, t))], \quad (3.4)$$

where \mathbf{M} is the magnetization, γ the gyromagnetic ratio, M_s the saturation magnetization and \mathbf{H}_{eff} an effective magnetic field including contributions from anisotropy, exchange and demagnetization fields. The parameter α describes how fast the magnetic moments dissipate energy and relax into an equilibrium state. For our calculations, $\alpha = 0.5$. OOMMF integrates Eq. (3.4) and tries to find an equilibrium where $\partial M / \partial t = 0$.

For the simulation of a magnetic stray field, two steps are necessary:

1. Calculate the magnetization of a Fe bar in an external magnetic field B_{ext} by finding an equilibrium magnetization $\mathbf{M}(\mathbf{r}, t)$ with Eq. (3.4).
2. Calculate the stray field induced by this magnetization with Eq. (3.2) and (3.3).

The simulations are all in 3D. Yet, our structures are often much larger in y -direction than in x and z and we are mostly interested in the stray field in the x/z -plane.

An analytical solution of the 3D stray field of a homogeneously magnetized bar has been presented in [61]. These predictions agree well with the results of our simulations, however, they cannot account for effects of non-homogeneous magnetization in a sample, neither can they simulate the magnetization build-up at low magnetic fields.

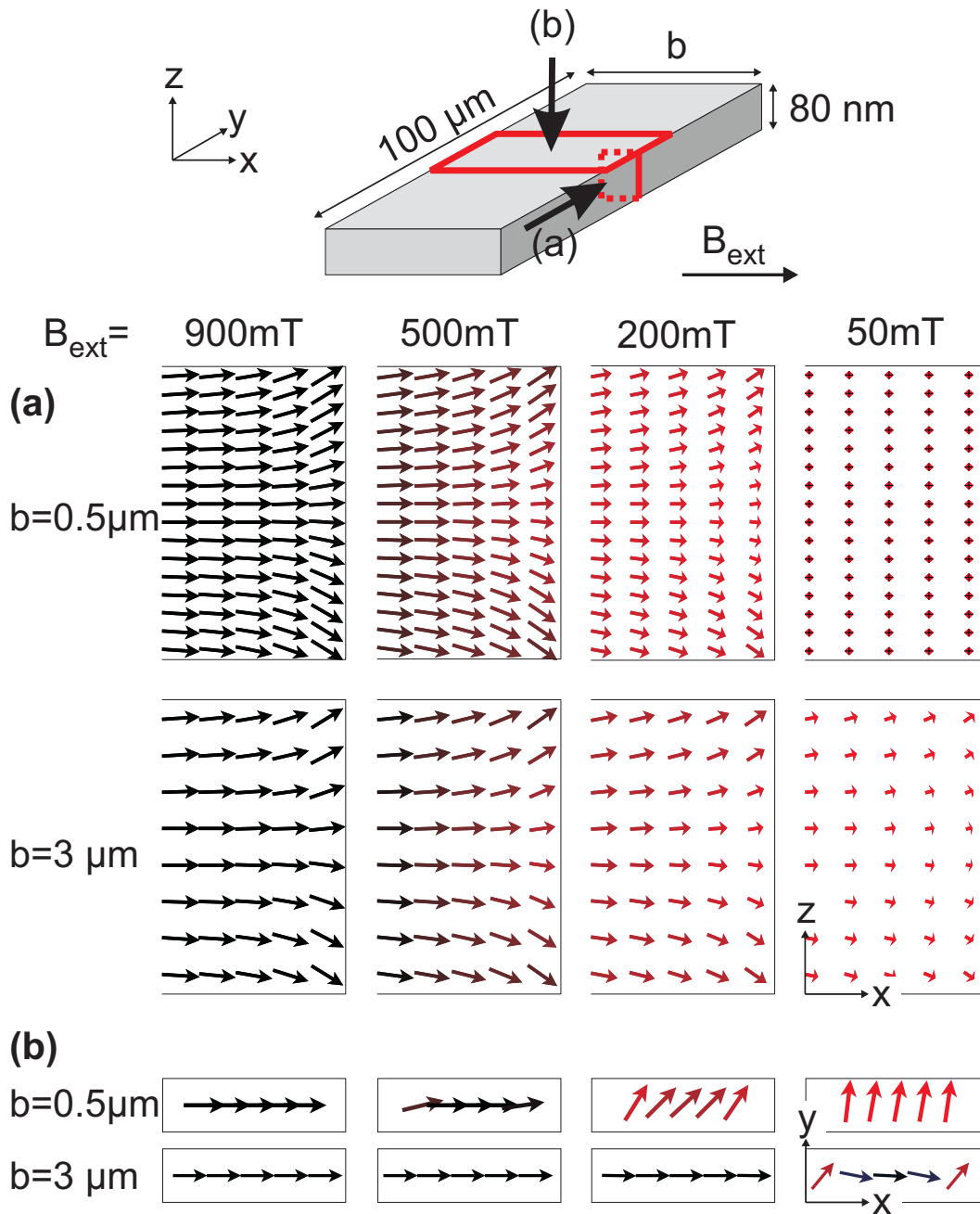


Figure 3.2: Numerical simulation of the magnetization of a Fe bar $80\ \text{nm}$ thick, $100\ \mu\text{m}$ long and $b = 0.5$ and $3\ \mu\text{m}$ wide, in an external magnetic field of 900 , 500 , 200 and $50\ \text{mT}$ along x . (a) shows the magnetization in the x/z -plane close to an edge of a cross-section through the middle of a bar, (b) illustrates the magnetization in the x/y -plane in the center of a bar. The red color indicates the y -component of the magnetization.

3.3.1 Magnetization simulations

Figure 3.2 shows a numerical simulation of the magnetization of two Fe bars, 80 nm thick, 100 μm long and $b = 0.5$ or 3 μm wide. The simulation started at an initial external magnetic field $B_{\text{ext}} = 1$ T in x -direction. To minimize numerical artefacts, B_{ext} was slightly rotated and had components of some milliteslas also in y - and z -direction. During the simulation, B_{ext} was reduced stepwise by 25 mT, and during each step the magnetization of the Fe bar was calculated. One cell was $10 \times 200 \times 5$ nm large for $b = 0.5 \mu\text{m}$ and $10 \times 200 \times 10$ nm for the wider bar with $b = 3 \mu\text{m}$. The simulation time amounted to approx. 12 hours on a 3 GHz Pentium 4 processor with 1 GB RAM.

At $B_{\text{ext}} = 900$ mT, both bars are magnetized along x . However, not all magnetic moments are aligned along x . While in the center of an x/z -cross-section of a bar, the magnetization is aligned along x , it slightly turns ‘outside’ close to an edge, visible in Fig. 3.2a. By this, the magnetization tries to reduce the energy of the stray field. Compared to simulations with (forced) full magnetization, this changes the stray field by 10% at most, depending on the position (see Figs. 3.6a and 3.18 later on). When reducing B_{ext} , the magnetization starts to rotate in direction of y , the component along y is indicated by shades of red. The narrower the bar, the higher is B_{ext} where this rotation occurs. At $B_{\text{ext}} = 50$ mT, the narrower bar is magnetized almost only along y , while for the wider bar, the magnetization is still partly aligned along x , as visible in Fig. 3.2b. At $B_{\text{ext}} = 0$, both bars are magnetized along y , which is therefore called the *easy axis* of the bar. In this configuration, the energy of the magnetic moments in their own demagnetization field $E \propto \mathbf{M} \cdot \mathbf{B} = NM^2/2$ is minimal. Here, N is the ‘demagnetizing factor’, which accounts for the geometry of the sample [76].

3.3.2 Stray field simulations

Three numerical stray field simulations are shown in Fig. 3.3. In Fig. 3.3a, a simulation of both the magnetization and the stray field of a 0.5 μm wide and 80 nm thick bar is shown. The microscopic example presented in Fig. 3.3b is a 1 μm wide and 80 nm thick Fe bar used in the experiments presented later on. Its magnetization has been determined with a simulation as described above. In Fig. 3.3c, the stray field of a macroscopic object is shown, an iron block that could serve as a kitchen magnet, $1 \times 2 \times 1$ cm large.

Close to a face perpendicular to the magnetization, where the divergence of the magnetization is highest, stray fields of $4\pi M_s = 2.1$ T are expected (see the next section for a measurement of the saturation magnetization M_s). The stray field decays rapidly on the length scale of the magnetized sample, one length (1 μm or 2 cm) away, the stray field is less than 20 mT.

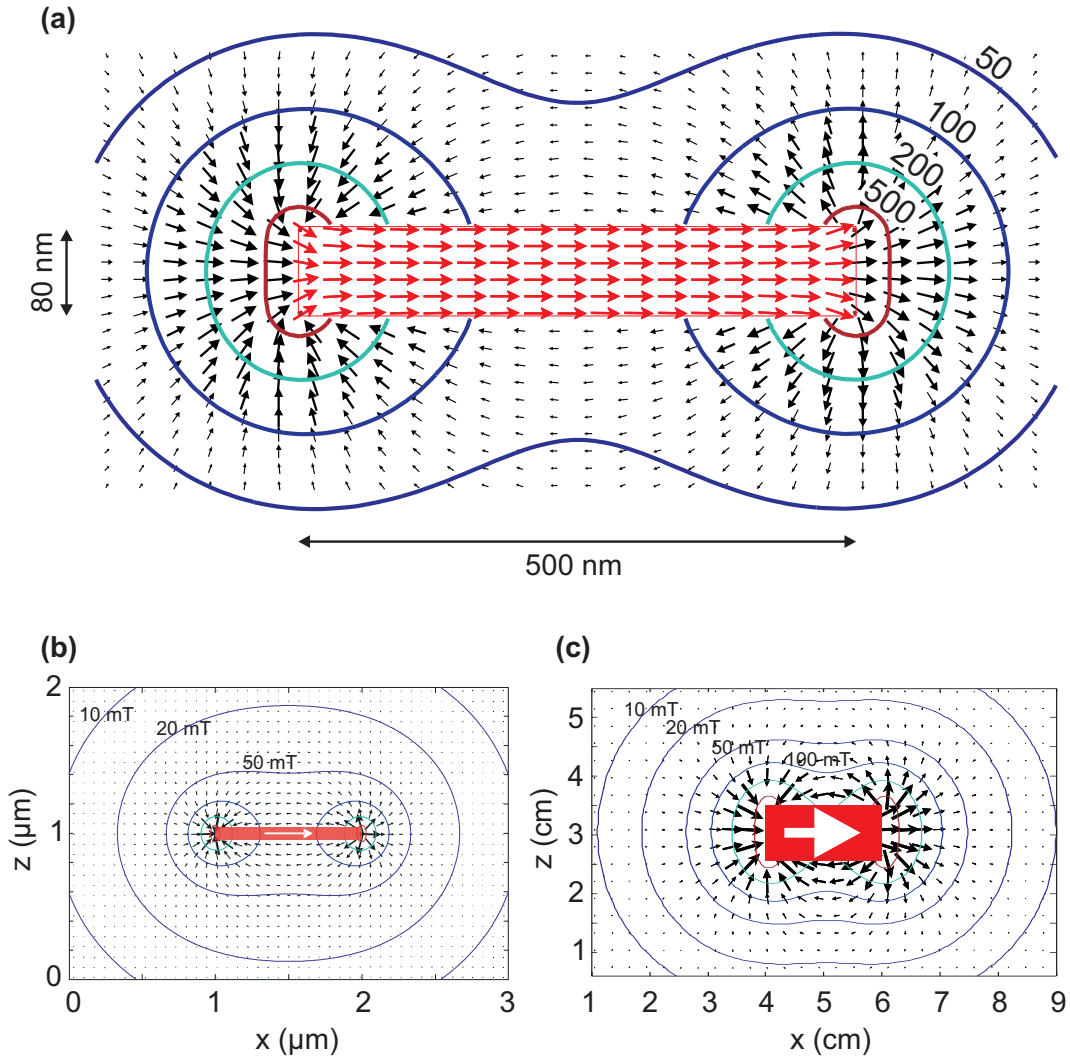


Figure 3.3: Magnetic stray field simulations. **(a)** Magnetization of a Fe bar (red arrows inside the bar) and the induced stray field outside the bar. Lines indicate constant fields and are labeled in millitesla. **(b,c)** Stray field of a magnetized microscopic **(b)** and a fully magnetized macroscopic **(c)** iron sample. Equi-field lines are at (counting from the inside) 500, 200, 100, 50, 20, and 10 mT.

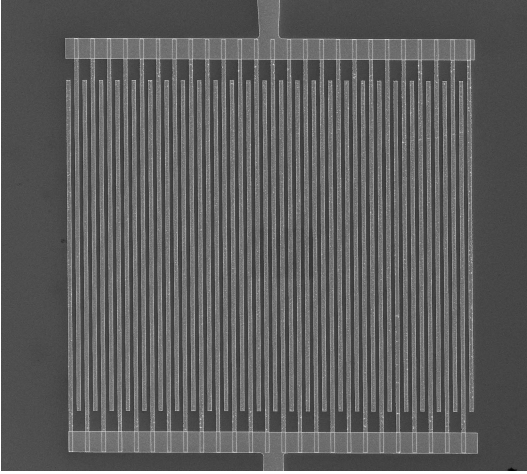


Figure 3.4: Scanning electron micrograph of a Fe grating. The grating is 100 by 100 μm large, each bar and each gap 1 μm wide.

3.4 Stray field measurements on ferromagnetic gratings

3.4.1 Measurement setup

On the surface of samples from wafer P805, Fe and Au gratings have been fabricated using electron beam lithography and lift-off techniques as described in Sect. 2.6.1 and Sect. 2.6.2. Figure 3.4 shows an SEM-image of such a grating with interdigitated gate electrodes, i.e. with separate electrical connections to odd and even bars. The gratings consist of 100 μm long bars with a thickness of 80 nm. As an adhesion layer between GaAs and the metal, we use 10 nm Ti. The Fe bars were capped with 10 nm Al to prevent oxidation. We vary the width of the bars as well as their spacing. The bar spacing (i.e. the gap) is always equal to the bar width. We have fabricated bars with widths 3 μm , 2 μm , 1 μm , and 0.5 μm and refer to the corresponding gratings as 3-3, 2-2, 1-1 and 0.5-0.5, meaning (bar width)-(gap width).

TRFR is measured in the Voigt geometry with an external magnetic field B_{ext} applied along x (in the QW plane and perpendicular to the long axis of the bars). Electron spins are polarized along z (perpendicular to the QW) by a circularly polarized pump pulse. The helicity of the circular polarization is modulated with a photo-elastic modulator at a frequency of 50 kHz, allowing the use of lock-in amplifiers. We measure the Faraday rotation angle $\theta_F(\Delta\tau)$ of a linearly polarized probe pulse that is delayed by a time $\Delta\tau$ with respect to the pump pulse, as described in detail in Sect. 2.1. The laser is tuned to the absorption edge of the QW at 870 nm and focused to a spot of about 15 μm in diameter. The pump (probe) beam has a power of 500 (60) μW . From the oscillating $\theta(\Delta\tau)$ we extract the spin coherence time T_2^* and

$$\nu = g\mu_B B_{\text{tot}}/h \quad (3.5)$$

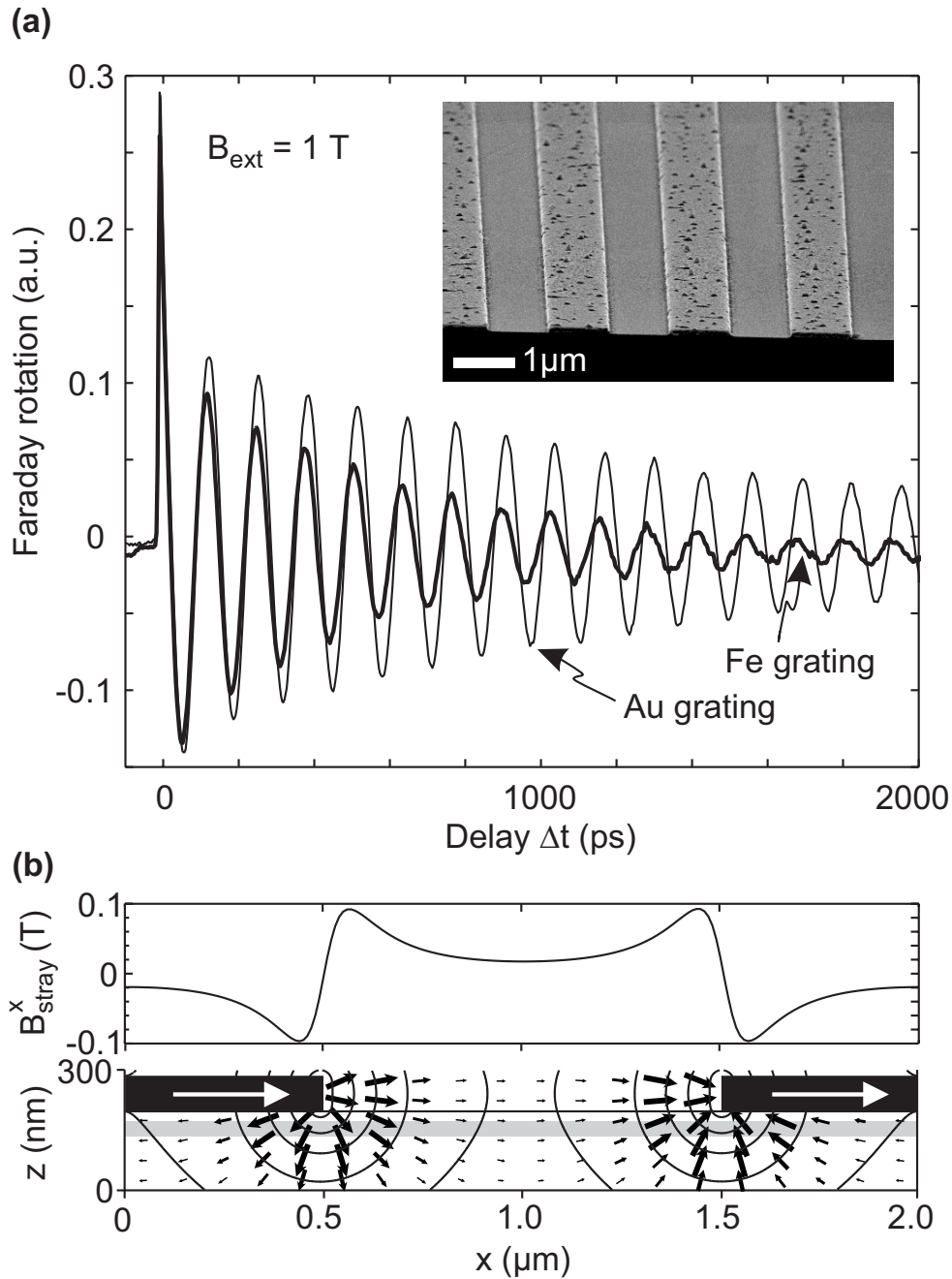


Figure 3.5: (a) Faraday rotation measured at $T = 40 \text{ K}$ on a Fe and a Au grating with the dimensions 1-1. Due to the magnetic stray field of the Fe grating, the electrons precess faster and their lifetime is reduced. Inset: SEM-picture of a 1-1 Au grating. (b) Calculated magnetic stray field of two magnetized Fe bars: x -component (top), direction and magnitude (bottom). Each bar is $1 \mu\text{m}$ wide and 80 nm thick. Lines indicate constant magnetic fields of 500 mT , 200 mT , 100 mT , 50 mT and 20 mT (moving away from a bar). The shaded area shows the location of the QW.

by fitting it to Eq. (2.1). The total local magnetic field

$$\mathbf{B}_{\text{tot}} = \mathbf{B}_{\text{ext}} + \mathbf{B}_s + \mathbf{B}_n \quad (3.6)$$

includes B_{ext} , the magnetic stray field of the ferromagnetic grating B_s , and an effective magnetic field B_n resulting from hyperfine interaction of the electron spins with polarized nuclear spins. Within a good approximation, all magnetic fields point along the x -axis.

3.4.2 Expectations from numerical simulations

Stray field of two bars

A numerical simulation of the magnetic stray field of two Fe bars at $B_{\text{ext}} = 1$ T obtained as described above (Sect. 3.3) is shown in Fig. 3.5b. Here, the stray field of two separate, spatially displaced bars is superimposed, interactions between the bars are not taken into account. This is reasonable, since the stray field decays rapidly in space.

Magnetization build-up

At $B_{\text{ext}} = 0$, both bars are magnetized along their long (easy) axis in direction of y , and no stray field is expected along x . As B_{ext} is increased, the bars are magnetized in x -direction. Magnetization saturates at B_{ext} of 100-400 mT, depending on the bar width (Fig. 3.2a). We find good agreement with the experimental data presented in Sect. 3.4.3.

Average stray field

A numerically simulated stray field, homogeneously averaged over the gap width, is shown in Fig. 3.6a as a function of B_{ext} . The left scale indicates the average value of the stray field, the right scale the corresponding change in ν , assuming $g = 0.5$. The horizontal lines in Fig. 3.6a show the average stray field expected if the grating is fully magnetized. It is slightly lower than for the calculations assuming an inhomogeneous magnetization discussed in Sect. 3.3.1. This is because, as seen from Fig. 3.2, the magnetization at the edges points outwards and increases the stray field in the QW *below* the grating. When studying the stray field *between* the bars of a grating, the non-homogeneous magnetization reduces the stray field compared to fully magnetized bars (see Fig. 3.18 below in Sect. 3.5 on etched gratings).

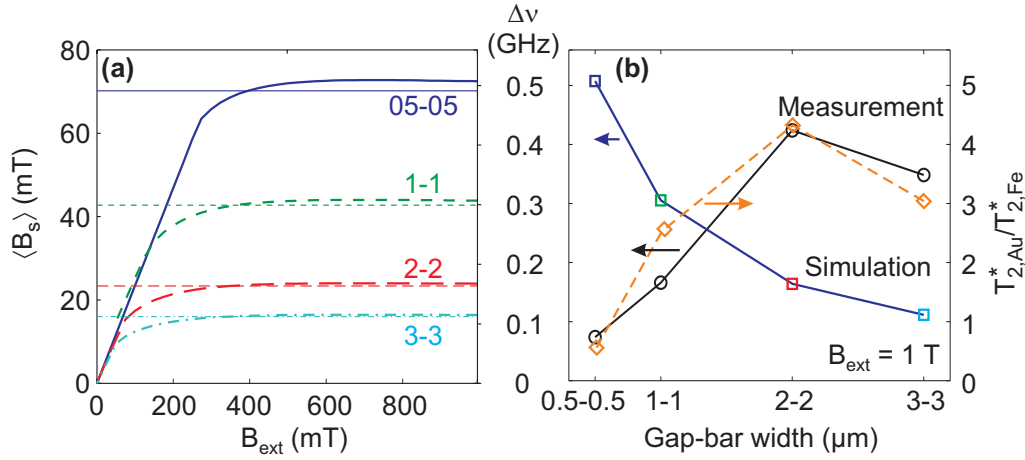


Figure 3.6: **(a)** Numerically calculated stray field as a function of B_{ext} . The stray field was homogeneously averaged over the gap width, the left scale indicates the averaged value, the right scale the corresponding change in precession frequency, $\Delta\nu = g\mu_B\langle B_s\rangle/h$, with $g=0.5$. Horizontal lines indicate $\langle B_s \rangle$ for homogeneously magnetized bars. **(b)** Stray-field-induced change in precession frequency $\Delta\nu$ at $B_{\text{ext}} = 1\text{ T}$ as expected from the simulations in (a), and as measured. Dashed line: Measured relative reduction in spin coherence time $T_{2,\text{Au}}^*/T_{2,\text{Fe}}^*$ at $B_{\text{ext}} = 1\text{ T}$.

Average electron precession frequency

To verify whether the averaged stray field can be directly converted into a change in precession frequency $\Delta\nu = g\mu_B\langle B_s\rangle/h$, we uniformly distributed electron spins in the QW between two Fe bars, all pointing along z at $\Delta\tau = 0$. For $\Delta\tau > 0$, the spins precess around a spatially varying $\mathbf{B}_{\text{tot}}(x, z) = \mathbf{B}_{\text{ext}} + \mathbf{B}_s(x, z)$. The averaged z -component of these spins was calculated as a function of $\Delta\tau$ and fitted with Eq. (2.1) to provide ν_{Fe} . The results obtained with this more sophisticated method correspond well to the findings obtained by simple averaging.

Expectations for different geometries

From these simulations, we expect $\Delta\nu$ to be between 0.05 and 0.5 GHz depending on the size of the gap between the bars. Larger gaps exhibit a lower $\Delta\nu$ than small gaps. For one individual Fe bar, \mathbf{B}_s does not depend on the bar width, as it relies on the divergence of the magnetization [Eq. (3.2) and (3.3)], which only depends on the boundaries of the bar. In the gap, \mathbf{B}_s decays quickly, and thus for larger gaps the averaged $\Delta\nu$ decreases. However, in the experiment, we find a non-monotonous dependence of $\Delta\nu$ on the gap size, see Fig. 3.6b and later Sect. 3.4.3.

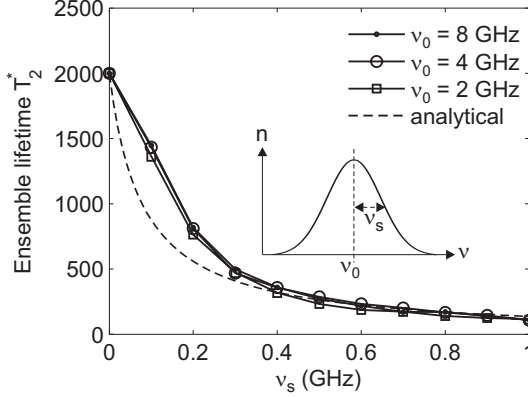


Figure 3.7: Simulation of the ensemble spin coherence time T_2^* as a function of the spread in single spin precession frequency ν . Dashed line: Spin coherence time including a new decoherence rate $2\pi\nu_s$. Inset: We assume a Gaussian distribution of ν , with mean ν_0 and standard deviation ν_s .

3.4.3 Measurement of stray-field-induced modification of spin dynamics

Fits to the experimental data shown in Fig. 3.5a yield precession frequencies of $\nu_{\text{Fe}} = 7.82$ GHz and $\nu_{\text{Au}} = 7.68$ GHz on the Fe and Au grating, respectively. As there is no magnetic stray field originating from the Au grating and provided $B_n = 0$ (see below Sect. 3.4.4), we can determine the stray field averaged over the gap from

$$\langle B_s \rangle = h(\nu_{\text{Fe}} - \nu_{\text{Au}})/g\mu_B = h\Delta\nu/g\mu_B \quad (3.7)$$

to be 21 mT. The same fits also yield $T_2^* = 1510$ ps in the QW below the Au grating and 590 ps below the Fe grating, which is reduced due to averaging effects in the inhomogeneous stray field. Such an effect is confirmed by a simulation shown in Fig. 3.7. We average over $n_0 = 1000$ spins that precess according to Eq. (2.1), but with a Gaussian-distributed ensemble of frequencies ν_i

$$\theta_F(\Delta\tau) = \frac{1}{n_0} \sum_{i=1}^{n_0} \theta_0 e^{-\Delta\tau/T_2} \cos(2\pi\nu_i\Delta\tau). \quad (3.8)$$

Assuming a spin coherence time of $T_2 = 2$ ns for a single spin, the ensemble lifetime is reduced with an increasing frequency-spread ν_s , but not with a change in the center frequency ν_0 . The same result is obtained by assuming that $\nu_s > 0$ introduces a new decoherence rate. After a time τ , defined by $\omega_s\tau = 2\pi\nu_s\tau = 1$, the spins in the ensemble are out of phase. Combining the two rates determined by T_2^{-1} and τ^{-1} , we obtain for the lifetime of the ensemble

$$T_2^* = \left(\frac{1}{T_2} + \frac{1}{\tau} \right)^{-1}, \quad (3.9)$$

shown by a dashed line in Fig. 3.7.

These findings are confirmed in the measurements. As soon as the bar magnetization is saturated, a further increase of B_{ext} increases ν , but does not influence T_2^* (see Fig. 3.9 below). The observed reduction of T_2^* by a factor of ≈ 2.5 corresponds to $\nu_s \approx 0.2$ GHz in Fig. 3.7, which agrees well with the observed increase $\Delta\nu = 0.14$ GHz due to the stray field.

Dependence on B_{ext}

A more systematic study of the dependence on B_{ext} is presented in Fig. 3.8a, showing $\nu_{\text{Fe,Au}} - \nu_0$, with $\nu_0 = g\mu_B B_{\text{ext}}/h$, where $g = 0.520$ has been determined from a fit to ν_{Au} . While ν_{Au} is clearly linear in B_{ext} , the electrons precess faster below the Fe grating by an amount that is proportional to the bar magnetization. The latter has been measured independently with magneto-optical Kerr effect measurements (MOKE), using a continuous-wave laser at a wavelength of 633 nm (bold line in Fig. 3.8a). We suspect that the small linear increase in ν_{Fe} after magnetization saturation is due to a slightly enhanced g -factor in the QW below the Fe grating resulting from unequal strain exerted by the Au and the Fe grating. Assuming different g -factors g_{Fe} and g_{Au} on Fe and Au gratings, the difference in precession frequency $\Delta\nu$ can be expressed as

$$h\Delta\nu = g_{\text{Fe}}\mu_B\langle B_s \rangle + (g_{\text{Fe}} - g_{\text{Au}})\mu_B B_{\text{ext}}. \quad (3.10)$$

For a saturated B_s , $\Delta\nu$ increases with B_{ext} with a slope that is proportional to the difference in g -factors. The slope is larger for wide than for narrow bars, as visible in Fig. 3.8b. A large bar exerts more strain than a small bar and the already enhanced g_{Fe} is further increased.

Dependence on grating geometry

Comparing the different geometries, we verify that a larger B_{ext} is required to fully magnetize the narrow bars compared to the wide bars (Fig. 3.8b), in agreement with room-temperature MOKE measurements (Fig. 3.8c) and numerical simulations (Fig. 3.6a).

In contrast to the expectations from the simulations, we experimentally find the value of $\Delta\nu$ to depend non-monotonically on the gap-size, as visible from Fig. 3.8b and summarized Fig. 3.6b. This was reproduced on two additional samples, and might be explained by non-perfect magnetization of the Fe grating or, as discussed in the next two paragraphs, by an additional field due to nuclear polarization (Sect. 3.4.4), or by inhomogeneous averaging over the gap due to optical/electronic effects (Sect. 3.4.5).

Figure 3.9 shows the spin coherence time T_2^* as a function of B_{ext} . Below the Au-gratings (dashed lines), T_2^* is largely independent of the grating geometry and

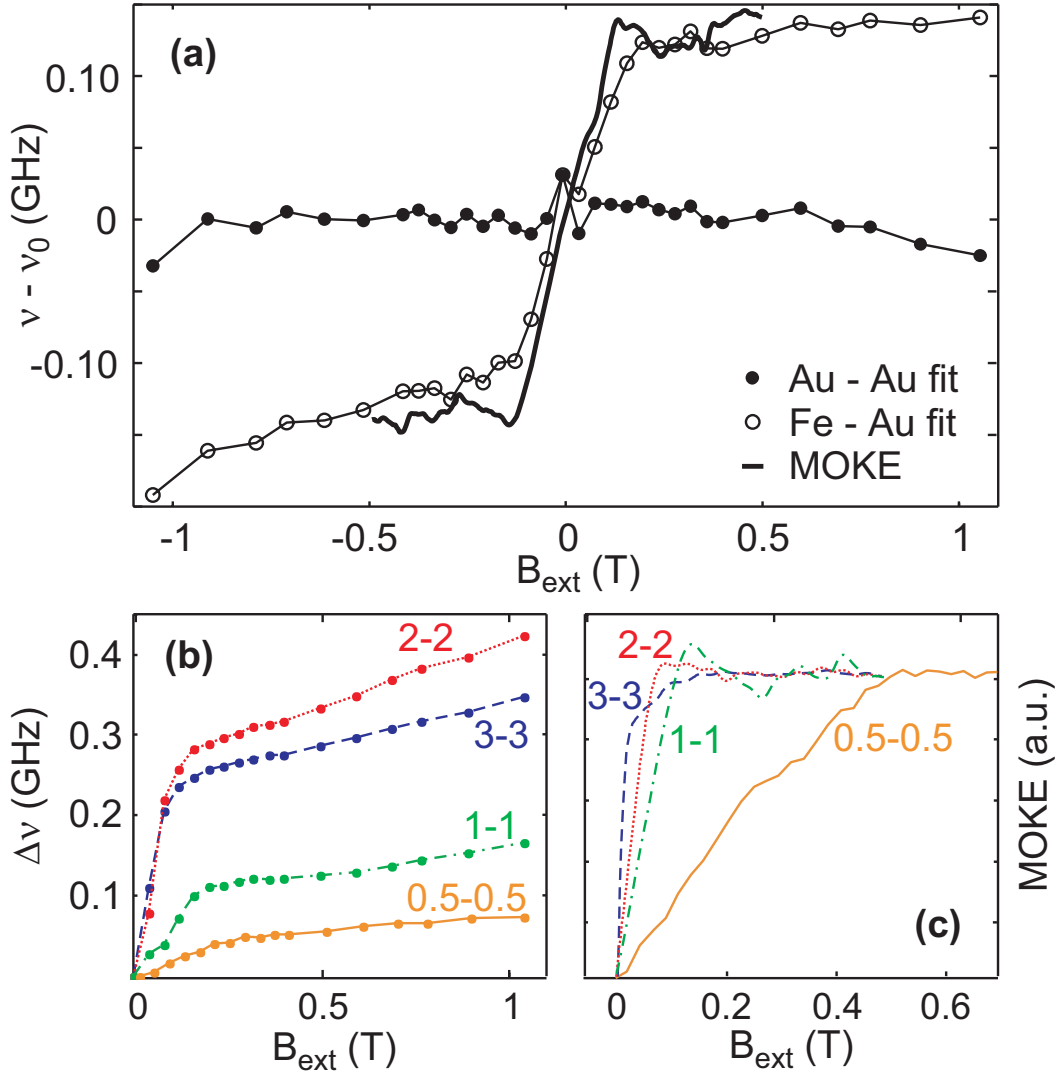


Figure 3.8: (a) Electron precession frequency ν in the QW below the 1-1 Au grating (dots) and below the 1-1 Fe grating (open circles) as a function of B_{ext} . A linear fit to the Au data, $\nu_0(B_{\text{ext}})$, has been subtracted. Electron precession in negative B_{ext} is assigned a negative ν . Bold line: MOKE measurement of the Fe bar magnetization, scaled to fit the y-scale. (b) Precession frequency difference $\Delta\nu = \nu_{\text{Fe}} - \nu_{\text{Au}}$ for all geometries ($T = 40$ K). (c) MOKE measurements for all geometries ($T = 295$ K, background removed and normalized).

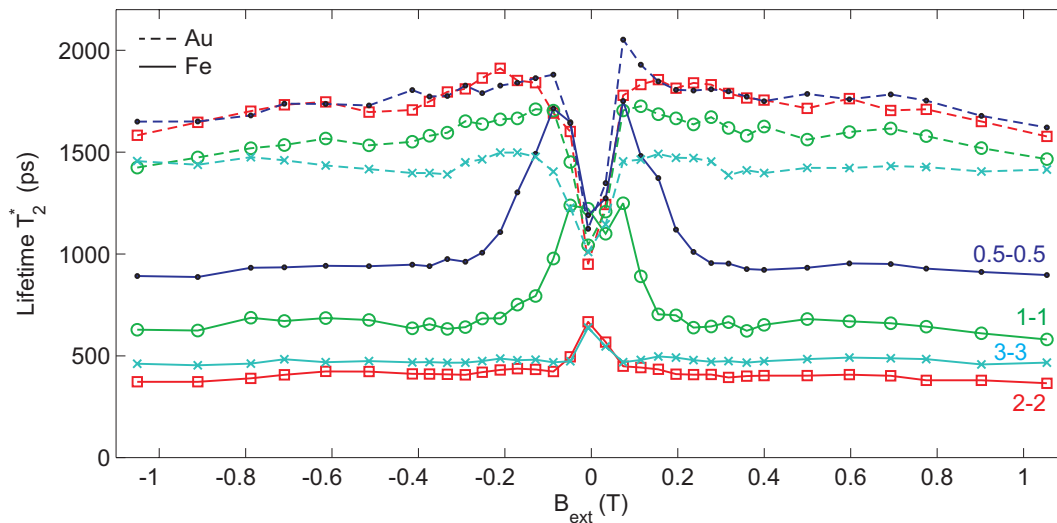


Figure 3.9: Spin lifetime as a function of the external magnetic field B_{ext} for different Au and Fe gratings.

B_{ext} , except around $B_{\text{ext}} = 0$, where the lifetime is reduced. Here, we measure T_1 , and in these samples, $T_1 < T_2^*$ (generally, $T_2 \leq 2T_1$ [39]). Below the Fe-gratings, a reduced lifetime around $B_{\text{ext}} = 0$ is also visible, but it is superimposed on the effect of an increased lifetime, as the stray field along x decreases with the decaying magnetization at low B_{ext} , and the reduced stray-field becomes more homogeneous. As mentioned above, as soon as the magnetization is saturated, T_2^* stays constant. Again, for the small gratings, this happens at higher B_{ext} than for large gratings, because a stronger B_{ext} is needed to align the magnetization along x and to fully build up the stray field.

The relative reduction in lifetime below a Fe-grating compared to below an Au-grating $T_{2,\text{Au}}^*/T_{2,\text{Fe}}^*$ is plotted in Fig. 3.6b. Its dependence on grating geometry is consistent with the argument given in Sect. 3.4.3 and the measured $\langle B_s \rangle \propto \Delta\nu$.

3.4.4 Effects of nuclear polarization and nuclear imprinting

In Eq. (3.6) we have included a contribution from polarized nuclei B_n to the total magnetic field B_{tot} . In the following, we quantify B_n and conclude that the observed increase in ν below the Fe gratings is *not* caused by nuclear magnetic fields.

Generation of nuclear polarization

Electron and nuclear spins are coupled via the hyperfine interaction. This interaction is also called ‘contact interaction’, because it is proportional to the electron wave function squared at the position of the nuclei. Polarized nuclear spins result in

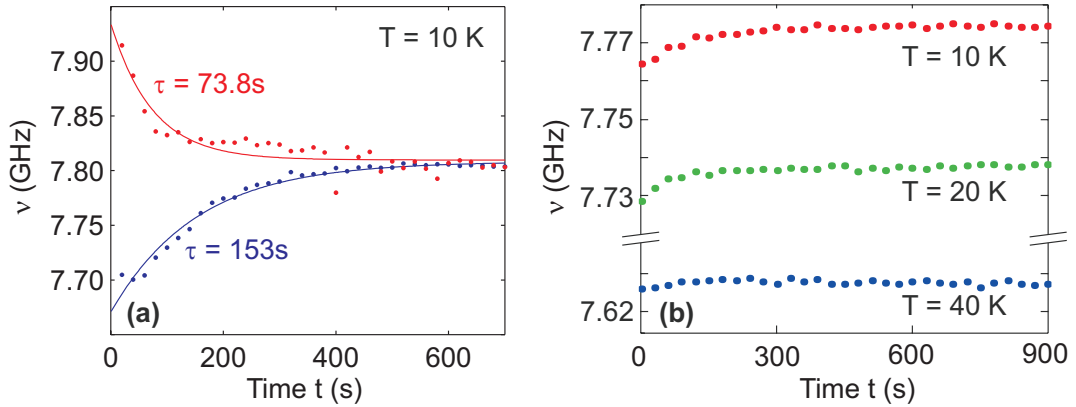


Figure 3.10: **(a)** Decay of nuclear polarization. The sample was illuminated during 10 mins with σ^- or σ^+ -light (red and blue traces). At $t=0$, ν was measured, this time using the PEM. The sample is tilted by $\approx 10^\circ$ with respect to $B_{\text{ext}} = 1$ T. The solid line is a fit to an exponential decay. **(b)** Temperature dependence of the nuclear polarization at $B_{\text{ext}} = 1$ T. Here, the non-tilted sample was in the dark for 10 mins. At $t=0$, $\nu(t)$ was measured using the PEM.

an effective magnetic field acting on electron spins². On the other hand, optically polarized electron spins can polarize nuclei by the following two processes [25].

Dynamic nuclear polarization (DNP) When pumping the electron spins into a non-equilibrium (i.e. polarized) state, the contact interaction leads to a polarization of nuclear spins. In our geometry, the electron spins and therewith also the nuclear spins are polarized along z (see Sect. 3.4.1). Our measurement setup, however, is only sensitive to magnetic fields along x (or y). Therefore, DNP manifests only when the sample is tilted (10° around y in Fig. 3.10a).

Overhauser effect When electrons are artificially maintained in a disordered state, they try to align according to their thermal equilibrium by flipping spins with nuclei. Such a disordered state is achieved in our experiment by polarizing the electron spins along z , while in thermal equilibrium, they would (partly) be polarized along B_{ext} , i.e. along x .

Common to both effects is the appearance of nuclear time scales. Nuclear polarization in bulk and QW systems builds up and relaxes within seconds to minutes, remarkably different to electron spin polarization. By observing the electron spin precession over minutes, we attribute long-time changes in ν to a nuclear magnetic field B_n .

²Of course, also polarized electrons exert an effective magnetic field on the nuclei. Such a field leads to a shift in nuclear magnetic resonance, called ‘Knight shift’. The corresponding effect in electron spin resonance is called ‘Overhauser shift’.

Measurements of nuclear fields

To polarize the nuclear spins we first illuminated the tilted sample with light ($P = 1$ mW) of constant helicity (either σ^- or σ^+) over a time of 10 minutes. During this time, a nuclear polarization builds up due to DNP, and the precession frequency is enhanced or reduced, depending on the helicity and the direction of the external magnetic field. Then, at $t = 0$, the σ^\pm light was switched off, and we started a series of fast TRFR sweeps with a PEM, which is expected to influence the nuclear polarization only weakly (see below). The observed $\nu(t)$ is plotted in Fig. 3.10a. On the timescale of minutes, ν relaxes to a value of $\nu(t \rightarrow \infty) = 7.81$ GHz, independent of the helicity of the light initially used. We ascribe this to the decay of a nuclear polarization that was built up when optically pumping the sample with circularly polarized light [77, 78]. Again assuming that the PEM does not influence the nuclear polarization (see below), we argue that at $t \rightarrow \infty$ no nuclear polarization is present anymore. Then, the magnetic field B_n induced by the nuclear polarization present at $t = 0$ changed ν by ± 130 MHz. This corresponds to $B_n = \pm 19$ mT or a nuclear polarization of 0.35% if taking $B_n = 5.3$ T as a maximum nuclear field [79].

Preventing nuclear polarization

Since the frequency of 50 kHz, at which the PEM switches between σ^+ and σ^- , is much faster than the timescale of the nuclear polarization, we expect $B_n \approx 0$ when measuring TRFR with the PEM. This is verified in Fig. 3.10b with a non-tilted sample. After the sample has been in the dark for at least 10 minutes, fast TRFR-scans were performed. Electron precession becomes faster on a time scale of minutes, which we attribute to an increasing nuclear polarization due to the Overhauser effect. However, the increase is on the order of 5 MHz, thus greatly reduced compared to the case of constant helicity. Additionally, this value can be almost zeroed by increasing the temperature to 40 K. In order to minimize effects of nuclear polarization, we performed all measurements shown here at a temperature of 40 K and using a PEM, modulating the photon helicity at 50 kHz.

Nuclear imprinting

We can further exclude effects of ferromagnetic imprinting [80–82] to account for the observed difference: a transparent, 7 nm thick Fe film evaporated on our sample with the same technique as used for the gratings did not affect ν in the QW (not shown). This is not surprising, since ferromagnetic imprinting can only occur at a ferromagnet-semiconductor junction [83, 84], and is not expected to happen through the 20 nm GaAs cap separating the QW from the ferromagnetic gate.

Also, we have measured curves similar to the one in Fig. 3.8b at temperatures between 10 K and 80 K and found a maximum relative variation of $\Delta\nu$ of 10%,

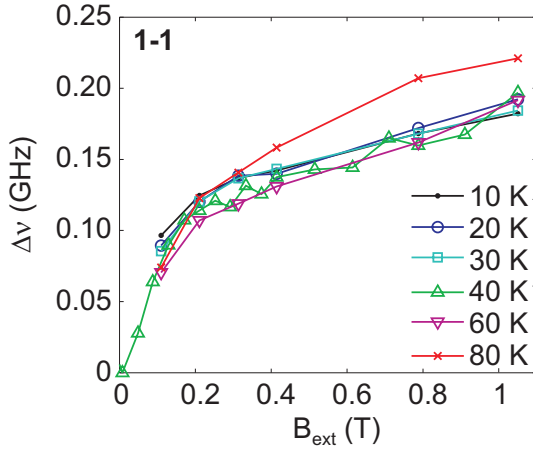


Figure 3.11: Temperature dependence of the stray field measurement on a 1-1 grating.

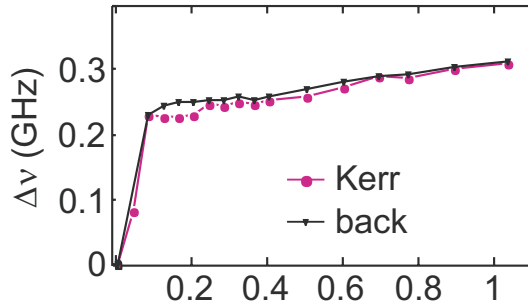


Figure 3.12: Measurement of $\Delta\nu$ on the 3-3 grating with different set-ups: Kerr geometry (reflected probe) and Faraday geometry from the sample's backside.

as visible in Fig. 3.11. If nuclear effects influenced $\Delta\nu$, a strong dependence on temperature would be expected.

3.4.5 Optical diffraction at the grating

In the simulation presented in Sect. 3.4.2, the stray field is sampled uniformly in the gap between the Fe bars. In the experiment, diffraction and near-field optical effects including surface plasmons [85, 86] may lead to a non-uniform intensity distribution of pump and probe pulses in the gap.

As a consequence, the excitation of electrons in the gap by the pump pulse may be inhomogeneous, possibly also due to an inhomogeneous circular polarization. In-between the pump and the probe pulse, in-plane electric fields originating from the strain or contact potential of the metallic bars may lead to a lateral redistribution of the electrons on a picosecond time scale. And lastly, the Faraday rotation of the transmitted probe beam may probe the electron spin distribution in an inhomogeneous way.

These deviations are most important at the boundary of the Fe bars where the stray field is strongly non-uniform, and where the x -component even changes

sign, which could explain the discrepancy between the experimental results and the simplified simulation, previously shown in Fig. 3.6b.

In Fig. 3.12, we show $\Delta\nu$ measured in different set-ups, where optical diffraction might manifest differently. In addition to TRFR, we measured the spin dynamics in Kerr geometry, where the reflected instead of the transmitted probe beam is analyzed. The $\Delta\nu$ obtained this way looks very similar to the data presented in Fig. 3.8b. Surprisingly, also TRFR from the backside, where the beams first pass the QW before they are diffracted by the grating, gives similar results.

Simulations of the QW illumination below a grating

In order to further investigate the role of probe diffraction, we measured ν in different geometries and polarization configurations. A numerical simulation (obtained with the ‘finite-difference time-domain’ method) assuming a vanishing electric field of the radiation on the metallic bar is shown in Fig. 3.13. Below the metallic gates (indicated in gray) of the 0.5-0.5 and 1-1-gratings, the light intensity does not immediately vanish, and especially for the probe beam polarization perpendicular to the bars, a substantial part of the QW covered by a gate is illuminated. The simulations predict pronounced differences in the illumination of these areas depending on the probe beam polarization.

Below the 2-2 and the 3-3-grating, the light intensity distribution is enhanced close to a bar edge, where the stray field is high, independent of the polarization. Those regions are thus probed more in the optical average by the probe pulse, and the measured $\langle B_s \rangle$ is expected to be larger than the homogeneous average performed in Sect. 3.4.2. So far, this explains the ‘too large’ $\langle B_s \rangle$ measured for the 2-2 and 3-3-gratings.

We did, however, not observe a different $\langle B_s \rangle$ for the probe beam polarized parallel or perpendicular to the bars, as suggested by the simulations for the small 0.5-0.5 and 1-1-gratings. Further investigations with gated gratings presented later in Sect. 4.1 suggest that the QW area probed below the bars of a small grating is larger than indicated by the simulations shown here, possibly due to surface plasmonic effects leading to an enhanced transmission. The stray field pointing in negative x -direction in these areas reduces the average stray field considerably.

3.4.6 Gratings with larger gap than bar size

In the simulations in Sect. 3.4.2, we have already discussed that the average stray field should decrease with increasing gap width. However, we found a non-monotonic relationship between bar/gap width and the measured stray field for gratings with equal bar width b and gap width a . For small $b = 0.5$ and $1 \mu\text{m}$, the stray field measured was smaller than expected, for large $b = 2$ and $3 \mu\text{m}$, it was larger. The

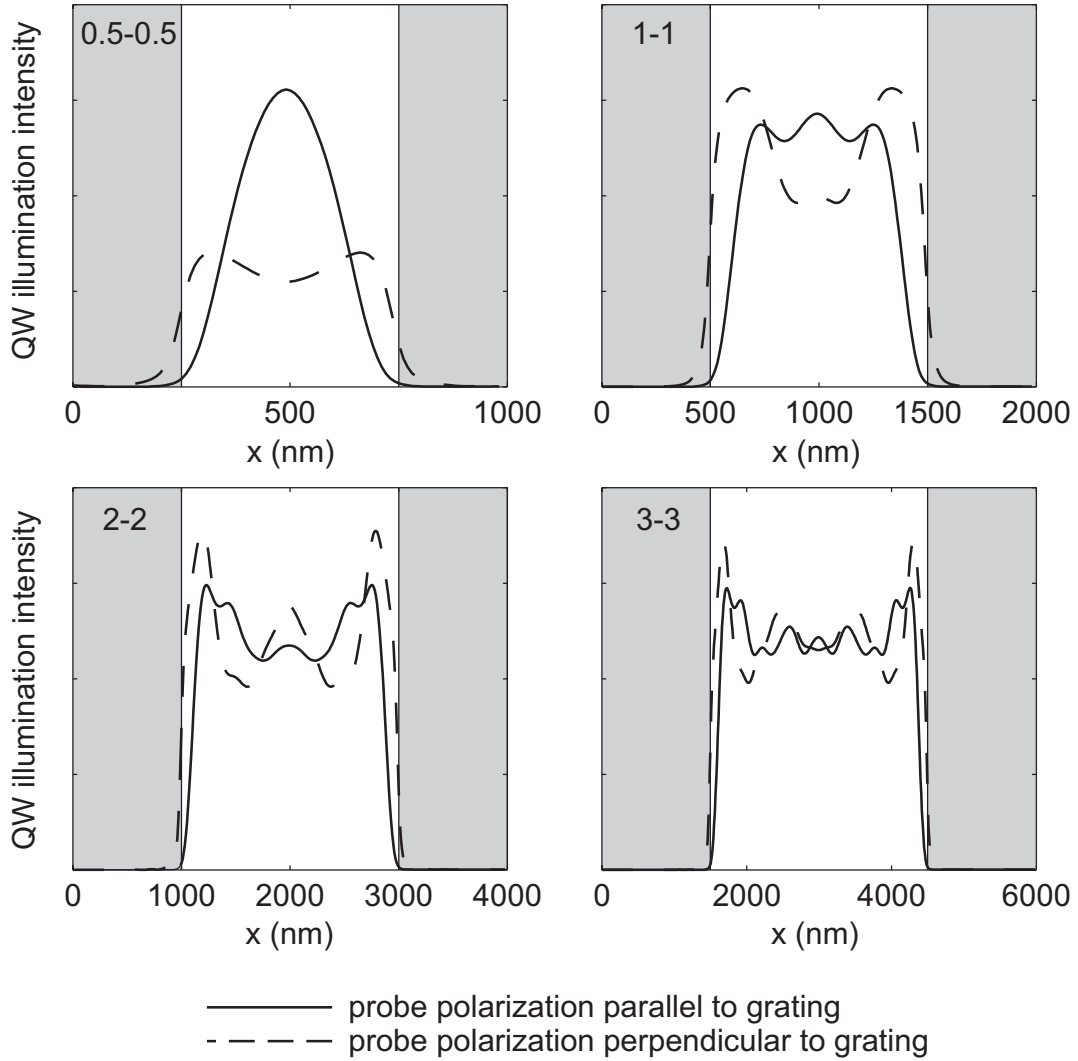


Figure 3.13: Simulated probe intensity below a grating for linearly polarized light, E -field parallel (solid line) and perpendicular (dashed line) to the bars. The smaller the bars, the more QW is illuminated below the bars. The shaded areas indicate the parts of the quantum well that are covered by a gate.

latter could be explained by simulations of the light intensity distribution below a grating.

Figure 3.14 shows measurements of the stray-field-induced change in spin precession frequency $\Delta\nu$ for gratings with twice ($a = 2b$) or three times ($a = 3b$) larger gap than bar width. For comparison, we also plot $\Delta\nu$ for equal gap and bar width ($a = b$).

In the non-saturated regime, $\Delta\nu$ builds up similarly for all geometries and reaches its saturation value at the same external magnetic field B_{ext} . This is not surprising, since the magnetization build-up depends only on b and not on a .

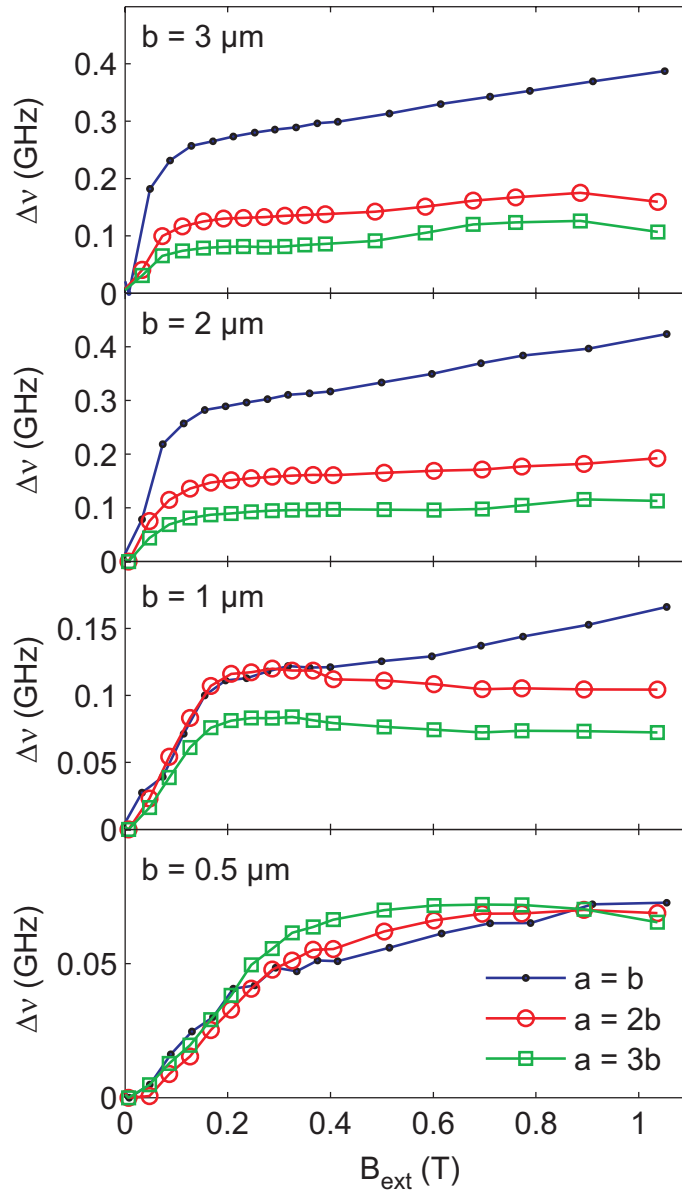


Figure 3.14: Stray-field-induced change in electron precession frequency for gratings with gap widths a 1, 2 or 3 times the bar width b .

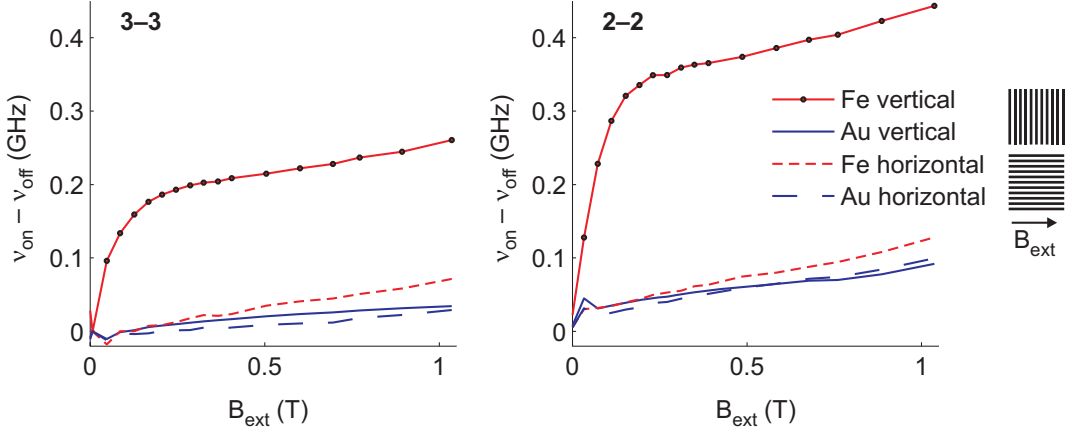


Figure 3.15: Magnetic stray-field-effect on the electron precession frequency ν_{on} of 3-3 and 2-2 gratings for parallel (‘horizontal’) and perpendicular (‘vertical’) orientation of the external magnetic field B_{ext} to the bars’ easy axis. The electron precession frequency beside a grating ν_{off} has been subtracted. The data points measured are indicated on the ‘Fe vertical’ curve.

For $b = 3 \mu\text{m}$ and for $b = 2 \mu\text{m}$, $\Delta\nu$ is reduced for $a = 2b$ and $a = 3b$. Assuming an intensity distribution as previously calculated, we expect a ‘too high’ $\langle B_s \rangle$ for $b = 2$ and $3 \mu\text{m}$ and a reduction of the saturated $\Delta\nu$ by a factor of 2 for the $a = 2b$ -grating and by a factor of 3 for the $a = 3b$ -grating compared to the $a = b$ -grating. This is also observed in the measured data.

For $b = 1 \mu\text{m}$ and for $b = 0.5 \mu\text{m}$, however, $\Delta\nu$ is only slightly reduced ($b = 1 \mu\text{m}$) or does not change at all ($b = 0.5 \mu\text{m}$) with wider gaps. For those small bars, again, we suggest the presence of enhanced transmission leading to illumination of regions below the bars and a reduction of $\langle B_s \rangle$ as mentioned earlier. With larger a , these effects are expected to diminish, since they are only present when the spatial dimensions involved are on the order of (or smaller than) the laser wavelength (870 nm). This would lead to a larger $\Delta\nu$ with increasing a , but at the same time, due to the larger gap proportion with vanishing stray field included in the average, a larger a also leads to a decrease of $\Delta\nu$, as explained for the $b = 3$ and $2 \mu\text{m}$ gratings above. The two effects seem to cancel exactly for $b = 0.5 \mu\text{m}$.

We further note that the strain-induced increase of the g -factor (see Sect. 3.4.3), visible from the slope of $\Delta\nu$ in the saturated regime, is more pronounced for small gaps $a = b$. This seems reasonable, since strain emerges from the bars and is expected to decline with distance.

3.4.7 Horizontal and vertical gratings

In the measurements presented up to now, we have always compared ν on a Fe grating with ν on a non-magnetic Au grating, in order to measure the stray-field-

induced change in ν . It is also possible to measure this $\Delta\nu$ by comparing ν on two Fe gratings, one oriented perpendicular to B_{ext} , the other with the bars' easy axis parallel to B_{ext} . Since our B_{ext} is horizontal, we call the latter gratings 'horizontal', and the former 'vertical'.

For the horizontal gratings, virtually no stray field is induced in the gap and we do not expect to see any change in ν due to the magnetization. The measured ν_{on} is plotted in Fig. 3.15. An offset ν_{off} , the precession frequency beside a grating, has been subtracted. While $\nu_{\text{on}} - \nu_{\text{off}}$ for horizontal and vertical Au gratings is very similar, the effect of the stray field is well visible for the vertical Fe grating. Again, slightly modified g -factors due to strain are visible, $g_{\text{Fe}} > g_{\text{Au}} > g_{\text{off}}$.

This measurement was not performed with the 1-1 and the 05-05 gratings, since due to the vertically offset alignment of our pump and probe beams, the diffraction occurring at the horizontal gratings leads to scattering of the pump beam into the probe detection. This scattering and where the pump beam is deflected to depends on the grating period.

3.4.8 Spatially resolved measurements

To get an impression of the spatial distribution of the stray field, we performed two-dimensional scans over a grating and its surroundings. Since the focus diameter of our laser beam ($15 \mu\text{m}$) is much larger than the grating periodicity of $1 - 6 \mu\text{m}$, we do not expect to see the individual bars in our measurements. This is only possible for larger grating periods, as shown later for a gated 3-9-grating in Fig. 4.6.

In Fig. 3.16, we show images representing the spin precession frequency ν , the spin coherence time T_2^* and the transmitted probe power in the x/y plane around a 3-3 Fe and Au grating. In the transmitted power plot (bottom row), the location of the gratings is visible, including two wire-gates. In the top row, ν is shown to be very homogeneous on both the Fe and the Au grating. Again, a slightly enhanced g_{Au} is observed when comparing ν on the Au grating and in its surroundings. In the middle row, the spin coherence time is plotted. As already mentioned previously, it is reduced on the Fe grating due to averaging effects (see Sect. 3.4.3).

3.5 Stray field measurements on etched gratings

To eliminate the probing of 'negative' stray fields below the Fe bars, we etched the gates down to the QW. In this configuration, the stray field is probed in the plane of the gratings and not below the gratings, as previously illustrated by the shaded region in Fig. 3.5b. From the same figure it is also visible that the stray field is now almost perfectly aligned along x and the z -components virtually vanish. Besides these advantages, the average field is enhanced by a factor of between 2 and 3 on an

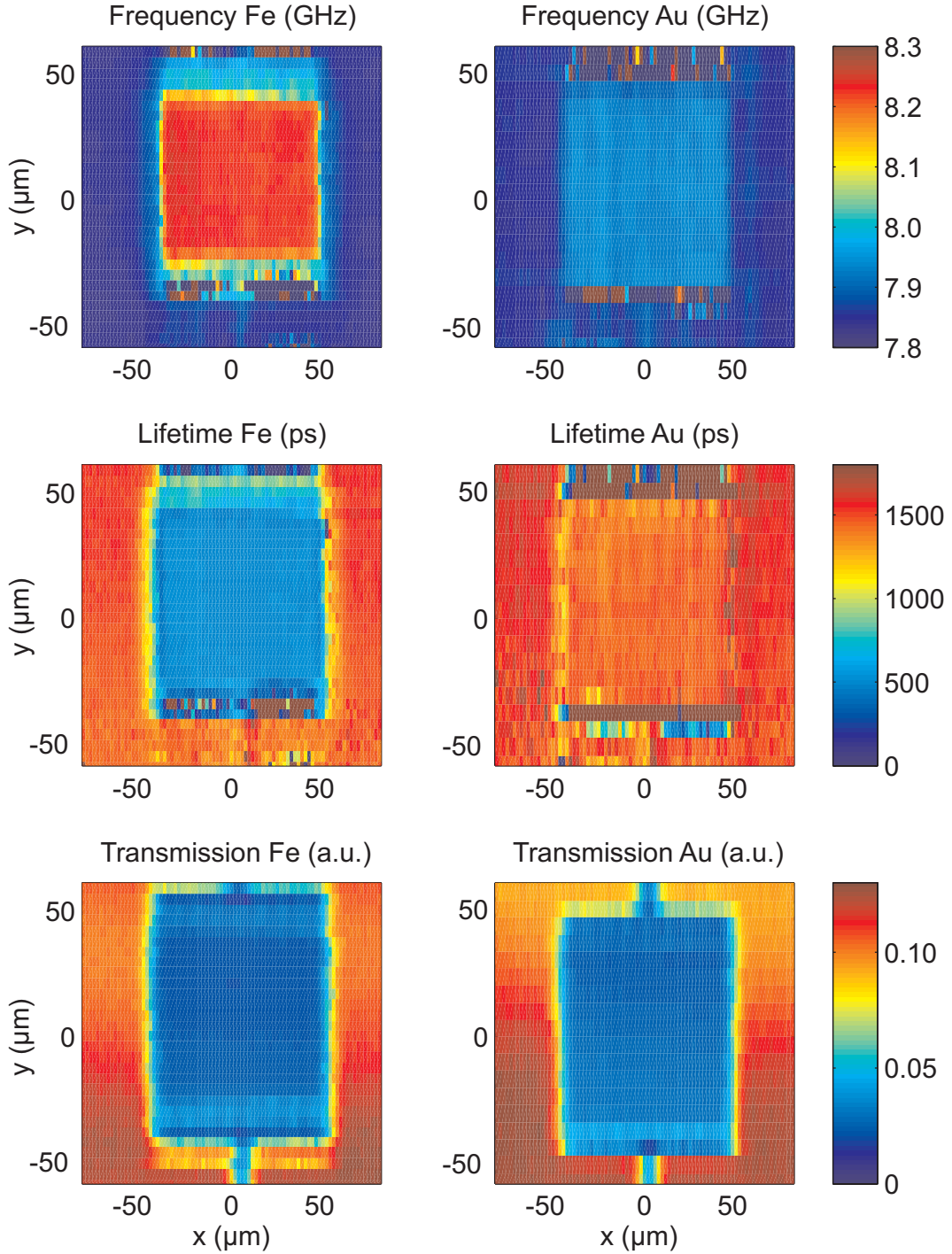


Figure 3.16: Two-dimensional scans over a 3-3 Fe (left column) and Au (right column) grating at $B_{\text{ext}} = 1$ T. On the Fe grating, the electron precession frequency ν is enhanced due to the magnetic stray field, on the corresponding Au grating, ν is only slightly higher compared to beside the grating, presumably because of a modified g -factor due to strain. The spin coherence time is reduced by a factor of ≈ 3 on the Fe grating and virtually unchanged on the Au grating. The transmitted laser power shows the position of the gratings. For a SEM-image of a similar grating, see Fig. 3.4.

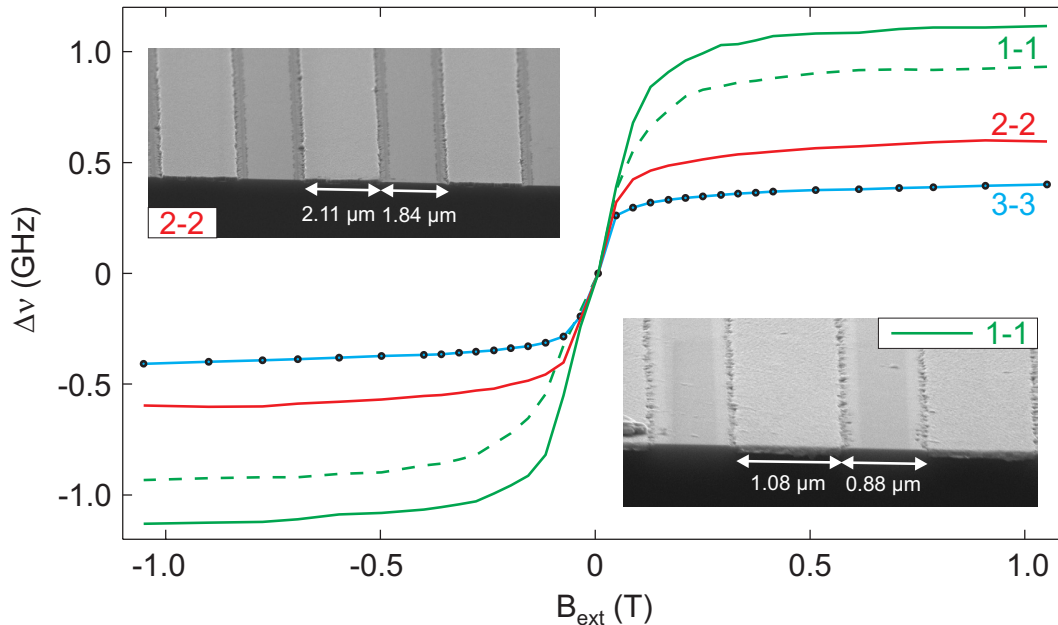


Figure 3.17: Stray field effect on the electron spin precession frequency for gratings etched down to the QW. For the measurements represented by solid lines, the gratings had slightly too wide bars and too small gaps, as shown in the insets. The dashed line shows the data for a grating, where the widths of the bars has been corrected for the widening influence of the etching process. Dots on the 3-3-curve indicate the magnetic field steps.

etched compared to a non-etched grating, see the simulations in Figs. 3.18 (etched) and 3.6 (non-etched).

Using the etching process described in Sect. 2.6.3, we etched away ≈ 80 nm of GaAs prior to evaporating the metal. That way, the bars are buried in the GaAs and centered in the QW layer.

The stray-field-induced change in spin precession frequency $\Delta\nu$ is shown in Fig. 3.17. Now, the smallest grating (1-1) exhibits the largest stray-field effect, and the largest grating (3-3) the lowest. The magnetization builds up as expected, for 1-1 the largest B_{ext} is needed to saturate the bar magnetization.

When comparing with simulations (Fig. 3.18), the agreement is satisfactory. Only the absolute magnitude of the stray field appears too high in the measurement. This can partly be attributed to the Fe bars, which are slightly too wide and the gaps, which are too narrow (inset in Fig. 3.17). During the etching process, the upper layer of the two-layer PMMA-resist gets slightly etched laterally, resulting in a widened bar. Measurements of $\Delta\nu$ for a 1-1 grating with improved mask geometry (smaller bars were written) are shown by the dashed line in Fig. 3.17. For this sample, the predicted and the measured value differ by about 20%. Such an enhancement of $\Delta\nu$ can again be attributed to similar effects as on the non-etched structures, where

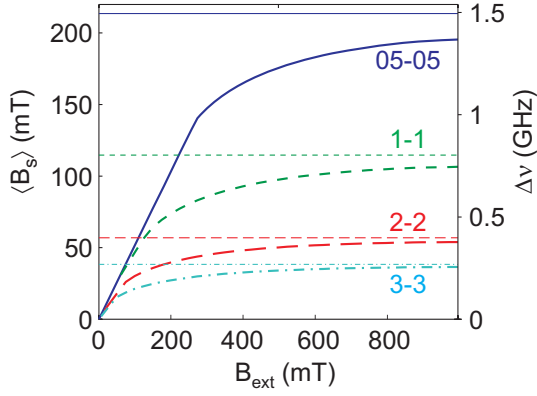


Figure 3.18: Numerically calculated stray field of an etched grating as a function of B_{ext} . The stray field was homogeneously averaged over the gap width, the left scale indicates the averaged value, the right scale the corresponding change in precession frequency. Horizontal lines indicate $\langle B_s \rangle$ for homogeneously magnetized bars.

the light intensity is enhanced close to the metal bars due to diffraction and surface plasmonic effects.

Chapter 4

Spin manipulation with magnetic and electric fields

The experiments presented in chapter 3 were static, and the stray-field-induced electron spin precession could not be influenced externally. In this chapter, gate voltages are applied to the ferromagnetic gratings and the electrons are spatially moved in the inhomogeneous stray field, resulting in electrical control on the electron spin precession. First, measurements with static gate voltages are presented (Sect. 4.1). Secondly, the gate voltages are modulated on a nanosecond timescale (Sect. 4.2)¹

4.1 Gated gratings

4.1.1 Overview

In this section, we extend the experiments presented in Sect. 3.4 by applying gate voltages to the Fe bars. Thereby we move the electrons in the inhomogeneous stray field and gain electrical control of the electron spin precession.

By employing TRFR, we track the electron spin precession in the QW below an array of ferromagnetic bars made of Fe. In an external magnetic field of sufficient strength to magnetize the Fe bars, the magnetic stray field B_s makes the electron spins precess faster than below an identical grating made out of non-magnetic Au, as shown in the previous Sect. 3.4. By applying a ‘symmetric’ gate voltage V_g with opposite sign to neighboring bars of an interdigitated grating (see Fig. 3.4 for an SEM-image), the electron distribution in the QW is moved within the inhomogeneous stray field, and precesses in a higher or lower mean stray field. The application of a voltage of $V_g = \pm 1$ V to a grating with a period of 1 μm leads to an increase in the electron spin precession frequency ν by up to 0.5 GHz, corresponding to a mag-

¹Parts of this chapter have been published in L. Meier *et al.*, Phys. Rev. B **74**, 245318 (2006)

netic field of ≈ 70 mT. By modulating the gate voltage with gigahertz frequencies, we achieve control of the electron precession frequency on the nanosecond timescale, see the following Sect. 4.2.

We use the samples presented in Sect. 3.4, with substrate P805 (see Sect. 2.5) and arrays of 80 nm thick Fe (Au) bars evaporated on the surface by electron-beam lithography and standard lift-off processes (see Sect. 2.6.2). Neighboring bars have separate electrical connections, so that they can be put on different potentials. We have fabricated interdigitated gratings $100 \mu\text{m} \times 100 \mu\text{m}$ in size having periods p of 1, 2, and 4 μm and a bar width of half the period (called 0.5-0.5, 1-1 and 2-2 gratings in chapter c3).

We use TRFR at $T = 40$ K to trace the electron spin precession in the QW (c.f. Sect. 2.1). As our laser focus (15 μm in diameter) is much larger than the grating period, we measure the electron spin precession averaged over an ensemble of spins which precess in an inhomogeneous magnetic field. This spatial average is determined by the laser field distribution below the grating, which acts as an optical mask, as well as by the electron distribution within the illuminated regions of the QW (see Sect. 3.4.5). $\langle B_s \rangle$ is the spatially averaged B_s that results from these optical and electronic effects.

4.1.2 Sweeps of B_{ext} at different gate voltages

A numerical simulation of B_s (obtained as described in Sect. 3.3) is shown in Fig. 4.1a, similar to Fig. 3.5b but for half the bar/gap size. The stray field in the center of the QW is expected to be ≈ 200 mT close to a Fe bar and ≈ 50 mT in the middle of the gap. The x -component, which our measurement geometry is most sensitive to, changes sign at the edge of a bar. It is parallel to B_{ext} between the bars and antiparallel below a bar.

Figure 4.1b shows for different V_g the dependence of ν on B_{ext} with a linear background $\nu_0 = g_{\text{Fe,Au}}\mu_B B_{\text{ext}}$ subtracted ($g_{\text{Au}} = 0.5179$, $g_{\text{Fe}} = 0.5163$). We first focus on the data for $V_g = 0$ V. While on the sample with the Au grating, $\nu - \nu_0 \approx 0$ independent of B_{ext} , $\nu - \nu_0$ on the Fe sample increases linearly up to $|B_{\text{ext}}| \approx 0.3$ T. For $|B_{\text{ext}}| > 0.3$ T, $\nu - \nu_0$ remains constant at about 0.05 GHz, corresponding to an average stray field of ≈ 7 mT. Magneto-optical Kerr measurements confirm that at this external field, the magnetization of the Fe grating (and with it the stray field) saturates, as previously shown in Fig. 3.8. Simulations assuming a homogeneous electron distribution and illumination between the bars and no illumination below the bars predict $\langle B_s \rangle$ on the order of 100 mT. We ascribe the difference to the probing of negative stray fields antiparallel to B_{ext} below the Fe bars owing to optical diffraction and surface plasmonic effects at the grating (as $p \sim \lambda$) and to non-perfect magnetization of the Fe bars due to edge roughness (see Sect. 3.4).

When applying a voltage of ± 1 V (± 2 V) to neighboring bars, the electrons

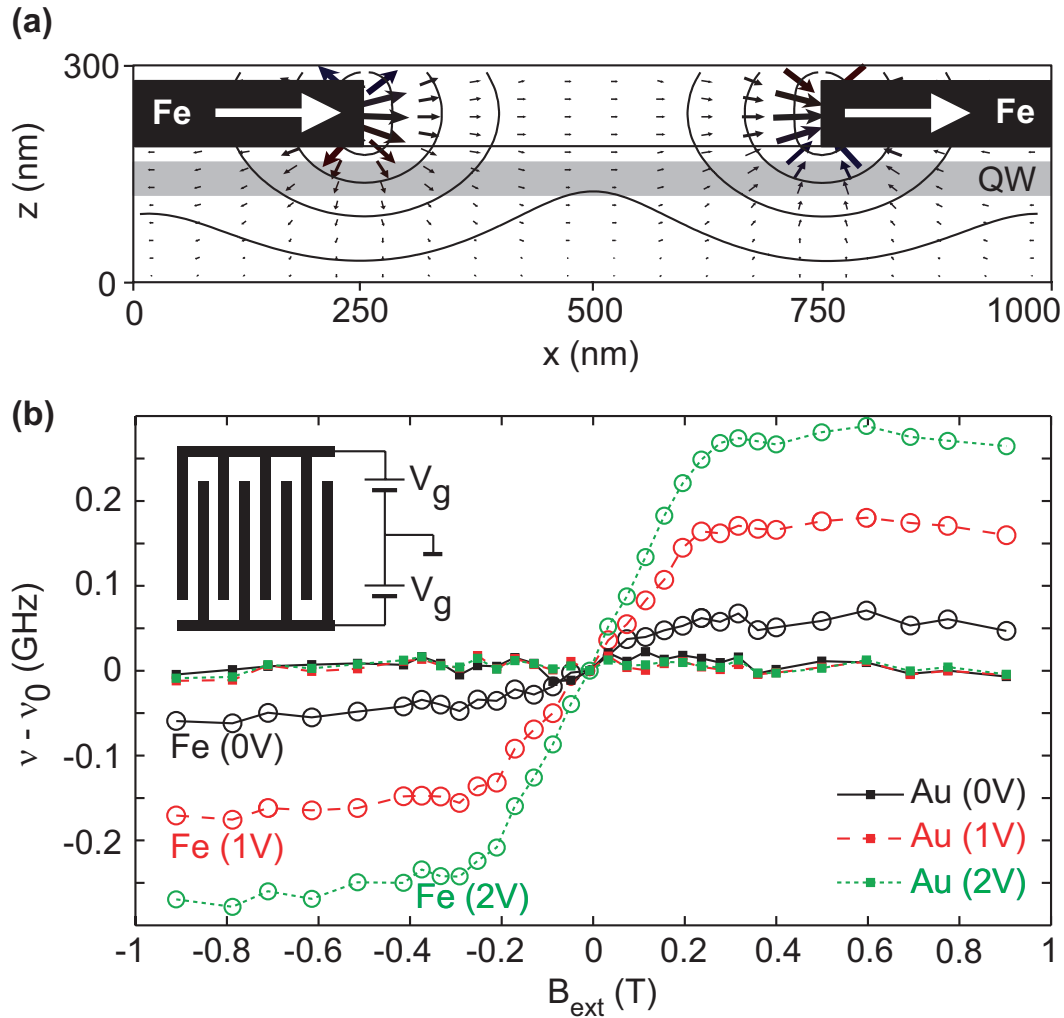


Figure 4.1: **(a)** Micro-magnetic simulation of the magnetic stray field of a grating with period $1 \mu\text{m}$. The solid lines of constant field indicate magnetic fields of 500, 200, 100, and 50 mT. The QW is shaded gray. **(b)** Electron precession frequency ν in the QW below the $1 \mu\text{m}$ grating for different gate voltages as a function of B_{ext} . A linear fit $\nu_0 = g_{\text{Fe,Au}}\mu_B B_{\text{ext}}$ to the data has been subtracted (for Fe the fit only included the saturated region $|B_{\text{ext}}| > 0.3 \text{ T}$). Inset: sketch of an interdigitated grating, gated with a ‘symmetric’ gate voltage V_g .

precess 0.15 GHz (0.25 GHz) faster on the Fe sample than on the Au sample in the saturated region, corresponding to $\langle B_s \rangle = 20$ mT (34 mT). Note that $\nu - \nu_0$ builds up similarly for all voltage traces. In particular it saturates at the same value of B_{ext} . This indicates that the same stray field is probed with a different spatial averaging for different gate voltages. The spin lifetime T_2^* decreases slightly with an applied gate voltage (see later Fig. 4.3c), also indicating a change in spatial averaging and a larger spread in ν , as mentioned above in Sect. 3.4.3.

4.1.3 Gate sweeps at constant magnetic field

Overview

To study the tunability of ν with V_g , we set B_{ext} to 1.05 T, where the magnetization of the Fe bars is saturated, and vary V_g in small steps. Figure 4.2a shows $\nu(V_g)$ for Fe and Au gratings and three different geometries. On samples with Fe gratings, ν is enhanced by a few tenths of a gigahertz as $|V_g|$ is increased. The steepest slope for the $p = 1$ -grating around $V_g = 0.7$ V corresponds to a tunability $\partial\nu/\partial V_g \approx 0.5$ GHz/V. In samples with Au gratings, ν changes little with V_g , the small offsets in ν_{Au} for different p are ascribed to small variations in g due to strain from the grating. Fits yield $g_{\text{Au}}^{1,2,4\mu\text{m}} = 0.5211, 0.5225, \text{ and } 0.5253$.

Probing a single gap

When probing a single $2 \mu\text{m}$ wide gap between two large, electrically contacted Fe (Au) gates (data not shown), we find a very similar behavior in $\nu(V_g)$ as in the case of the Fe (Au) grating with $p = 4 \mu\text{m}$ (i.e., $2 \mu\text{m}$ bar and $2 \mu\text{m}$ gap). Hence, measuring a grating is equivalent to measuring a single gap, but the grating enhances the signal-to-noise ratio considerably. Specifically, in both cases, the sign of the x -component of the electric field is not of importance: in a single gap the electric field always points in one direction, whereas on a grating, we average over fields pointing in the x - and in the $-x$ -direction.

Origin of the tunability on Fe gratings

In Fe samples, the increase in ν with V_g is more pronounced for gratings with smaller p , whereas the stray-field effect on ν at $V_g = 0$ is larger for gratings with large p . The latter was discussed in detail in Sect. 3.4.

The understanding of these two observations is facilitated by investigating a mixed Fe/Au grating, in which every other Fe bar has been replaced by a Au bar. As long as a negative V_g is applied to the Fe bars, $\nu(V_g)$ obtained is similar to $\nu(V_g)$ of the pure Fe sample, see Fig. 4.2b. However, a positive voltage applied to the Fe

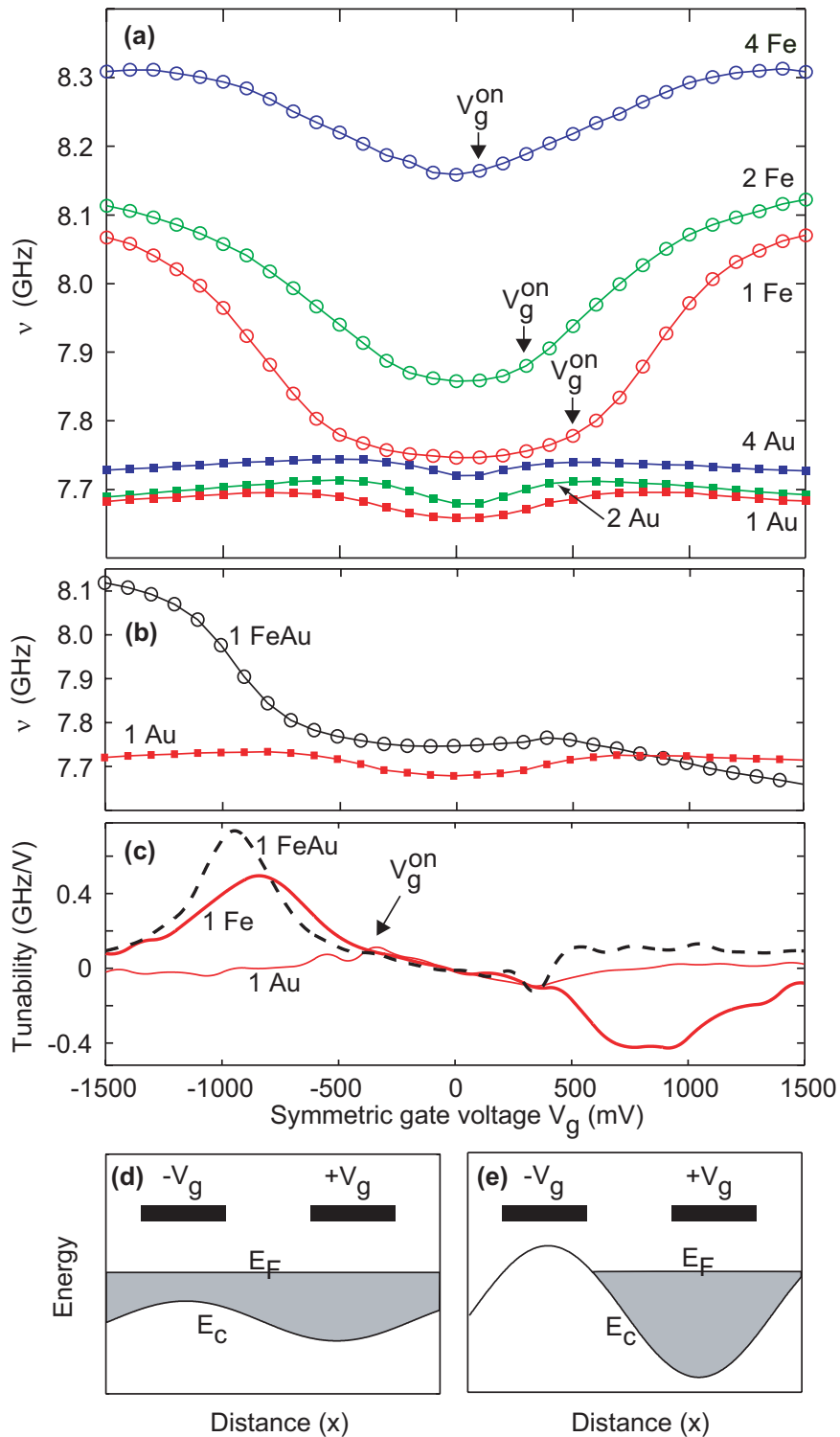


Figure 4.2: **(a)** Electron precession frequency ν at $B_{\text{ext}} = 1.05$ T as a function of V_g . **(b)** $\nu(V_g)$ for a Au and a mixed Fe/Au grating (V_g is applied to the Fe bars, $-V_g$ to the Au bars). **(c)** Gate tunability of the electron precession frequency $\partial\nu/\partial V_g$ as a function of V_g . **(d)** and **(e)** Schematic conduction band modulation and Fermi energy E_F in the QW for (d) a small $|V_g| < V_g^{\text{on}}$ and (e) a large gate voltage $|V_g| > V_g^{\text{on}}$.

bars leads to a *decrease* of ν on the mixed Fe/Au sample below the value on the reference Au sample, indicating that the stray field effectively reduces B_{tot} . Thus, the contribution to the stray-field-average of regions below a positively charged Fe bar is in fact (slightly) *negative*. The ‘negative’ stray field below the positively charged bar, directed along $-x$, is weighed more than the ‘positive’ stray field beside the bar (see Fig. 4.1a above for a sketch of the stray field). In contrast, below a negatively charged Fe bar, contributions from the positive stray field beside the bar dominate. This dependence of the probed regions on the gate voltage is explained by the depletion of electrons below the negatively charged Fe bar, as explained in the next paragraph.

TRFR dependence on the electron density

TRFR relies on the circular birefringence at the absorption edge of the QW (see Sect. 2.1.2). Spin polarization leads to different Fermi energies for spin-up and spin-down electrons $E_F^{\uparrow,\downarrow}$ (Fig. 2.2). The TRFR signal is proportional to $\Delta E_F = E_F^{\uparrow} - E_F^{\downarrow}$ (here $\Delta E_F \approx 0.05 E_F \approx 2$ meV), i.e. to the optically excited, polarized electrons and not to the total electron density.

A positively charged bar leads to an accumulation of electrons below the bar, but as just stated, the resulting higher electron density does not enhance the TRFR signal. However, when a bar is negatively charged and all electrons are depleted from below the bar, then no electrons from this region will contribute anymore to the TRFR signal and to the averaged ν [see Fig. 4.2d and e].

The smaller p , the more diffraction and surface plasmonic effects lead to a probing of negative stray fields below a Fe bar, resulting in a smaller ν , as discussed in Sect. 3.4.5. Returning to the pure Fe grating, applying $\pm V_g$ to a pair of neighboring bars has no effect on the sampling of the stray field close to the bar at $+V_g$, but removes contributions from electron spins in the negative stray field below the bar at $-V_g$, which results in an overall increase of ν . The larger the sampled region below a bar (i.e., the smaller p), the larger the increase in ν when this region is depleted below the negatively charged bar. This explains the larger tunability $\partial\nu/\partial V_g$ for smaller p .

More data on the mixed Fe/Au-grating

More data supporting this explanation is shown in Fig. 4.3. In Fig. 4.3a we show for a mixed Fe/Au-grating (periodicity $p = 1$), as a function of B_{ext} , that the change $\Delta\nu$ in precession frequency (compared with a pure Au-grating) can become negative, if large positive V_g are applied to the Fe bars. Data similar to Fig. 4.2b ($p = 1$) is shown in Fig. 4.3b, but this time for a $p = 2$ -grating. Also here, on the mixed Fe/Au-grating (solid line), ν decreases with a positive V_g applied to the Fe bars.

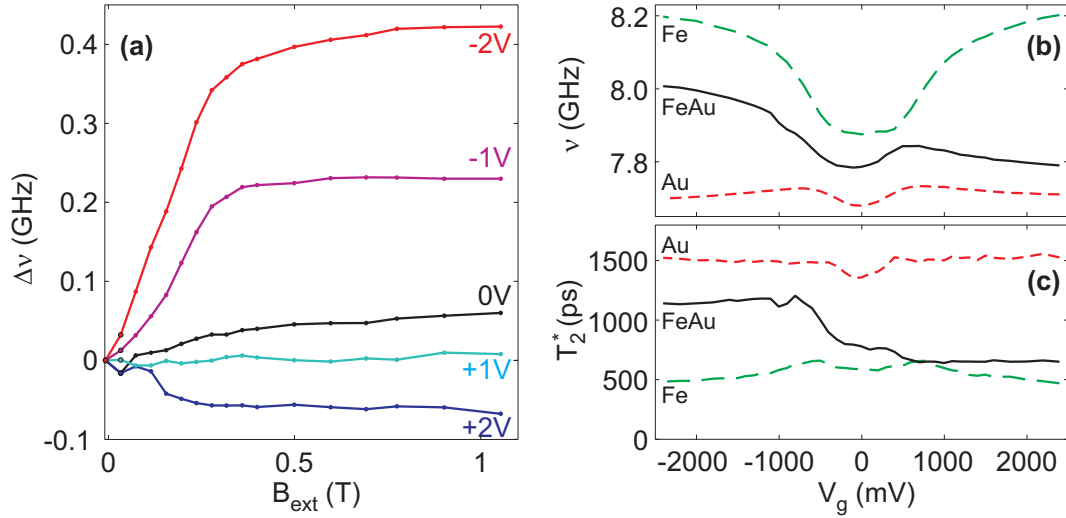


Figure 4.3: (a) $\Delta\nu$ as a function of B_{ext} for different V_g applied to a mixed Fe/Au-grating. $+V_g$ was applied to the Fe bars, $-V_g$ to the Au bars (grating periodicity $p = 1$). (b,c) ν and T_2^* for a Fe-grating, a Au-grating and a mixed Fe/Au-grating (all $p = 2$).

However, ν does not fall below ν on the Au-grating (dashed red line), since the sampling of ‘negative’ stray fields is less pronounced for $p = 2$ compared to $p = 1$. The spin coherence time T_2^* as a function of V_g is shown in Fig. 4.2c. For a pure Fe or Au grating, T_2^* is symmetric with respect to $V_g = 0$ (dashed lines). For a mixed Fe/Au-grating, however, a negative V_g applied to the Fe bars increases T_2^* , while a positive V_g on the Fe bars reduces T_2^* . In the latter case, the inhomogeneity of the stray field is raised, since both positive and negative stray fields are probed. For negative V_g applied to the Fe bars, only positive stray fields are probed, resulting in a more homogeneous stray field and an increased T_2^* , as previously mentioned in Sect. 3.4.3 and in Fig. 3.7.

Tunability for low $|V_g| < V_g^{\text{on}}$

We return again to the pure Fe and Au-gratings and the data shown in Fig. 4.2. The increase in ν (Fig. 4.2a) is not linear in V_g . The sensitivity $\partial\nu/\partial V_g$ of ν to changes in V_g for the $p = 1 \mu\text{m}$ grating is plotted in Fig. 4.2c. For $V_g < V_g^{\text{on}} \approx 500 \text{ mV}$ the increase is small and very similar for both the Fe and the Au (as well as the mixed Fe/Au) grating. We suspect that in this regime, ν changes because of a variation of the electron g -factor by about 0.001. Possible explanations for such an electric-field-induced modification of spin dynamics include changes in the overlap between electron and hole wavefunctions [87], band-structure effects [88, 89], and strain-induced spin-orbit effects [45].

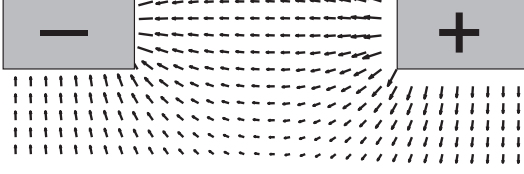


Figure 4.4: Electric field between a positively and a negatively charged bar.

Tunability for high $|V_g| > V_g^{\text{on}}$

For $|V_g| > V_g^{\text{on}}$, ν increases strongly on the $1 \mu\text{m}$ Fe sample, whereas it remains constant on the $1 \mu\text{m}$ Au sample. The tunability is highest around $V_g \approx 800 \text{ mV}$, where a change of 1 V in V_g leads to a variation of about 0.5 GHz in ν , corresponding to an effective stray field of $\approx 70 \text{ mT}$.

Dependence of V_g^{on} on geometry

The on-set voltage V_g^{on} is smaller for larger p . An analysis of the electric field between and below the bars can explain this dependence on V_g . As mentioned above, the relevant mechanism that increases ν is the depletion of the QW below the negatively charged gate. In the center below a bar, far away from an edge, vertical electric fields dominate. With a capacitor model we estimate the potential drop between gate and QW needed to deplete the QW to be roughly 100 mV , which is lower than V_g^{on} . For voltages which are more negative than required for the depletion of the electron gas, lateral electric fields between the bars become important, c.f. Fig. 4.4, similar to the situation in quantum point contacts [90]. Close to the edge of a bar, where the magnetic stray fields are highest, lateral electric fields dominate. Under illumination ($P = 500 \mu\text{W}$) at $V_g = 1 \text{ V}$, a considerable current of approx. $1 \mu\text{A}$ is measured through a gated grating, yielding an estimated resistance of $2 \text{ M}\Omega$. This resistance can be seen as a series of three resistances: a forward-biased Schottky barrier R_s^f from one bar to the QW, the resistance R_{QW} of the QW itself, and a reverse-biased Schottky barrier R_s^r from the QW to the other bar. The period $p = d_{\text{gate}} + d_{\text{gap}}$ is the sum of the gate and the gap width. The (lateral) electric field in the QW is

$$E_{\text{QW}} = \frac{V_{\text{QW}}}{d_{\text{gap}}} = \frac{R_{\text{QW}}}{d_{\text{gap}}} \frac{2V_g}{R_s^f + R_s^b + R_{\text{QW}}} \quad (4.1)$$

$$\approx \frac{V_g}{d_{\text{gap}}} \frac{R_{\text{QW}}}{R_s^f + R_s^b},$$

where we have assumed $R_s^b \gg R_{\text{QW}}$. Enlarging the channel length d_{gap} increases its resistance, i.e. $R_{\text{QW}} \propto d_{\text{gap}}$, whereas enlarging d_{gate} reduces the resistance of the Schottky contact, as the area between gate and the sample surface is increased, thus $R_s^{f,b} \propto 1/d_{\text{gate}}$. As a consequence, $E_{\text{QW}} \propto d_{\text{gate}} V_g$.

We assume that a critical (lateral) field $E_{\text{QW}}^{\text{on}}$ is needed to significantly shift the

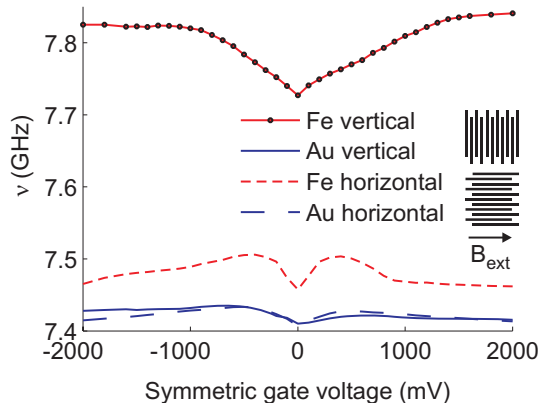


Figure 4.5: Magnetic stray field effect on the electron precession frequency ν of an interdigitated 2-2 grating as a function of gate voltage applied for parallel (‘horizontal’) and perpendicular (‘vertical’) orientation of the external magnetic field $B_{\text{ext}} = 1.04$ T to the bars’ easy axis. The data points measured are indicated on the ‘Fe vertical’ curve.

depletion edge of the electron gas close to the bar edge and to move the electrons towards the positively charged bar. Then, for larger d_{gate} the onset voltage decreases:

$$V_g^{\text{on}} \propto E_{\text{QW}}^{\text{on}}/d_{\text{gate}} \quad (4.2)$$

This qualitatively explains the dependence of V_g^{on} on the grating geometry. In addition, we experimentally tested relation (4.2) by fabricating gratings with $d_{\text{gap}} = a d_{\text{gate}}$, $a = 1, 2$, and 3 . Changing d_{gap} did not significantly alter V_g^{on} , whereas a larger d_{gate} reduced V_g^{on} substantially. Further support for Eq. (4.2) was found in time-resolved photoluminescence measurements (see appendix A).

4.1.4 Horizontal and vertical gratings

Instead of comparing the V_g -dependence on a Fe with an Au-grating, we can compare $\nu(V_g)$ on a vertical grating (easy axis of the bars perpendicular to B_{ext}) with ν on a horizontal grating (easy axis parallel to B_{ext}), similar to the experiments presented in Sect. 3.4.7 for sweeps of B_{ext} .

Figure 4.5 shows a plot similar to Fig. 3.15, but this time at a constant field B_{ext} and for a varying gate voltage V_g . Again, the change in ν is largest for the vertical Fe grating. For both Au gratings, ν changes as already shown in Fig. 4.2a, and there is no relevant difference between horizontal and vertical grating orientation. For the Fe grating, the vertical orientation shows what has already been presented in Fig. 4.2a. The horizontal orientation exhibits also a small change of ν with V_g . We attribute this to edge roughness of the Fe that locally induces small magnetic stray fields. With a varying V_g , those stray fields are probed differently.

4.1.5 Spatially resolved measurements on gated gratings

To verify the mechanism that leads to the observed dependence of ν on V_g below a Fe grating (Sect. 4.1.3), we performed spatially resolved measurements with the 3-

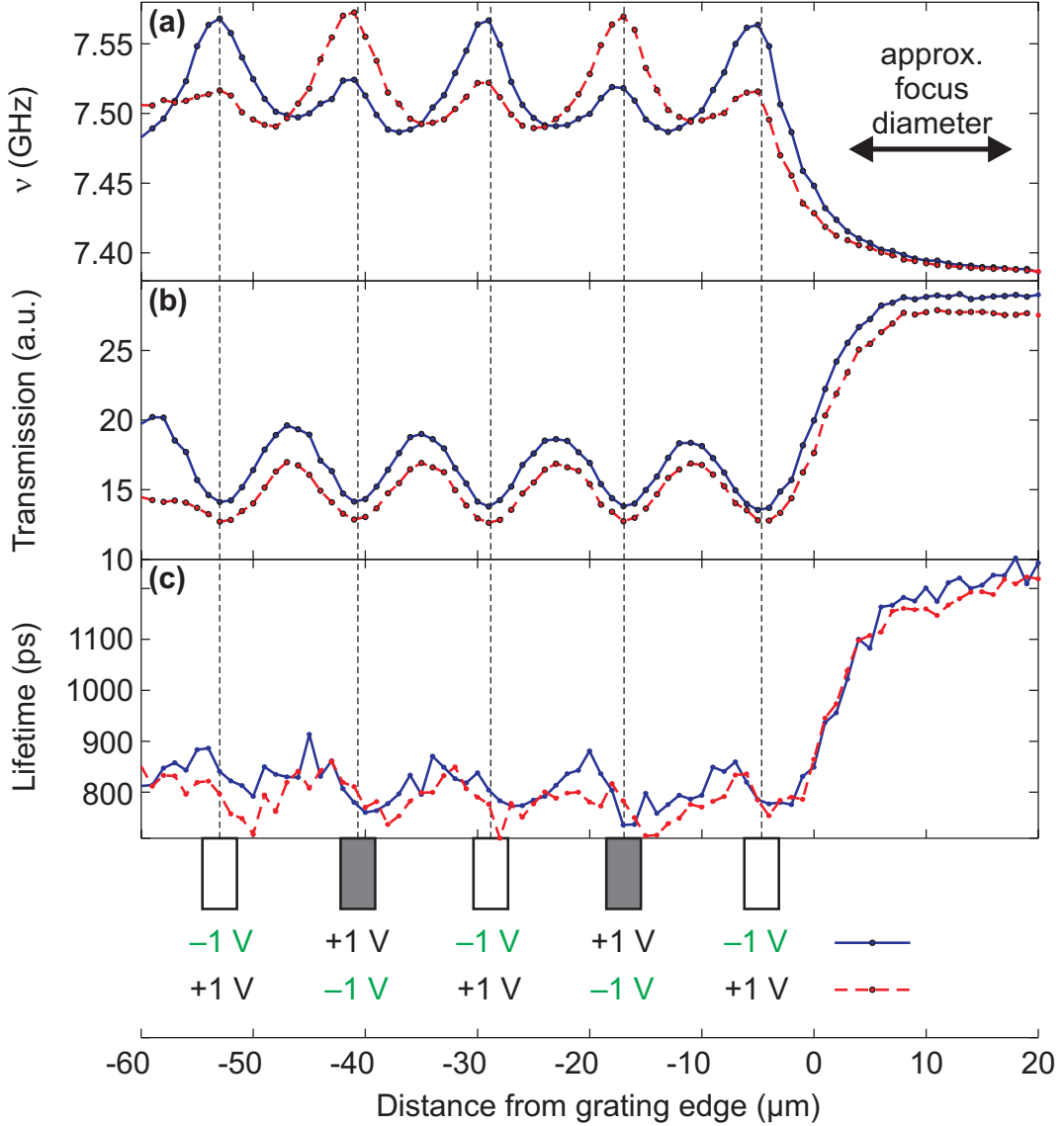


Figure 4.6: Scan along the x -axis over a 3-9-grating. (a) Spin precession frequency ν as a function of x . In the vicinity of a bar, the stray field is enhanced. If the bar is negatively charged, this enhancement is higher than if the bar is positively charged. (b) Transmission through the grating. Minima in the transmission indicate that the laser is centered on a bar. (c) Spin coherence time T_2^* . Below a positively charged bar, the lifetime is (slightly) shorter than below a negatively charged bar.

9-grating already introduced in Sect. 3.4.6. This grating has a period of $p = 12 \mu\text{m}$, comparable to the laser focus diameter of $d \approx 15 \mu\text{m}$. When the laser is centered on a bar, we can expect ν to be dominated by the stray field induced by this bar, since, on both sides, the next bar is $9 \mu\text{m}$ away. In Fig. 4.6a we present a scan along the x -axis over this grating, centered in z -direction. We show two traces, one with a gate voltage of $V_g = +1 \text{ V}$, the other with $V_g = -1 \text{ V}$. For the measurements with pure Fe or Au gratings presented in Sect. 4.1.3 it was unimportant if the odd bars were gated with $+1 \text{ V}$ and the even bars with -1 V , or vice versa. Because $d \gg p$, we averaged over both odd and even bars and the sign did not matter, as illustrated in the symmetric curves with respect to $V_g = 0$ in Fig. 4.2a.

In the experiment shown here, however, it does matter if the laser focus is centered on a bar that is put on a positive or on a negative potential. In Fig. 4.6b, the minima in transmission indicate that the laser focus is centered on a bar, labeled by the vertical dashed lines. In the lowest part of the figure, a sketch of the bars with the voltages applied is shown for the two traces. In Fig. 4.6a, ν is shown as a function of x . If the laser is centered on a positively charged bar ($V_g > 0$), then ν increases slightly compared with ν in the middle of a gap. If the laser focus is centered on a negatively charged bar ($V_g < 0$), ν increases considerably more than in the case $V_g > 0$.

This is consistent with the argument given in Sect. 4.1.3: below a negatively charged bar, the QW is depleted and a smaller or even no region with negative stray field is probed, thus the increase in ν due to the stray field is larger than if the laser is centered on a positively charged bar, where the probing of negative stray fields below a bar reduces the increase in ν considerably. Note that the stray field in both cases ($V_g \gtrless 0$) is still positive. Only in the mixed Fe/Au-gratings with $0.5 \mu\text{m}$ wide bars, diffraction and surface plasmonic effects were sufficiently strong to result in a negative average stray field for positive V_g applied to a Fe bar (if at the same time, no negatively charged Fe bars were probed, as in the mixed Fe/Au-grating).

From the spin coherence time T_2^* (Fig. 4.6c), conclusions about the inhomogeneity of the magnetic field perceived by the probed electron ensemble can be drawn: an inhomogeneous field results in a decreased spin coherence time. Beside the grating, the electrons feel the homogeneous $B_{\text{ext}} = 1.05 \text{ T}$ and $T_2^* \approx 1200 \text{ ps}$. On the grating, due to the stray field, T_2^* is reduced to $\approx 800 \text{ ps}$. Below a positively charged bar, the inhomogeneity is larger, since both positive and negative stray fields are probed. This manifests in T_2^* : if the laser is centered on a bar, T_2^* is slightly lower if this bar is positively gated ($V_g = +1 \text{ V}$) than if it is negatively charged.

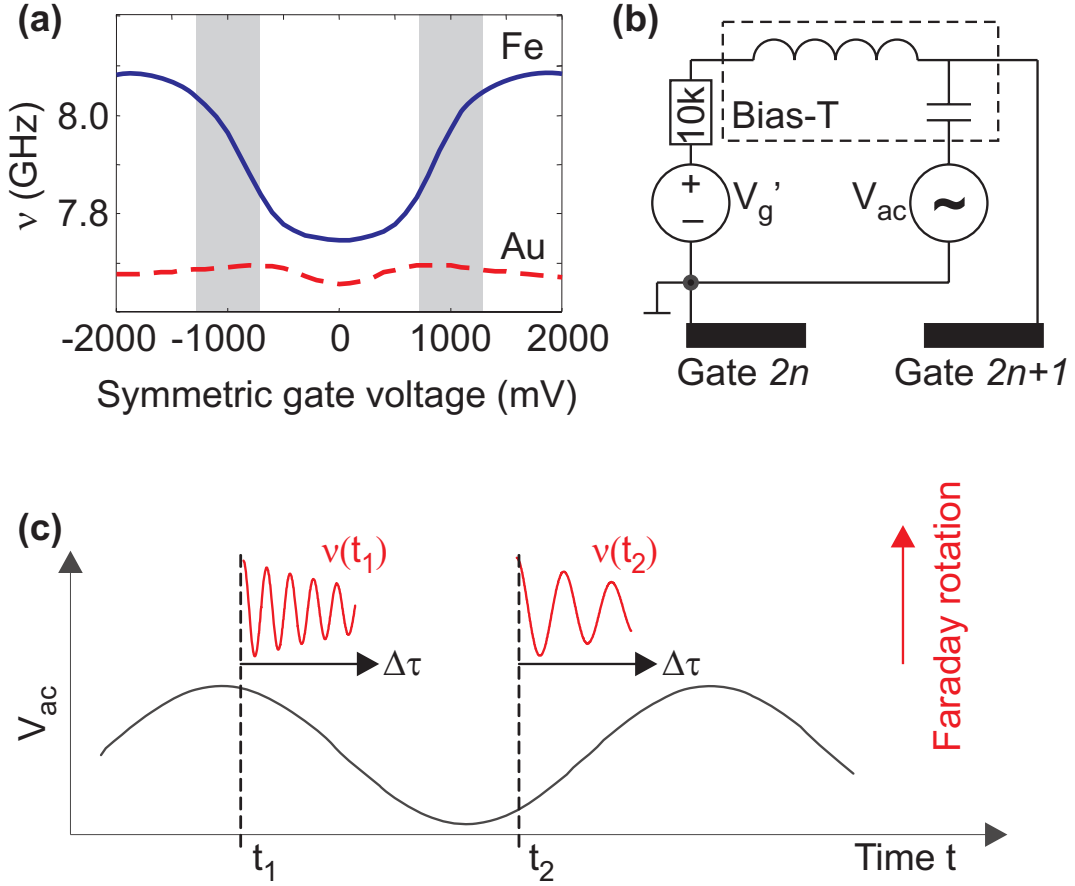


Figure 4.7: (a) The gate-controlled modification of ν below a Fe grating is most efficient around a symmetric gate voltage of $V_g = 1$ V (corresponding to $V_g' = 2$ V). (b) Set-up for the measurements with oscillating gate voltages. A d.c. voltage V_g' and an a.c. voltage V_{ac} are added using a bias-T. (c) The electron precession frequency ν is measured at different times t_i of the a.c. oscillating voltage. For this, the phase shift between the laser pulse and the a.c. voltage is controlled electronically. As long as the a.c. frequency f is slow compared to ν , a well defined $\nu(t_i)$ can be obtained.

4.2 Oscillating gate voltages

4.2.1 Introduction and electronic set-up

We now apply oscillating voltages to the interdigitated grating consisting of $0.5 \mu\text{m}$ wide Fe stripes separated by $0.5 \mu\text{m}$ wide gaps, as described in the previous Sect. 4.1. By modulating V_g on gigahertz frequencies, we expect the electrons to spatially move within the inhomogeneous stray field and to precess about a magnetic field that changes on a time scale of nanoseconds.

In Fig. 4.7a, we show again the $\nu(V_g)$ dependence for the $p = 1$ -grating. For a

symmetric gate voltage V_g of around 1 V, the tunability of ν is highest. With a d.c. voltage, we can choose this as a working point and add an oscillating voltage $V_{\text{a.c.}}$ with an amplitude of around 0.5 V. We expect then to see different ν , depending on whether we probe the electron spins at a time where $V_{\text{a.c.}}$ is maximal or minimal.

The set-up for these measurements is shown in Fig. 4.7b. In contrast to the experiments presented in Sect. 4.1, we use only one d.c. voltage source, i.e. the bars are not gated symmetrically with respect to the grounded substrate anymore. Therefore, we denote the gate voltages in this section by V'_g (instead of V_g for the symmetric case, c.f. Fig. 4.1b) and note that for the potential difference between two neighboring bars, $V'_g = 2V_g$. The d.c. voltage V'_g is added to a sinusoidally oscillating a.c. voltage $V_{\text{a.c.}}(t) = V_{\text{a.c.}}^0 \sin(2\pi ft)$ using a bias-T. An r.f. power of 10 dBm was used, theoretically corresponding to a V_{AC}^0 of about 0.7 V at low f . With this configuration, including the cables in the cryostat, we are capable of applying frequencies f up to a few GHz, as experimentally verified using an oscilloscope. However, since our gratings have capacitances on the order of 5 pF, the a.c. amplitude arriving at the gates is damped already for $f > 500$ MHz. The gates have a high impedance, and are not terminated by a 50Ω resistance. This leads to reflections, which are mostly absorbed by the 50Ω part of the system (bias-T and a.c. voltage source). A measurement of the oscillating voltage on the gates with a high-impedance probe did show nice sinusoidal oscillations with no signs of reflections. The amplitude of the voltage at $f = 480$ MHz is reduced by ≈ 4 dBm by the bias-T, cables and connectors. This seems little, but taking into account that an effectively doubled amplitude would be expected since the gates are not terminated by 50Ω , an effective reduction of ≈ 10 dBm is measured.

Figure 4.7c illustrates the principle of our measurement: by scanning the phase difference between the laser pump pulse and the a.c. modulation, we are able to track the electron spin precession at different phases of the a.c. modulation. We call this time difference the ‘laser-gate delay t ’. It is known up to a constant t_0 , which is unchanged throughout an experiment, as long as f is not changed (in which case the function generator changes its relative phase). This is a consequence of the fact that we do not know when exactly our laser pulse reaches the sample, but we can precisely (with a precision of less than 10 ps) change this delay t .

At different laser-gate delays t , we perform TRFR sweeps and extract a spin precession frequency $\nu(t)$. To determine ν with ample precision, about 3 spin oscillations are required. In a total magnetic field of ≈ 1 T, one spin precession takes the time of 125 ps, we therefore need ≈ 400 ps for the determination of ν . As long as f is slow compared to this, $\nu(t)$ is well defined. Otherwise, the effects of $V_{\text{a.c.}}(t)$ will start to average out and for $f \approx \nu/3 \approx 3$ GHz, we expect $\nu(t)$ to be constant in t .

4.2.2 Electron precession frequency as a function of laser-gate delay

In Fig. 4.8a we present results with a modulated gate voltage on the $p = 1 \mu\text{m}$ grating for four modulation frequencies of 160, 480, 960 and 1440 MHz and $V_g' = 2 \text{ V}$. $\nu(t)$ oscillates with the exciting frequency f and an oscillation amplitude ν_1 of between 0.02 and 0.5 GHz. (Note that the phase of the a.c. modulation has changed between measurements on Fe and Au gratings and the four frequencies due to the a.c. function generator.) This oscillation is explained by assuming that the electrons in the QW follow the a.c. modulation. When t is such that the laser pulse coincides with a minimum in $V_{\text{a.c.}}$, then the voltage below the even bars is minimal when we measure the electron spin precession. Consequently, the electrons are depleted in the QW below and, as found for the d.c. case, ν is maximal. A similar argument explains the minima in ν .

However, this oscillation is observed not only on the Fe grating, where it is expected following our expectations above. Also on the Au grating, a (weaker) oscillation is visible. From the knowledge of $\nu(V_g)$ (Fig. 4.7a), we can estimate the magnitude of ν_1 to be

$$\nu_1 = \frac{1}{2} \left. \frac{\partial \nu}{\partial V_g} \right|_{V_g'} V_{\text{a.c.}}^0. \quad (4.3)$$

Since below a Au grating, $\partial \nu / \partial V_g' \approx 0$, no oscillation is expected, contrary to the measurement. As we will show in the next chapter 5, the oscillations below the Au gratings are due to effects of spin-orbit-interaction, where the electrons feel a magnetic field due to their motion induced by the a.c. electric field.

Here, we take this effect as a background acting on electrons below both Au and Fe gratings. The linear fit in Fig. 4.8b matches the Au data points well. The additional effect below the Fe grating due to the influence of the stray field is described by Eq. (4.3) and added to the linearly fitted background on the Au grating. We further take into account the damping of our circuit at higher frequencies measured with a high-impedance probe to obtain a corrected value for $V_{\text{a.c.}}$. With this, we obtain the dashed ‘expectation Fe’ line, which matches the measured data points quite well.

4.2.3 Dependence on d.c. gate voltage

The dependence on the d.c. gate voltage V_g' is also estimated by Eq. (4.3). At $V_g' = 0$, the derivative of ν with respect to V_g vanishes and no oscillation amplitude ν_1 is expected. For an inverted V_g' , we also expect an inverted oscillation, i.e. a phase shift by π , since the sign of the derivative changes. Such a measurement is shown in the left panel of Fig. 4.9 for $f = 960 \text{ MHz}$. Again, smaller oscillations are detected on the Au grating but are not discussed in detail here.

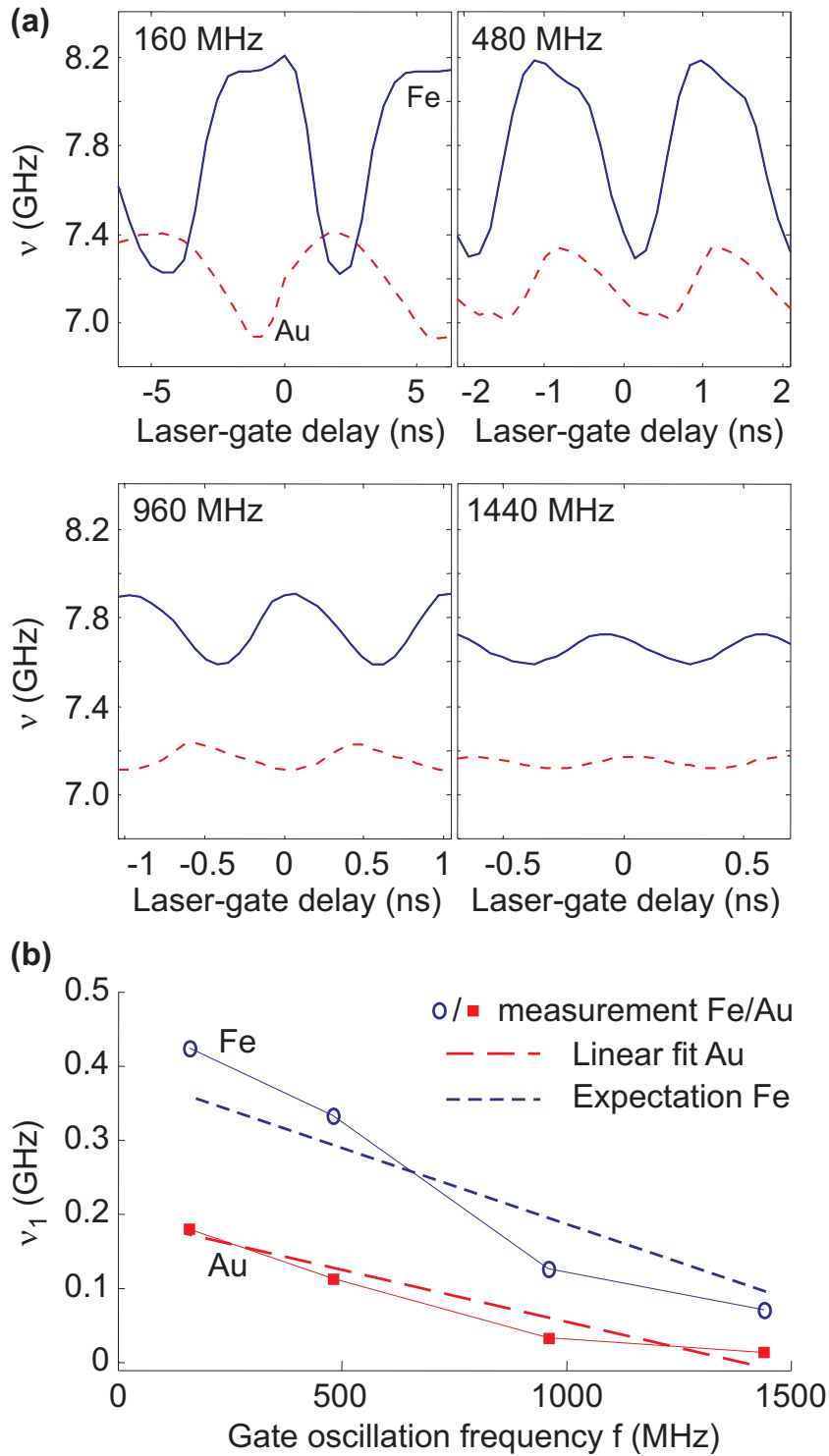


Figure 4.8: (a) Electron precession frequency ν below $p = 1$ Fe and Au gratings as a function of the phase shift between laser pulse and a.c. voltage phase for different gate oscillation frequencies f . A d.c. voltage $V'_g = 2$ V was added to the a.c. modulation. (b) Amplitude ν_1 of the oscillations in ν as a function of f . The phase of each measurement is arbitrary.

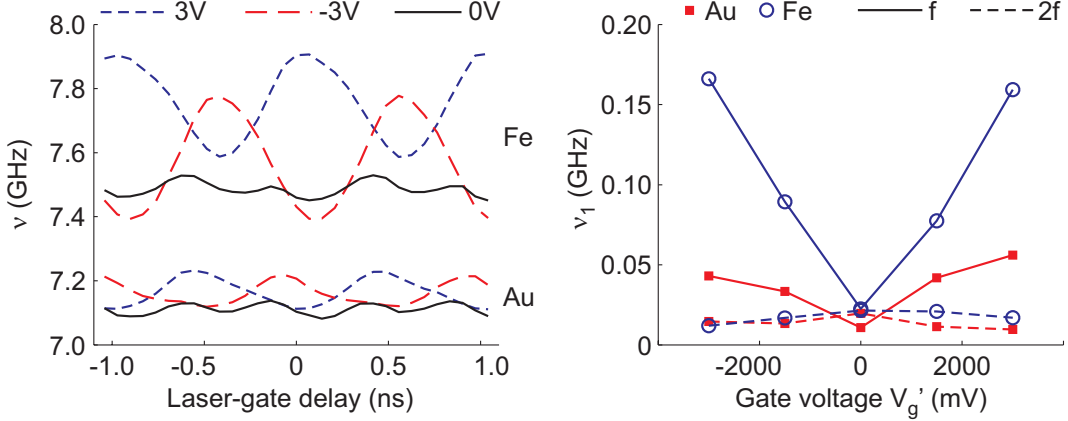


Figure 4.9: Left: The oscillations in ν as a function of laser-gate delay are modified when adding a d.c. gate voltage $V'_g = -3, +3$ and 0 V. Right: f - (solid line) and $2f$ -component (dashed lines) of the ν -oscillations as a function of V'_g . Data for the $p = 1$ Fe and Au gratings, a r.f. power of 10 dBm and $f = 960$ MHz. Again, the phase has changed between the measurement of the Fe and the Au gratings due to the a.c. function generator.

The traces for $V'_g = \pm 3$ V are shifted by π as expected. At $V'_g = 0$, the oscillations below the Fe grating are strongly reduced compared to $|V'_g| > 0$. Instead, oscillations with the double frequency $2f$ become visible. Such an effect can be explained when considering gate oscillations around $V'_g = 0$ in the $\nu(V'_g)$ -dependence in Fig. 4.7a. ν increases for both negative and positive gate voltages compared to $\nu(V'_g = 0)$, therefore an enhanced $\nu(t)$ is expected twice per a.c. period, resulting in $2f$ -oscillations.

Such $2f$ -oscillations are also anticipated for the spin-orbit-induced magnetic field (chapter 5), if this field is oriented perpendicularly to B_{ext} . In fact, this effect seems to dominate the $V'_g = 0$ trace, since the oscillations on both Fe and Au grating are of similar amplitude.

A plot of the amplitudes of both the f and $2f$ -components of the oscillations in $\nu(t)$ is shown in the right panel of Fig. 4.9 for $V'_g = \pm 3, \pm 1.5$ and 0 V (corresponding to $V_g = \pm 1.5, \pm 0.75$ and 0 V). The $2f$ -components (dashed lines) are similar below Fe and Au gratings and do not significantly change with V'_g , supporting that they both originate from spin-orbit effects. The f -component of the oscillation below the Fe grating increases since also $|\partial\nu/\partial V'_g(V'_g)|$ increases with V'_g in Eq. (4.3).

The fact that also the spin-orbit induced f -component below the Au grating increases with V'_g could be explained as follows: a higher V'_g leads to higher currents that flow through the Schottky-contacts between the gates and the QW. Since the I/V-characteristics of a Schottky-contact is highly non-linear, the additional electric field due to $V_{\text{a.c.}}$ leads to an additional current that is larger than just the ratio of $(V'_g + V_{\text{a.c.}})/V'_g$. Therefore, $V_{\text{a.c.}}(t)$ leads to a faster electron movement when

superimposed on a d.c. voltage V'_g and therefore to larger spin-orbit magnetic fields.

4.2.4 A.c. effects beside a grating

Figure 4.10b shows the oscillation amplitude ν_1 on a two-dimensional scan over four gratings, whereof the two gratings to the right ($p = 1$ Fe and Au) were applied $V'_g = 3$ V and an a.c. voltage at $f = 480$ MHz with a r.f. power of 10 dBm. A microscope image of the region scanned is shown in Fig. 4.10a.

Clearly, the effect of the a.c. gate modulation is not restricted to the grating itself. Although ν_1 is largest on the $p = 1$ Fe grating, even beside the excited gratings an oscillating behavior of $\nu(t)$ is measured. It spreads mainly in x -direction and decays on a length scale of a few $100 \mu\text{m}$ as visible from the cut at $z = 0$ in Fig. 4.10c.

Beside a grating, the magnetic stray fields are negligible and therefore, the oscillation in $\nu(t)$ cannot be explained by the effects of magnetic stray fields. Furthermore, these oscillations vanish when reducing the r.f. power. They are, again, explained by magnetic fields induced by spin-orbit coupling. Close to an excited grating, due to the grating itself as well as due to the wiring on the sample, oscillating electric fields exist in the plane of the QW. These fields lead to an oscillatory motion of the electrons and induce a spin-orbit magnetic field. The investigation of this field will be the subject of the following chapter 5.

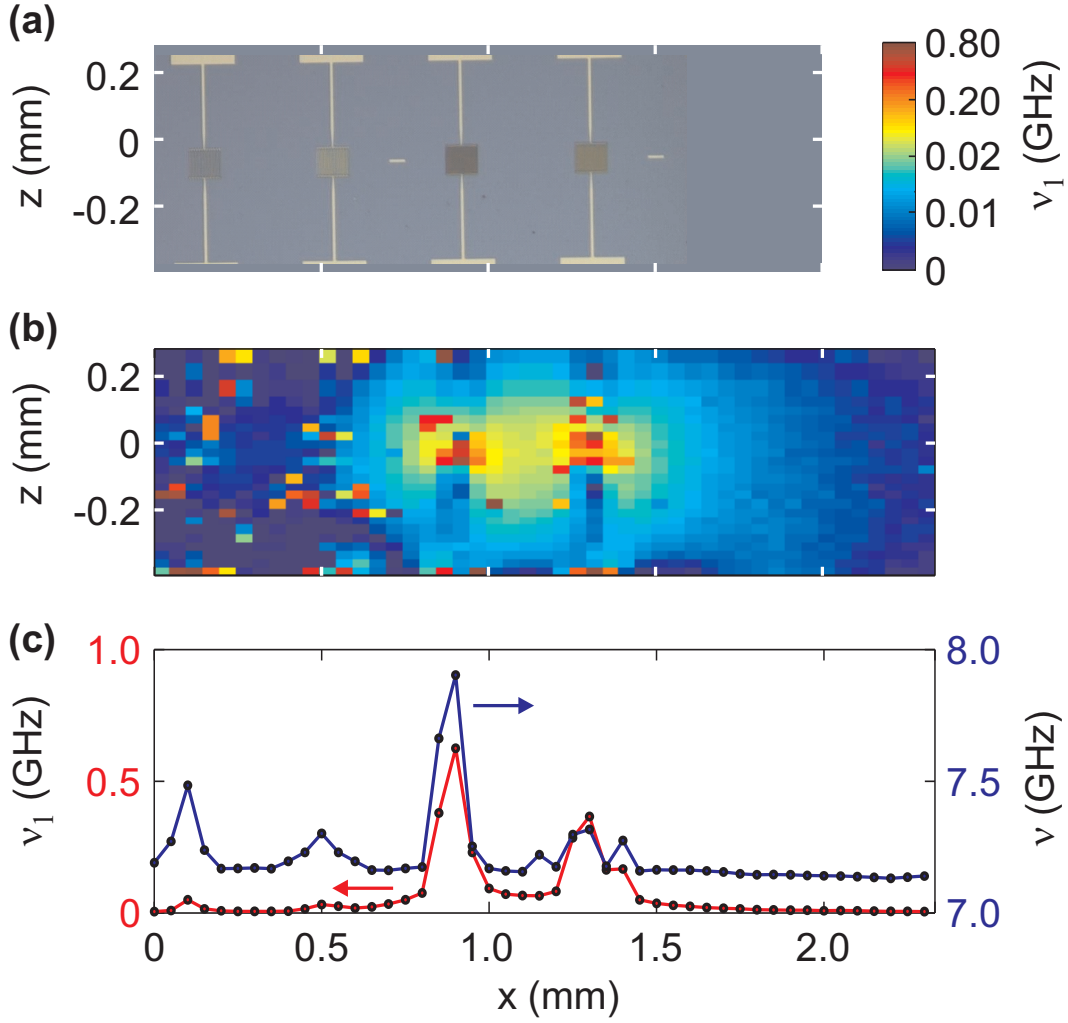


Figure 4.10: (a) Microscope image of the scanned region. The two gratings to the left are $p = 2$ Fe and Au. The two gratings to the right ($p = 1$, Fe and Au) are excited with an a.c. gate voltage. (b) Oscillation amplitude ν_1 on and beside the gratings. Imperfections are due to dirt on the sample. (c) ν_1 (left scale) and the average electron precession frequency ν (right scale) as a function of the lateral position x at $z = 0$.

Chapter 5

Spin manipulation with electric fields

In this chapter, after an introduction into spin-orbit interaction (Sect. 5.1), we report on a new method enabling the direct measurement of both Rashba and Dresselhaus spin-orbit fields by probing the electron spin precession frequency as a function of the direction of the electron motion with respect to the crystal lattice (Sect. 5.2). We then show, in Sect. 5.3, how the spin-orbit interaction spatially depends on the local orientation of an exciting electric field. In Sect. 5.4, we show that the spin-orbit fields can be used to trigger spin resonance, also referred to as electric-dipole-induced spin resonance.¹

5.1 Introduction to spin-orbit interaction

Not only magnetic fields can serve as a tool to manipulate electron spins, also electric fields couple to the spin, via the spin-orbit (SO) interaction. This is a relativistic effect, where electric fields in the moving frame of an electron appear as magnetic fields (c.f. the Lorentz-transformation, Eq. 1.9).

Symmetry-breaking electric fields in semiconductors and externally applied gate voltages induce a spin splitting, because electric fields appear to a moving electron as magnetic fields, which interact with the electron spin and couple it with the electron momentum, or wave vector, \mathbf{k} . In zinc-blende-type crystals, such as GaAs, the electric fields resulting from the lack of an inversion center lead to bulk inversion asymmetry (BIA) and to the Dresselhaus term in the Hamiltonian [51]. In the conduction band, its coupling is linear or cubic in k with proportionality constants β and γ , respectively. In heterostructures, additional electric fields are introduced owing to structure inversion asymmetry (SIA), giving rise to the Rashba term [53], which for conduction-band electrons is linear in k with coupling constant α . Both

¹Parts of this chapter have been published in L. Meier *et al.*, Nature Physics (2007).

contributions have been extensively studied [91], since a potential use of electron spins in future devices (e.g. a spin transistor [47]) requires precise control of the spin's environment and of the Dresselhaus and Rashba fields [54]. Spin-orbit fields also contribute to spin decoherence [41], see Sect. 1.4.2.

In two-dimensional systems, such as quantum wells (QWs), usually $\alpha \gg \beta$ and $\gamma \approx 0$ [92–95]. Therefore, measurements of the spin-orbit coupling initially focused on the Rashba term in QWs and concentrated on the study of beatings in Shubnikov–de-Haas oscillations [93, 95–98], whose interpretation, however, is debated [99, 100]. More recent experiments include the investigation of antilocalization in magnetotransport [101] or the analysis of photocurrents [102]. In the latter experiment, the ratio α/β could be determined. A gate-induced transition from weak localization to antilocalization allowed the discrimination between Rashba, as well as linear and cubic Dresselhaus contributions to the spin-orbit field [103]. Tuning of the Rashba coupling has been achieved by introducing additional electric fields from gates [94, 104] or by changing the electron density [105, 106].

The influence of effective spin-orbit magnetic fields on optical measurements in a heterostructure was already measured in 1990 [107], and the spin-orbit-induced precession of spin packets was observed more than a decade later [71, 108]. Remarkably, the in-plane spin-orbit fields in a QW can lead to an out-of-plane spin polarization [109]. In ref. [110], it was pointed out that although spin-orbit and external magnetic fields can be added to describe spin precession [107], a more complicated concept has to be evoked when accounting for the generation of an out-of-plane spin polarization.

5.1.1 Rashba spin-orbit term (SIA)

The Rashba spin-orbit coupling term originates from electric fields induced by interfaces in heterostructures or from electric fields from charged gates. For a QW, these fields are always perpendicular to the QW plane, and since the electron motion \mathbf{v} is confined to the QW plane, it already follows from Eq. (1.9) that the resulting magnetic field is in-plane of the QW and perpendicular to \mathbf{v} , its magnitude proportional to v . Indeed, the Rashba spin splitting is linear in the electron wave vector $\mathbf{k} \propto \mathbf{v}$ [91, 111],

$$H_{\text{SIA}} = \alpha(\sigma_x k_y - \sigma_y k_x), \quad (5.1)$$

independent of the (orthogonal) coordinate system. The proportionality constant α is called the Rashba coefficient. In a heterojunction, it is given by [91, 112]

$$\alpha \propto \frac{\Delta_0}{E_g^3} \nabla V, \quad (5.2)$$

where E_g and Δ_0 are band gap and spin-orbit splitting (see Fig. 1.1), respectively, and $\mathcal{E} = -\nabla V$ is the electric field induced by the interface. It can be tuned over

one to two orders of magnitude by choosing materials with appropriate E_g and Δ_0 and by engineering ∇V in a heterostructure.

For the following discussion, we denote the electric field in the conduction (valence) band by \mathcal{E}^c (\mathcal{E}^v), and the expectation value for a wave function in the conduction or the valence band by $\langle \rangle_c$ or $\langle \rangle_v$, respectively.

It has been argued that the expectation value of the electric field $\langle \mathcal{E}^c \rangle_c$ for a wave function in the conduction band of a QW vanishes, since, according to Ehrenfest's theorem, no force acts on a bound state. The electron wave function rearranges in z -direction such that $\langle \mathcal{E}_z^c \rangle_c$ vanishes. In this case, no Rashba spin-orbit coupling would be expected. It has, however, been shown [113] that the spin-orbit coupling of *conduction-band* electrons is determined by the expectation value of the electric field in the *valence band* for the *conduction-band* wave function $\langle \mathcal{E}_z^v \rangle_c$ (and vice-versa for holes the electric field in the conduction band $\langle \mathcal{E}_z^c \rangle_v$) [91]. The expectation value of $\langle \mathcal{E}_z^v \rangle_c$ can well be nonzero even if $\langle \mathcal{E}_z^c \rangle_c$ vanishes, as illustrated later in appendix C by Fig. C.3.

5.1.2 Dresselhaus spin-orbit term (BIA)

Dresselhaus term in bulk systems

The spin-orbit effect described by the Dresselhaus term originates from the lack of an inversion center in zinc-blende-type semiconductors, like in GaAs. Following [24], this results in the appearance of terms cubic in the electron wave vector \mathbf{k} in the Hamiltonian of conduction-band electrons

$$H = \frac{\hbar^2 k^2}{2m} + \frac{\hbar}{2} \boldsymbol{\sigma} \cdot \boldsymbol{\Omega}(\mathbf{k}), \quad (5.3)$$

where $\boldsymbol{\sigma}$ is a vector of Pauli matrices and $\boldsymbol{\Omega}(\mathbf{k})$ is defined by

$$\Omega_x(k) = \chi \hbar^2 \left(m \sqrt{2mE_g} \right)^{-1} k_x (k_y^2 - k_z^2), \quad (5.4)$$

with cyclic permutation of the indices x, y, z and the coordinate axes along [100], [010], [001].

Dresselhaus term in QWs

In the two-dimensional case of a QW, averaging over the cubic terms along the quantization axis in the case of low subband filling gives rise to terms linear in \mathbf{k} in the Hamiltonian [111],

$$H_{\text{BIA}} = \beta (\sigma_x k_y + \sigma_y k_x), \quad (5.5)$$

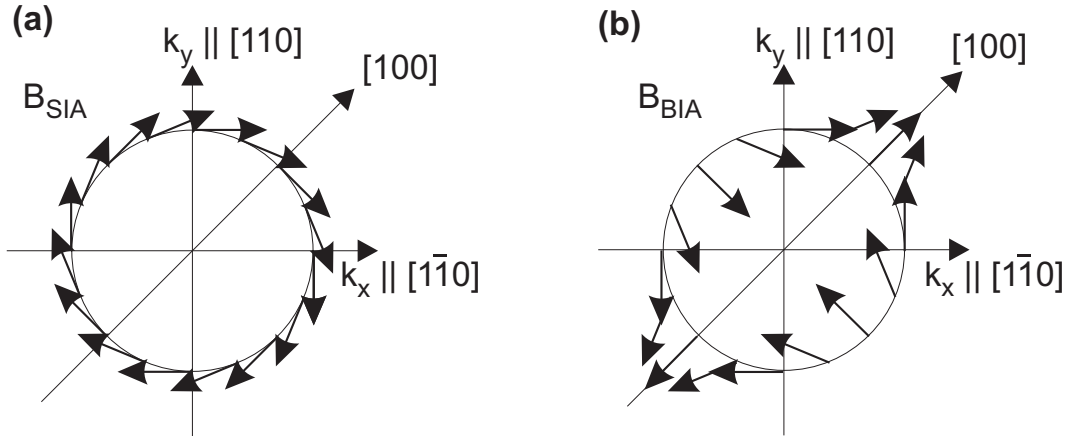


Figure 5.1: (a) Rashba and (b) Dresselhaus magnetic field for different orientations of the k -vector on a unit circle.

for coordinates along the crystal's $[1\bar{1}0]$ and $[110]$ axes². The proportionality is given by the linear Dresselhaus coefficient [103]

$$\beta \propto \gamma \langle k_z^2 \rangle, \quad (5.6)$$

where γ is the cubic Dresselhaus coefficient (see appendix B) that includes all prefactors in Eq. (5.4).

The Dresselhaus coupling is more difficult to tune, it depends not only on E_g and Δ_0 , but also on the structure of higher conduction bands [91, 112]. In a two-dimensional system, it depends on the extension of the wave function in confinement-direction, $\langle k_z^2 \rangle$. For the lowest subband in an infinitely deep potential well with width ℓ , $k_z = \pi/\ell$.

In GaAs/AlGaAs 2DEGs, even cubic Dresselhaus terms have been observed [103] on a magnitude similar to the linear terms. For our InGaAs/GaAs QWs, we did not observe cubic Dresselhaus terms, as explained later.

5.2 Measurement of Rashba and Dresselhaus fields

5.2.1 Geometrical properties of Rashba and Dresselhaus spin-orbit fields

In a two-dimensional QW, both the Rashba and Dresselhaus spin-orbit couplings are linear in the electron wave vector \mathbf{k} and can be deduced from Eq. (5.1) and (5.5)

²For coordinates along $[100]$ and $[010]$, $H_{\text{BIA}} = \beta(\sigma_x k_x - \sigma_y k_y)$.

to yield the effective magnetic fields

$$\mathbf{B}_{\text{SIA}} = \frac{\alpha}{g\mu_B} \begin{pmatrix} k_y \\ -k_x \end{pmatrix}, \quad \text{and} \quad \mathbf{B}_{\text{BIA}} = \frac{\beta}{g\mu_B} \begin{pmatrix} k_y \\ k_x \end{pmatrix}, \quad (5.7)$$

for a coordinate system with base vectors $\hat{\mathbf{x}} \parallel [1\bar{1}0]$ and $\hat{\mathbf{y}} \parallel [110]$. Here, g is the electron's g -factor and μ_B the Bohr magneton. Both fields are in-plane of the QW, but whereas \mathbf{B}_{SIA} is always perpendicular to \mathbf{k} (cf. Fig. 5.1a), \mathbf{B}_{BIA} is not (cf. Fig. 5.1b). The overall magnetic field an electron is exposed to sums up to

$$\mathbf{B}_{\text{tot}} = \mathbf{B}_{\text{ext}} + \mathbf{B}_{\text{SIA}} + \mathbf{B}_{\text{BIA}},$$

where \mathbf{B}_{ext} is an externally applied magnetic field, in-plane with the QW at an angle θ with the x -axis. As mentioned before and as we will justify later, we neglect the cubic Dresselhaus term here, its dependence on \mathbf{k} is given by Eq. (B.1) in appendix B.

5.2.2 Measurement set-up

To access B_{SIA} and B_{BIA} (or α and β), we directly measure $|\mathbf{B}_{\text{tot}}|$ by monitoring the precession of optically polarized electron spins using TRFR. We impose an effective (drift) momentum $\hbar\mathbf{k}$ on the QW electrons by applying an in-plane a.c. electric field $\mathbf{E} = \mathbf{E}_0 \sin(2\pi ft)$ at an angle φ with the x -axis, see Fig. 5.2a. Unless stated otherwise, $f = 160$ MHz. In the center of four top-gate electrodes, which enclose a square with $150 \mu\text{m}$ side length (see Fig. 5.2b), the angle φ is determined by the amplitudes E_x and E_y of two superposed fields along $\hat{\mathbf{x}}$ and $\hat{\mathbf{y}}$, $\mathbf{E}_0 = E_x\hat{\mathbf{x}} + E_y\hat{\mathbf{y}}$ (see Fig. 5.6). E_x and E_y are generated by two phase-locked oscillators, each driving two opposite electrodes. In the diffusive regime, the scattering time of the electrons in the QW is much smaller than $1/f$ and, therefore, their average drift wave vector $\mathbf{k}(t) = \hat{\mathbf{k}}k(t)$ is given by

$$k(t) = m^*\mu E(t)/\hbar = m^*\mu E_0 \sin(2\pi ft)/\hbar = k_0 \sin(2\pi ft), \quad (5.8)$$

with the unit vector $\hat{\mathbf{k}}$ pointing along the direction of \mathbf{E} ; m^* is the electron effective mass, μ the electron mobility in the QW, and \hbar Planck's constant.

Using TRFR, the electron spin precession is measured in the center of the electrodes at different times t of the electric field oscillation as already described in Sect. 4.2.1 and Fig. 4.7c. The TRFR scans are taken during a pump-probe delay interval $\Delta\tau = 0 \dots 700$ ps which is much shorter than the a.c. electric field period of $1/f = 6250$ ps. Therefore, $\mathbf{E}(t)$ is roughly constant over the spin precession observed and a well-defined precession frequency $\nu(t)$ can be obtained (c.f. Fig. 5.3a). Figure 5.3b shows TRFR oscillations at different times t . It is clearly visible that $\nu(t)$ changes periodically with t . From $\nu(t)$ we obtain $|\mathbf{B}_{\text{tot}}(t)| = h\nu(t)/g\mu_B$. Theo-

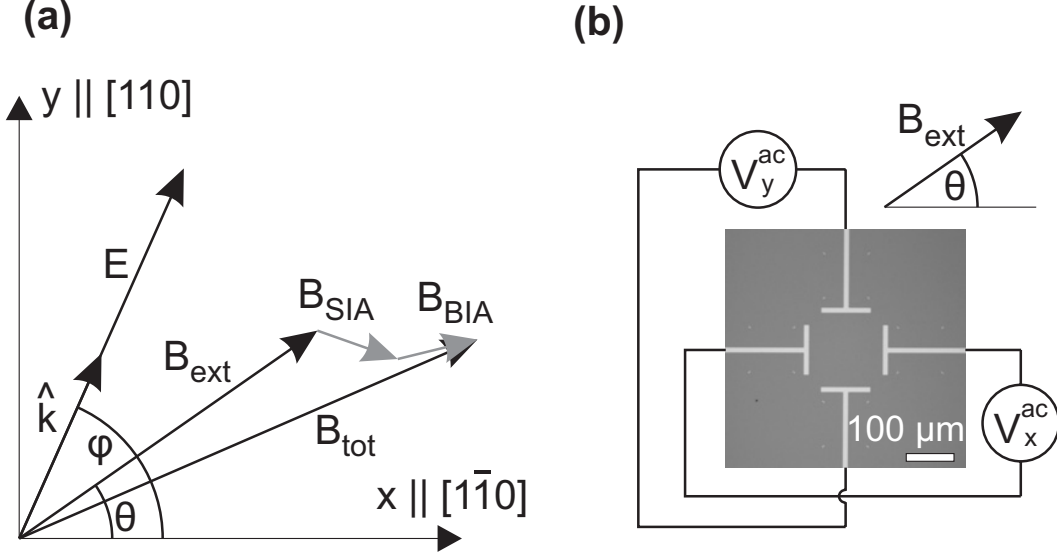


Figure 5.2: (a) Electric and magnetic fields involved in the experiment. (b) Optical microscopy image of the sample and wiring of the gates.

retically, the magnitude of $\mathbf{B}_{\text{tot}}(t)$ is obtained by the vector addition

$$\begin{aligned}
 \mathbf{B}_{\text{tot}}(t) &= \mathbf{B}_{\text{ext}} + \mathbf{B}_{\text{SIA}} + \mathbf{B}_{\text{BIA}} \\
 &= \begin{pmatrix} B_x \\ B_y \end{pmatrix} + \frac{\alpha}{g\mu_B} \begin{pmatrix} k_y(t) \\ -k_x(t) \end{pmatrix} + \frac{\beta}{g\mu_B} \begin{pmatrix} k_y(t) \\ k_x(t) \end{pmatrix} \\
 &= B_{\text{ext}} \begin{pmatrix} \cos \theta \\ \sin \theta \end{pmatrix} + \frac{k(t)}{g\mu_B} \left(\alpha \begin{pmatrix} \sin \varphi \\ -\cos \varphi \end{pmatrix} + \beta \begin{pmatrix} \sin \varphi \\ \cos \varphi \end{pmatrix} \right),
 \end{aligned} \tag{5.9}$$

where we have used Eq. (5.7) with $k_x(t) = k(t) \cos \varphi$ and $k_y(t) = k(t) \sin \varphi$. The magnitude squared of $\mathbf{B}_{\text{tot}}(t)$ is then given by

$$\begin{aligned}
 |\mathbf{B}_{\text{tot}}(t)|^2 &= |\mathbf{B}_{\text{ext}}|^2 \times (1 \\
 &\quad + \frac{2k(t)}{g\mu_B B_{\text{ext}}} ([\alpha + \beta] \cos \theta \sin \varphi + [\beta - \alpha] \sin \theta \cos \varphi) \\
 &\quad + \left(\frac{k(t)}{g\mu_B B_{\text{ext}}} \right)^2 (\alpha^2 + \beta^2 - 2\alpha\beta \cos 2\varphi)),
 \end{aligned} \tag{5.10}$$

and contains three terms that behave differently in time. A constant term, whose magnitude is given by B_{ext} , a term ‘first order’ in $k(t)/B_{\text{ext}}$ that oscillates with $k(t) \propto E(t) \propto \sin(2\pi ft)$, and a ‘second order’ term that oscillates with $k^2(t)/B_{\text{ext}}^2 \propto \sin^2(2\pi ft)$, i.e. with twice the frequency f . If we include a cubic Dresselhaus term in Eq. (5.9), additional terms proportional to $k^3(t)$, $k^4(t)$, and $k^6(t)$ appear in Eq. (5.10), see the calculation in appendix B, Eq. (B.3). These terms lead to oscillations with frequencies $3f$, $4f$, and $6f$ in $|B_{\text{tot}}|^2(t)$. Such oscillations were not

observed in the experiment, i.e. they were at least a factor 4 below the level of the ‘second order’ oscillations at $2f$ described below. We conclude that in our QWs, the cubic Dresselhaus term is negligible compared to the Rashba and linear Dresselhaus terms.

Assuming that $|B_{\text{SIA}}|, |B_{\text{BIA}}| \ll B_{\text{ext}}$, we expand the square root of Eq. (5.10) up to second order in k_0/B_{ext} , and obtain, using Eq. (5.7),

$$B_{\text{tot}}(t) \approx B_{\text{ext}} + A(\theta, \varphi) \sin(2\pi ft) + B(\theta, \varphi) \sin^2(2\pi ft), \quad (5.11)$$

with

$$\begin{aligned} A(\theta, \varphi) &= (B_{\text{BIA}} + B_{\text{SIA}}) \cos \theta \sin \varphi + (B_{\text{BIA}} - B_{\text{SIA}}) \sin \theta \cos \varphi, \quad \text{and} \\ B(\theta, \varphi) &= [(B_{\text{BIA}} + B_{\text{SIA}}) \sin \theta \sin \varphi - (B_{\text{BIA}} - B_{\text{SIA}}) \cos \theta \cos \varphi]^2 / B_{\text{ext}}. \end{aligned}$$

By measuring the oscillation amplitude of $B_{\text{tot}}(t)$ for varying angles θ and φ , we can extract the Rashba and Dresselhaus contributions to the spin-orbit magnetic field.

5.2.3 ν as a function of time

The fit of the experimental data to Eq. (5.11) with B_{ext} , $A(\theta, \varphi)$, and $B(\theta, \varphi)$ as fit parameters, matches the data points very well (Fig. 5.3d), with $B_{\text{ext}} = 0.958$ T, in agreement with Hall probe measurements of the external magnetic field. For most φ , we find $A \gg B$. The quadratic term in $k(t)$, $B(\theta, \varphi)$, which contributes to oscillations with frequency $2f$, is visible in the experiment only when rotating \mathbf{E} to an angle φ at which the k -linear term $A(\theta, \varphi)$ is weak, see Fig. 5.3e. Apart from the geometrical dependence, the amplitude of $B(\theta, \varphi)$ is suppressed by a factor $(|B_{\text{BIA}}| + |B_{\text{SIA}}|)/B_{\text{ext}} \approx 0.03$, i.e. by more than one order of magnitude compared with $A(\theta, \varphi)$. Therefore, we restrict our analysis to the linear term $A(\theta, \varphi)$.

5.2.4 ν as a function of φ and θ

We now use relation (5.11) to determine the Rashba and Dresselhaus spin-orbit fields $B_{\text{SIA}} \propto \alpha$ and $B_{\text{BIA}} \propto \beta$ by rotating \mathbf{E} and \mathbf{B}_{ext} for three GaAs/InGaAs QW samples with the substrates mentioned in the table below (c.f. Sect. 2.5). Directly from the TRFR oscillations in Fig. 5.3c we see that the electron precession frequency ν changes with the angle φ of the electric field \mathbf{E} .

For $\theta = 0$ and 90° , $A(\theta, \varphi)$ is given by $(B_{\text{SIA}} + B_{\text{BIA}}) \sin \varphi$ and $(B_{\text{BIA}} - B_{\text{SIA}}) \cos \varphi$, respectively. This dependence is observed in the experiment, as shown in Fig. 5.4a and b. The measured data points clearly follow $\sin \varphi$ for $\theta = 0$ and $\cos \varphi$ for $\theta = 90^\circ$ (solid lines). From the two measurements at $\theta = 0$ and 90° , we can extract the spin-orbit magnetic fields B_{SIA} and B_{BIA} . Normalized to a gate modulation amplitude

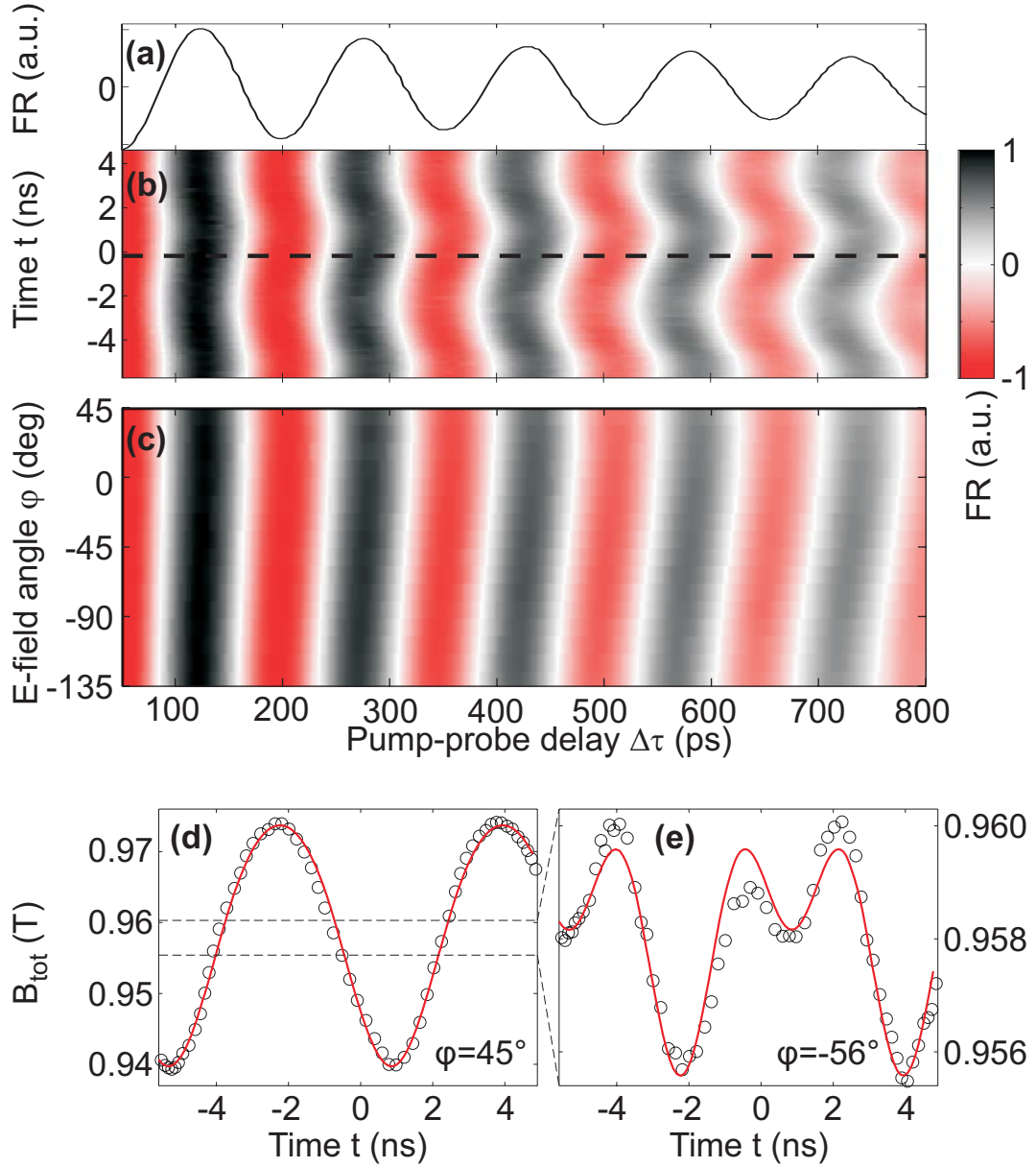


Figure 5.3: TRFR signal measured at different times t and electric field angles φ , at $\theta = 45^\circ$. (a) Faraday rotation vs. pump-probe delay. (b) TRFR scans at different times t , the dashed line indicates $t = 0$. (c) TRFR scans at different angles φ , at $t = 0$. (d, e) Total magnetic field as a function of t for (d) $\varphi = 45^\circ$ and (e) $\varphi = -56^\circ$. The solid line is a fit to Eq. (5.11).

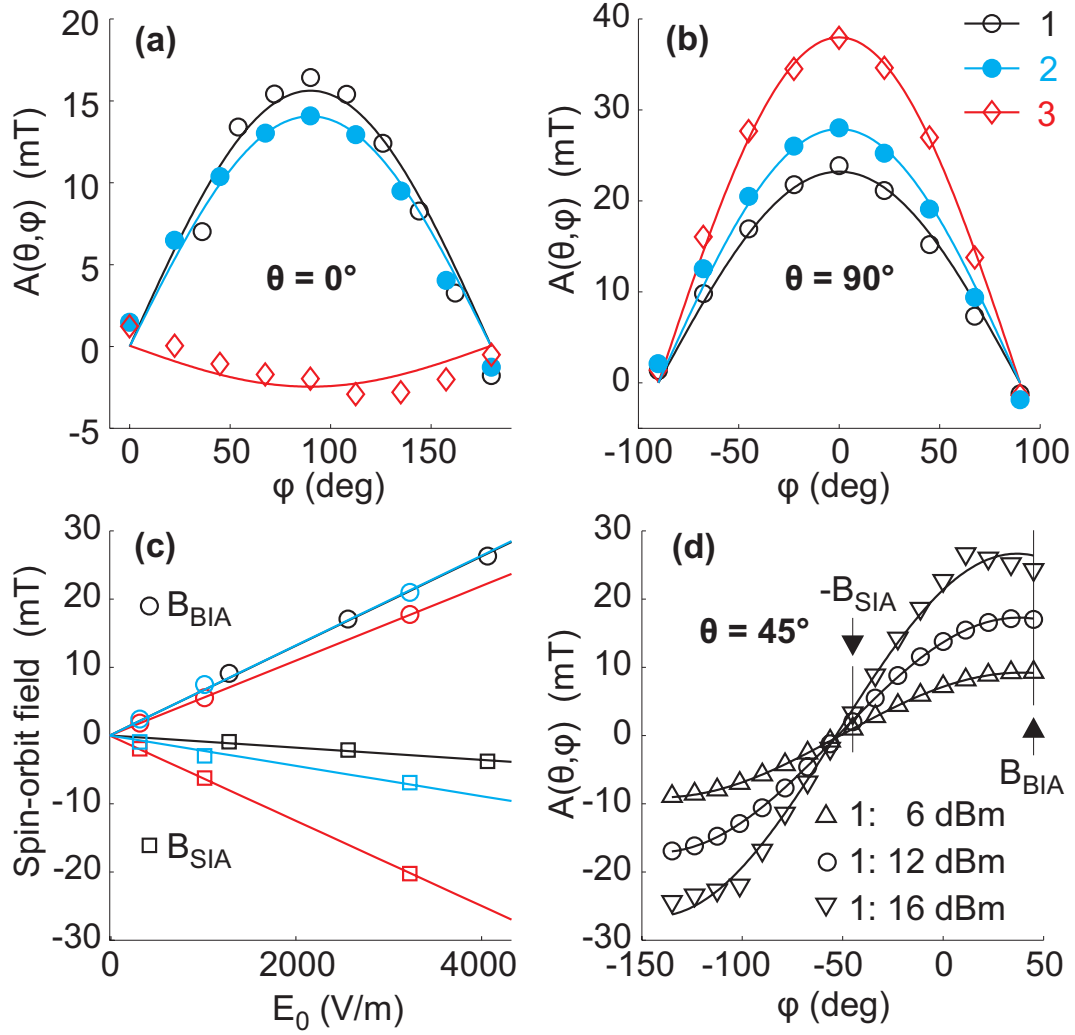


Figure 5.4: Spin-orbit fields as a function of φ for $\theta = 0, 90^\circ$ and 45° . Depending on θ , we measure **(a)** $(B_{\text{BIA}} + B_{\text{SIA}}) \sin \varphi$ [at $\theta = 0$] or **(b)** $(B_{\text{BIA}} - B_{\text{SIA}}) \cos \varphi$ [at $\theta = 90^\circ$]. The gate modulation amplitude was 12 dBm for sample 1 and 14 dBm for samples 2 and 3. **(c)** Both B_{SIA} and B_{BIA} increase linearly as a function of the electric field. **(d)** For $\theta = 45^\circ$, the measured spin-orbit field is $B_{\text{BIA}} \cos(\varphi - \pi/4) + B_{\text{SIA}} \sin(\varphi - \pi/4)$ with a linear dependence on the applied gate voltage. At $\varphi = 45^\circ$, we directly measure B_{BIA} , and at $\varphi = -45^\circ$, $-B_{\text{SIA}}$.

of $V_0 = 2$ V (≈ 13 dBm), corresponding to an electric field of $E_0 \approx 2900$ V/m, we find the following values for the spin-orbit magnetic fields:

sample number	substrate	B_{SIA} (mT)	B_{BIA} (mT)
1	P919	-4.2	21.6
2	P805	-8.5	21.1
3	ES887	-17.6	15.7

Note that as t is known up to an offset t_0 , the sign of $A(\theta, \varphi)$ is arbitrary, leading to an uncertainty in the absolute sign of B_{SIA} and B_{BIA} (the relative sign is obtained). We choose $B_{\text{BIA}} > 0$. As a function of the magnitude of the applied electric field E_0 , B_{SIA} and B_{BIA} increase linearly (see Fig. 5.4c), as expected from the linear relation between $k(t)$ and $E(t)$ and Eq. (5.7). We have conducted the same measurements at different magnitudes of $B_{\text{ext}} = 0.55$ and 0.82 T, and found similar values for the spin-orbit fields.

As discussed above, measurements at two angles, $\theta = 0$ and 90° , were needed to obtain B_{SIA} and B_{BIA} . At $\theta = 45^\circ$ both B_{SIA} and B_{BIA} can be determined simultaneously. This is because not only the amplitude, but also the phase of the oscillation in φ contains information about the spin-orbit fields. The zero-crossing of $A(\theta, \varphi)$ occurs at $\varphi_0 = \arctan [(B_{\text{SIA}} - B_{\text{BIA}})/(B_{\text{SIA}} + B_{\text{BIA}})]$, compared with $\varphi_0 = \theta$ for $\theta = 0$ and 90° . For $\theta = \varphi = 0$ and 90° , \mathbf{B}_{SIA} and \mathbf{B}_{BIA} are perpendicular to \mathbf{B}_0 (Fig. 5.1a and b) and $A(\theta, \varphi)$ vanishes, because it is equal to the component of $\mathbf{B}_{\text{SIA}} + \mathbf{B}_{\text{BIA}}$ along the direction of \mathbf{B}_0 . If however $\theta = \varphi = 45^\circ$, \mathbf{B}_{SIA} still is perpendicular to \mathbf{B}_0 , but \mathbf{B}_{BIA} is now parallel, and $A(\theta, \varphi) = B_{\text{BIA}}$.

The measurement at $\theta = 45^\circ$ is shown in Fig. 5.4d, with a fit to Eq. (5.11). For $V_0 = 2$ V, we extract the spin-orbit fields $B_{\text{SIA}} = -2.4$ mT and $B_{\text{BIA}} = 19.1$ mT for sample 1. These values correspond well to the values obtained from $\theta = 0$ and 90° . Relative variations in B_{SIA} of up to 50% (but far less in B_{BIA}) occurred for different cool-downs of the same sample, which we attribute to the freezing of electron states in the QW interface or to strain.

Knowing the electron g -factor and drift wave vector k , we can calculate the coupling constants α and β from B_{SIA} and B_{BIA} using Eq. (5.7). For sample 3, where the mobility is known ($\mu = 10^6 600$ cm²/Vs, see Sect. 2.5.3), we can extract the values of α and β from B_{SIA} and B_{BIA} . Note that for this, we need to know the electron drift wave vector k , which we obtain from the mobility μ and the in-plane electric field from the gate electrodes E_0 according to Eq. (5.8). While the mobility can be measured in transport experiments, we have to rely on simulations for the electric field E_0 , see the next Sect. 5.2.5. An error in the estimation of E_0 linearly transforms into an error in α or β , for which we obtain

$$\begin{aligned} \alpha &= \hbar g \mu_B B_{\text{SIA}} / m^* \mu E_0 = 1.5 \times 10^{-13} \text{ eV} \cdot \text{m}, \text{ and} \\ \beta &= \hbar g \mu_B B_{\text{BIA}} / m^* \mu E_0 = -1.4 \times 10^{-13} \text{ eV} \cdot \text{m}. \end{aligned} \quad (5.12)$$

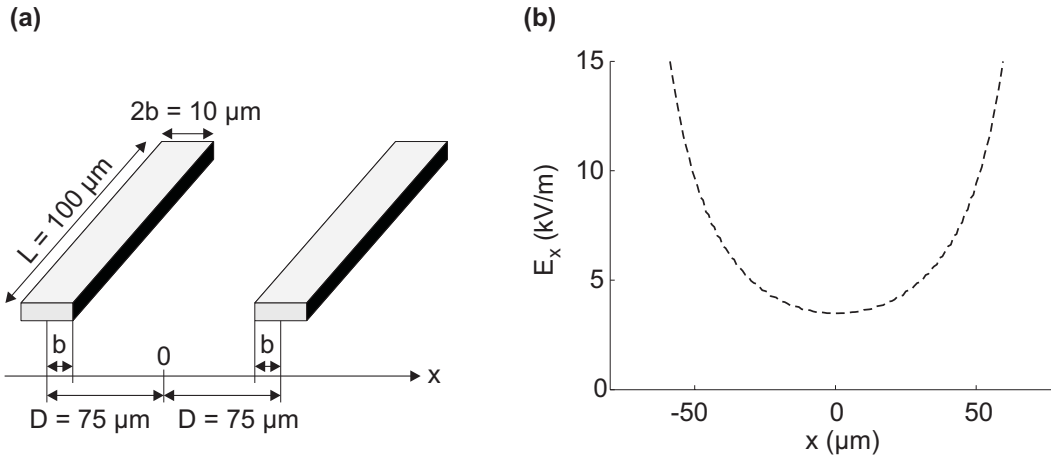


Figure 5.5: (a) Gate geometry and coordinate system used for the calculation of the electric field. (b) Electric field between two gates for gate potentials of +1 and -1 V, simulated for $L = \infty$.

We have used $g = -0.27$, as independently measured by TRFR in a known external magnetic field and assuming $g < 0$. Previous experiments report $\alpha \approx 5 - 10 \times 10^{-12}$ eV·m on $\text{In}_{0.53}\text{Ga}_{0.47}\text{As}/\text{In}_{0.52}\text{Al}_{0.48}\text{As}$ QWs or heterostructures [94, 98, 101] and in InAs/AlSb QWs [105] and assume $\alpha \gg \beta$. The Rashba coupling is proportional to the average electric field in the *valence* band (Sect. 5.1.1), including contributions from band discontinuities. We estimate the valence band offset in our QWs to be on the order of 10 meV, which is much smaller than in those previously investigated structures, and explains our small value of α . Our α is about four times larger than that reported in ref. [71], where an $\text{In}_{0.07}\text{Ga}_{0.93}\text{As}$ epilayer (10 times thicker than our QW) was studied. There, the interfaces play a minor role and strain-induced spin-orbit coupling predominates. The linear Dresselhaus term is expected to scale with the extent of the wave function in the confinement direction, $\langle k_z^2 \rangle$, and $\beta \propto 1/\ell^2$. Assuming that samples 1 and 2 have similar mobilities, we observed almost the same β , even though the QW in sample 2 is twice as wide as that in sample 1. This could be attributed to inhomogeneous In deposition during growth, leading to a triangular confinement potential, where the nominal QW width has less influence on β .

5.2.5 Determination of the electric field between the gate electrodes

To determine α and β from B_{SIA} and B_{BIA} , we needed to know the electron drift wave vector (see Eq. 5.7). If we were dealing with ballistic electrons in an electric field \mathbf{E} , the electron wave vector would steadily increase with time, since the electrons

would feel a constant force $\mathbf{F} = -|e|\mathbf{E}$, and in the non-relativistic limit,

$$\mathbf{k} = \frac{m^*\mathbf{v}}{\hbar} = -\frac{|e|\mathbf{E}}{\hbar}t.$$

In the presence of scattering, however, the electron velocity is limited. In the Drude model (see, e.g., [114]), the scattering is taken into account by introducing an average drift velocity

$$\langle \mathbf{v} \rangle = \mu \mathbf{E},$$

where the mobility $\mu = e\tau/m^*$ is related to the average time τ between two scattering events. With $\mu = 10'600 \text{ cm}^2/\text{Vs}$, taken from transport measurements, we obtain $\tau \approx 0.5 \text{ ps}$. This scattering time is much shorter than our a.c. modulation period $1/f \approx 6 \text{ ns}$. Therefore, we can assume that the electron velocity is proportional to $E(t)$, as already implicated by Eq. (5.8).

For a precise knowledge of k , both μ and E need to be known. Assuming that the two opposite gates are infinitely thin and infinitely long wires, separated by a distance $2D$ and with a charge density $\pm\lambda \text{ [C/m]}$, the electric field induced in the plane of the two wires as a function of the distance x from the center (see Fig. 5.5a with $b = 0$ and $L = \infty$) is

$$E_\infty(x) = \frac{\lambda}{2\pi\epsilon\epsilon_0} \left(\frac{1}{x+D} - \frac{1}{x-D} \right). \quad (5.13)$$

In GaAs, $\epsilon = 13$. Taking into account the finite length L of the two gates, we can still find an analytical expression for the electric field

$$E_L(x) = \frac{Q}{4\pi\epsilon\epsilon_0} \left(\frac{1}{(x+D)\sqrt{(x+D)^2 + (L/2)^2}} - \frac{1}{(x-D)\sqrt{(x-D)^2 + (L/2)^2}} \right), \quad (5.14)$$

where $\pm Q$ is the charge per gate. Both expressions require that the charge per length or per gate is known³. Therefore, an integration of the electric field given in Eq. (5.13) and (5.14) would be necessary. This is difficult, since $E(x)$ diverges for $|x| \rightarrow D$ and secondly, because close to $|x| = \mp D \pm b$, the field E is determined by the finite width b of the gates and is therefore incorrectly estimated by Eq. (5.13) and (5.14). From the analytical calculations we note that at $x = 0$, the electric field calculated for a finite L [Eq. (5.14)] is reduced compared to the case with $L = \infty$ [Eq. (5.13)] by a factor

$$r = \frac{E_L(x=0)}{E_\infty(x=0)} = \left(\sqrt{\left(\frac{2D}{L}\right)^2 + 1} \right)^{-1} \approx 0.55. \quad (5.15)$$

³The charge could be determined from a capacitance measurement. However, in such a measurement, stray-capacitances are also included, and the charge which is on the gates is difficult to extract.

To take into account the influence of the finite width b of the gates on the electric field, we simulated the potential between both gates using a two-dimensional partial differential equation solver (`pdetool` in `Matlab`). The electric field obtained this way is plotted in Fig. 5.5b. Because this two-dimensional simulation again assumes $L = \infty$, we reduce the electric field at $x = 0$ by the factor r obtained above. Then, $E(x = 0) = 2.9$ kV/m for one gate on a potential of -1 V, the other on $+1$ V. This corresponds to the situation with a ‘gate modulation amplitude’ of 1 V (13 dBm). Since our system is only 50 Ohms on the generator side and not terminated on the gate side, the modulation at the gates effectively is 2 V. Note that the samples here have much smaller capacitances than the gratings in chapter 4 and at $f = 160$ MHz, damping in the system is less pronounced than at higher frequencies (Sect. 4.2.1). Between 1 and 2 dBm are lost between the a.c. generator and the chip socket, as measured with a high-impedance probe.

The electric field at $x = 0$ is aligned almost perfectly along x , within $|x| < 10 \mu\text{m}$, $E_z < 50$ V/m.

5.3 Spatially resolved measurements

5.3.1 Large-area scans

In the previous chapter, Sect. 4.2.4, we have observed an oscillating electron precession frequency ν as a function of the laser-gate delay t beside interdigitated gratings that were biased with an a.c. gate voltage. We have attributed these oscillations to the effect of a spin-orbit magnetic field. With the findings of the previous Sect. 5.2, we are now able to determine the spin-orbit magnetic field acting on electrons that oscillate in a local electric field induced by gate electrodes.

For the estimation of such a local spin-orbit magnetic field, we first need to know the electric field in the scanned region. Figure 5.6 shows the electric potential distribution simulated with `pdetool` for the sample used in Sect. 5.2 above. Different gates have been set on a potential of $V_{\text{a.c.}} = 1$ V, others have been grounded. This again is a two-dimensional simulation, neglecting the fact that the QW is not exactly in the plane of the gates, but rather 40 nm lower. However, since we are interested in lateral distances from the gates on the order of $10 \mu\text{m}$, the vertical offset is negligible and we can assume that the gates and the QW are in the sample plane and that out-of-plane components of the electric fields are negligible.

From the potential distribution in Fig. 5.6, we derive the electric field. With Eq. (5.8), we then determine a local drift k -vector and, based on Eq. (5.10), the magnitude of the spin-orbit magnetic field. Neglecting the term in $(k/B_{\text{ext}})^2$, we

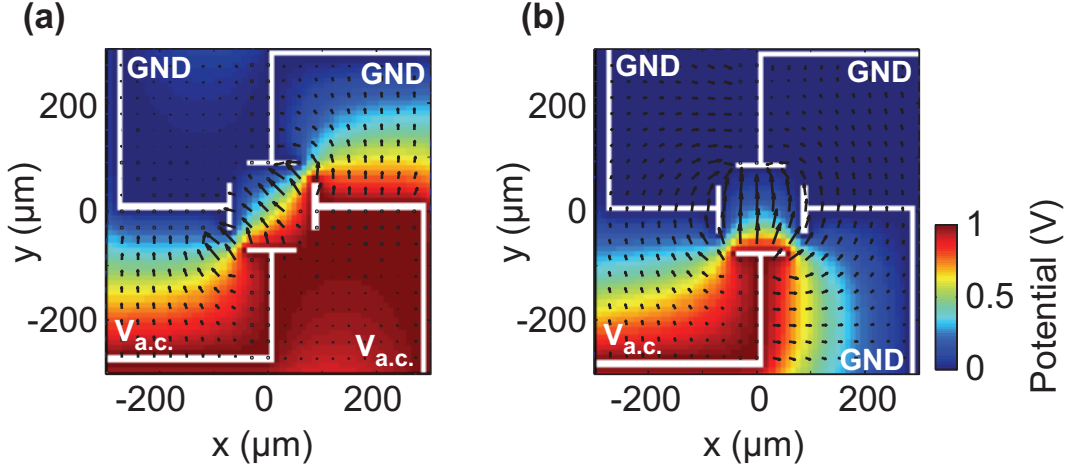


Figure 5.6: Simulations of the potential distribution and the electric field between the gate electrodes and the wire-gates for two different configurations. (a) Bottom and right electrode biased, (b) only bottom electrode biased.

solve Eq. (5.10) for the absolute, *observed* value of the spin-orbit field

$$\begin{aligned}
 B_{\text{so}}^* &= |\mathbf{B}_{\text{tot}}| - |\mathbf{B}_{\text{ext}}| \\
 &= B_{\text{ext}} \sqrt{1 + \frac{2k_0}{g\mu_B B_{\text{ext}}} ([\alpha + \beta] \cos \theta \sin \varphi + [\beta - \alpha] \sin \theta \cos \varphi) - B_{\text{ext}}} \\
 &\approx B_{\text{ext}} \left(1 + \frac{1}{2} \frac{2k_0}{g\mu_B B_{\text{ext}}} ([\alpha + \beta] \cos \theta \sin \varphi + [\beta - \alpha] \sin \theta \cos \varphi) \right) - B_{\text{ext}} \\
 &= \frac{k_0}{g\mu_B} ([\alpha + \beta] \cos \theta \sin \varphi + [\beta - \alpha] \sin \theta \cos \varphi).
 \end{aligned} \tag{5.16}$$

This equation can further be simplified using Eq. (5.7) to

$$B_{\text{so}}^* \approx (B_{\text{SIA}} + B_{\text{BIA}}) \cos \theta \sin \varphi + (B_{\text{BIA}} - B_{\text{SIA}}) \sin \theta \cos \varphi. \tag{5.17}$$

Note that there are three mechanisms that determine the *observed* magnitude B_{so}^* : firstly, the magnitude of the spin-orbit field is proportional to the local strength of the electric field. Secondly, the local orientation φ of the electric field determines how \mathbf{B}_{SIA} and \mathbf{B}_{BIA} add up to \mathbf{B}_{so} , see Fig. 5.1. And thirdly, the orientation θ of \mathbf{B}_{ext} decides, analogously to a projection, how much of $|\mathbf{B}_{\text{so}}| = |\mathbf{B}_{\text{SIA}} + \mathbf{B}_{\text{BIA}}|$ is actually observed in the experiment. We denote this by a star in the quantity B_{so}^* .

In the simulation, we can now use the values for B_{SIA} and B_{BIA} that were obtained at $E_0 = 2900$ V/m for the three samples above in Sect. 5.2 and scale them with the magnitude of the local electric field. The angles φ and θ are determined by the local orientation of the electric field and by the global orientation of B_{ext} , respectively. Equation (5.17) then provides the spatial variation of B_{so}^* on the sample surface. Figure 5.7b shows B_{so}^* obtained in such a simulation over a sample area $250 \times$

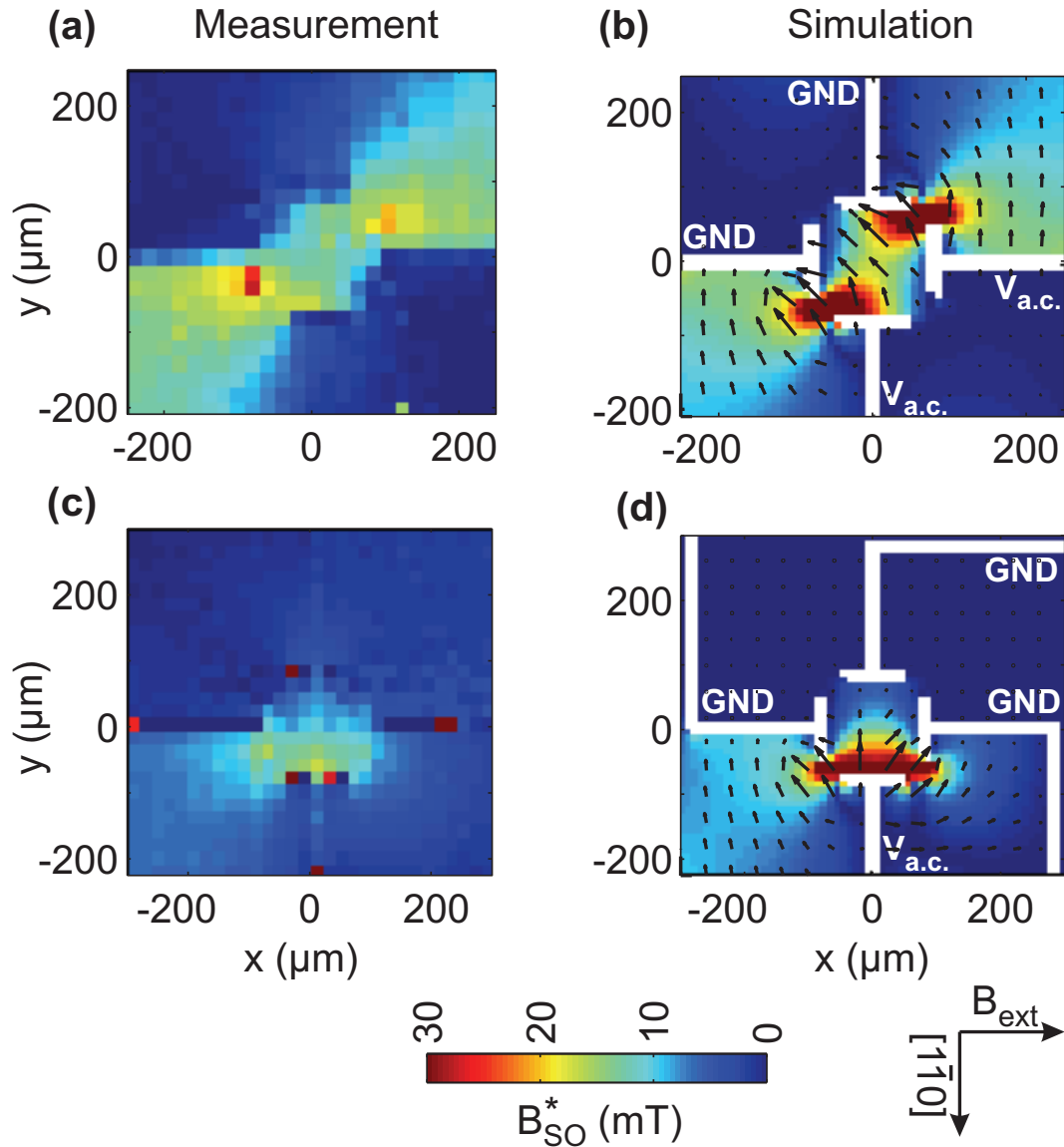


Figure 5.7: Spatially resolved measurements of the spin-orbit magnetic field B_{so}^* on sample P805 with B_{ext} oriented at $\theta = 90^\circ$ with respect to the crystal's $[1\bar{1}0]$ -direction. **(a,b)** Lower and right electrode excited with and a.c. voltage (r.f. power 12 dBm). **(c,d)** Bottom electrode excited. Left column: measurement, right column: simulation assuming $B_{\text{SIA}} = -8$ mT and $B_{\text{BIA}} = 20$ mT. Arrows indicate the direction and magnitude of the electric field.

250 μm with the gates on a potential as simulated in Fig. 5.6a. The corresponding measurement is shown in Fig. 5.7a. The agreement with the simulation is good, except for the values of B_{so}^* measured close to a gate edge that are by a factor of ≈ 2 lower than in the simulation. There, the simulation assumes perfect edges leading to very high electric fields. In reality, the edges are rough and round and the electric field is lower. Secondly, the simulation is only two-dimensional and neglects the finite extension of the gates perpendicular to the QW plane (see Sect. 5.2.5).

The two ‘horizontal’ (along x) wire-gates induce strong ‘vertical’ (along z) electric fields. With the $[\bar{1}10]$ -axis oriented vertically, these fields lead to a k -vector in direction of this axis, and, as visible from the orientation of the spin-orbit fields in Fig. 5.1, to a spin-orbit magnetic field pointing in the direction of \mathbf{B}_{ext} . If \mathbf{B}_{ext} and \mathbf{B}_{so} are parallel, the contribution of the latter to the total field B_{tot} is not reduced by a geometrical factor and therefore, we measure a large B_{so}^* close to the horizontal wire-gates. In contrast, the high horizontal electric fields close to the vertical wire-gates also lead to large spin-orbit fields. However, since the resulting electron motion is in $[110]$ -direction, the spin-orbit fields are vertical (Fig. 5.1) and perpendicular to \mathbf{B}_{ext} , leading to no first-order effect on B_{tot} and therefore, $B_{\text{so}}^* = 0$.

In Fig. 5.7d, a simulation of B_{so}^* is shown for the gate potential in Fig. 5.6b, and in Fig. 5.7c we present the corresponding measurement. Again, the qualitative agreement, and away from the sharp edges of the gates also the quantitative agreement, is good. Strong vertical electric fields in the lower left lead to a high value of B_{so}^* in the measurement, since, as mentioned above, \mathbf{B}_{ext} and \mathbf{B}_{so} are parallel.

5.3.2 Scans with a rotating electric field

Two-dimensional scans of the spin-orbit field between the four gate electrodes are shown in Fig. 5.8. Here, the angle φ of the electric field has been rotated by 30° in each step, as in the experiments presented in Sect. 5.2. In those experiments, the spin precession frequency was monitored in the center of the four gate electrodes. Here, the whole area between the gates is scanned with the same method as already described above. The electric field is rotated by applying variable gate voltages to the bottom and the right gate electrodes, such that the electric field is oriented at the desired angle in the center of the electrodes. This direction is indicated by an arrow in Fig. 5.8 between the measurement (left column) and the simulation (right columns).

The simulation again is in good agreement with the measurement, except close to edges, where the simulated electric field and therefore, also B_{so}^* is higher than observed. This measurement confirms that the technique of rotating the electric field, on which the results in Sect. 5.2 rely on, works and that the electric field, at least at some distance from the electrodes, is simulated realistically.

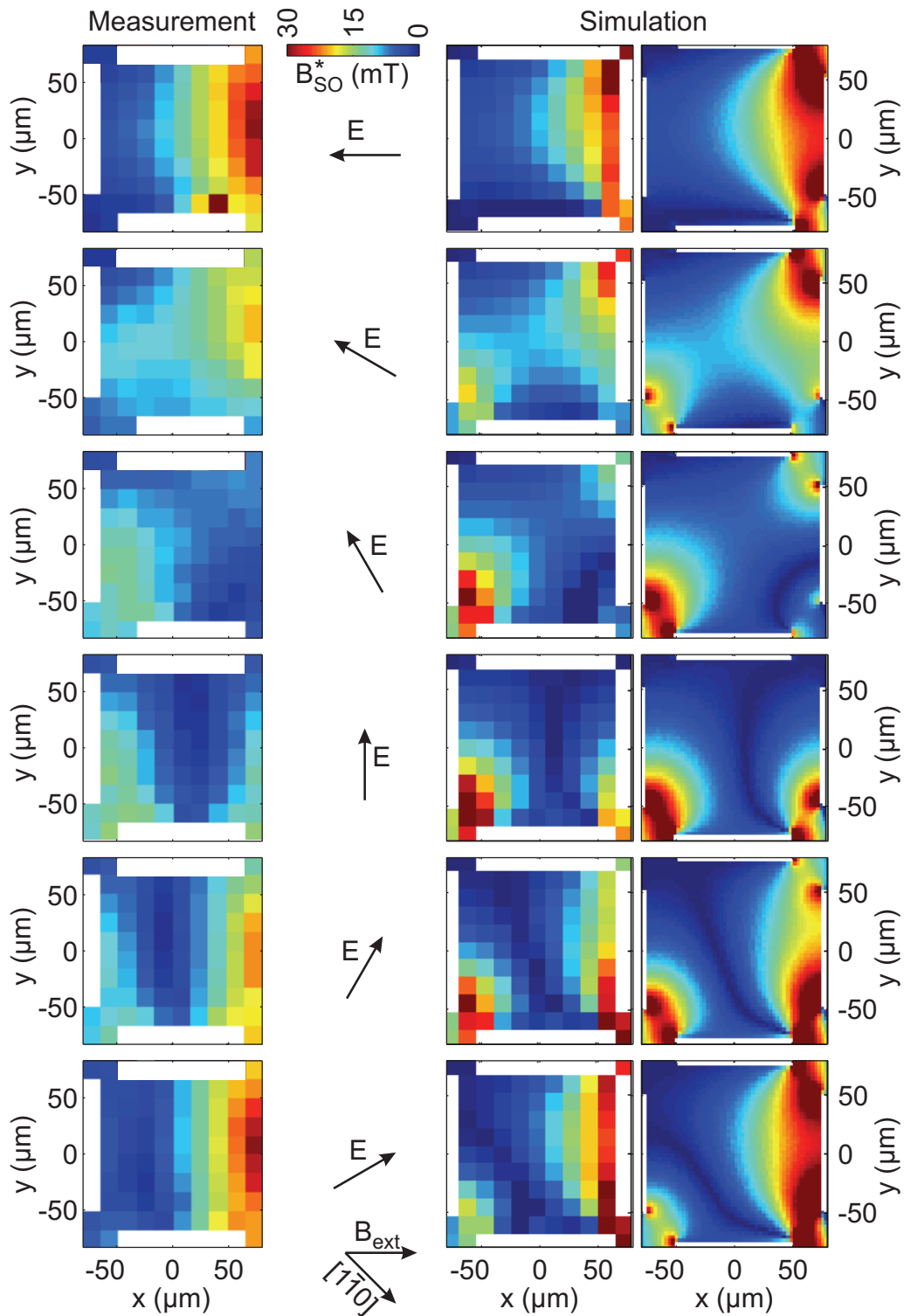


Figure 5.8: Measurement of the spin-orbit magnetic field B_{so}^* between four gate electrodes on substrate P919 oriented at $\theta = 45^\circ$ for different orientations of the electric field ($\varphi = 225^\circ, 195^\circ, 165^\circ, 135^\circ, 105^\circ, 75^\circ$). Left column: measurement. Right columns: simulation assuming $B_{\text{SIA}} = -3$ mT and $B_{\text{BIA}} = 20$ mT, downsampled to match the measurement's resolution and in a high-resolution version.

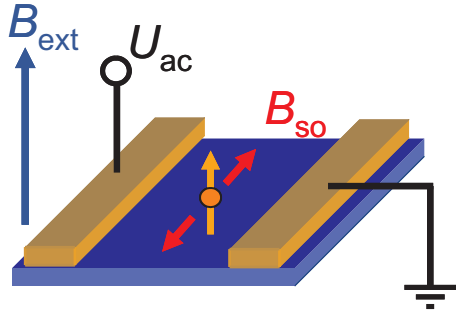


Figure 5.9: Setup for electric-dipole-induced spin resonance. The spins are polarized in the direction of an external magnetic field B_{ext} . The exciting electric field and the induced spin-orbit field are both in-plane of the QW.

5.4 Electric-dipole-induced spin resonance

5.4.1 Introduction and results

In electron spin resonance (ESR) experiments, spins that are initially polarized along the direction of a static magnetic field $B_{\text{ext}} = B_z$ perform Rabi oscillations between the states parallel and anti-parallel to B_z , if an a.c. magnetic field (the tipping field) is applied in the plane perpendicular to B_z and at the Larmor frequency $f = g\mu_B B_z/h$. Instead of an a.c. *magnetic* field, we use an a.c. *electric* field $E_x(t)$ in the plane of the QW (see Fig. 5.9). It induces an oscillating spin-orbit field $B_y(t)$, which can serve as a tipping field for ESR, in this context referred to as electric-dipole-induced spin resonance (EDSR) [115]. The measurements presented in Fig. 5.10 have been conducted in Faraday geometry with sample 1. Here, the external magnetic field B_z is parallel to the laser propagation and perpendicular to the QW plane. The pump laser pulse polarizes the spins into an eigenstate, in line with B_z , and the probe pulse monitors the spin polarization along z . In Fig. 5.10a, the pump-probe delay $\Delta\tau$ has been set to 3 ns, and the Faraday signal is recorded while sweeping the frequency f of $E_x(t)$ and B_z . On resonance, the optically generated spin polarization precesses about the spin-orbit-induced tipping field, and the TRFR signal at $\Delta\tau = 3$ ns becomes negative. We observe spin resonance with $|g| = 0.57$, which is confirmed by TRFR measurements of sample 1.

In Fig. 5.10b and c, TRFR scans are collected for varying B_z , monitoring the spin dynamics. At $B_z = 120$ mT, the Larmor frequency matches the electric field frequency $f = 960$ MHz and resonance occurs. Note that the short spin relaxation time of ≈ 1 ns strongly reduces the signal. At $\Delta\tau_s \approx 1800$ ps, the spins have performed a $\pi/2$ Rabi oscillation, yielding an estimate of the tipping field amplitude $B_y = 2h/g\mu_B 4\Delta\tau_s \approx 35$ mT. Here, the factor 2 takes into account the linearly (and not circularly) oscillating tipping field [116]. This value agrees well with the measurements of $|\mathbf{B}_{\text{SIA}} - \mathbf{B}_{\text{BIA}}| \approx 33$ mT at a gate modulation amplitude of $V_0 \approx 2.5$ V (15 dBm) and $\varphi = 0$.

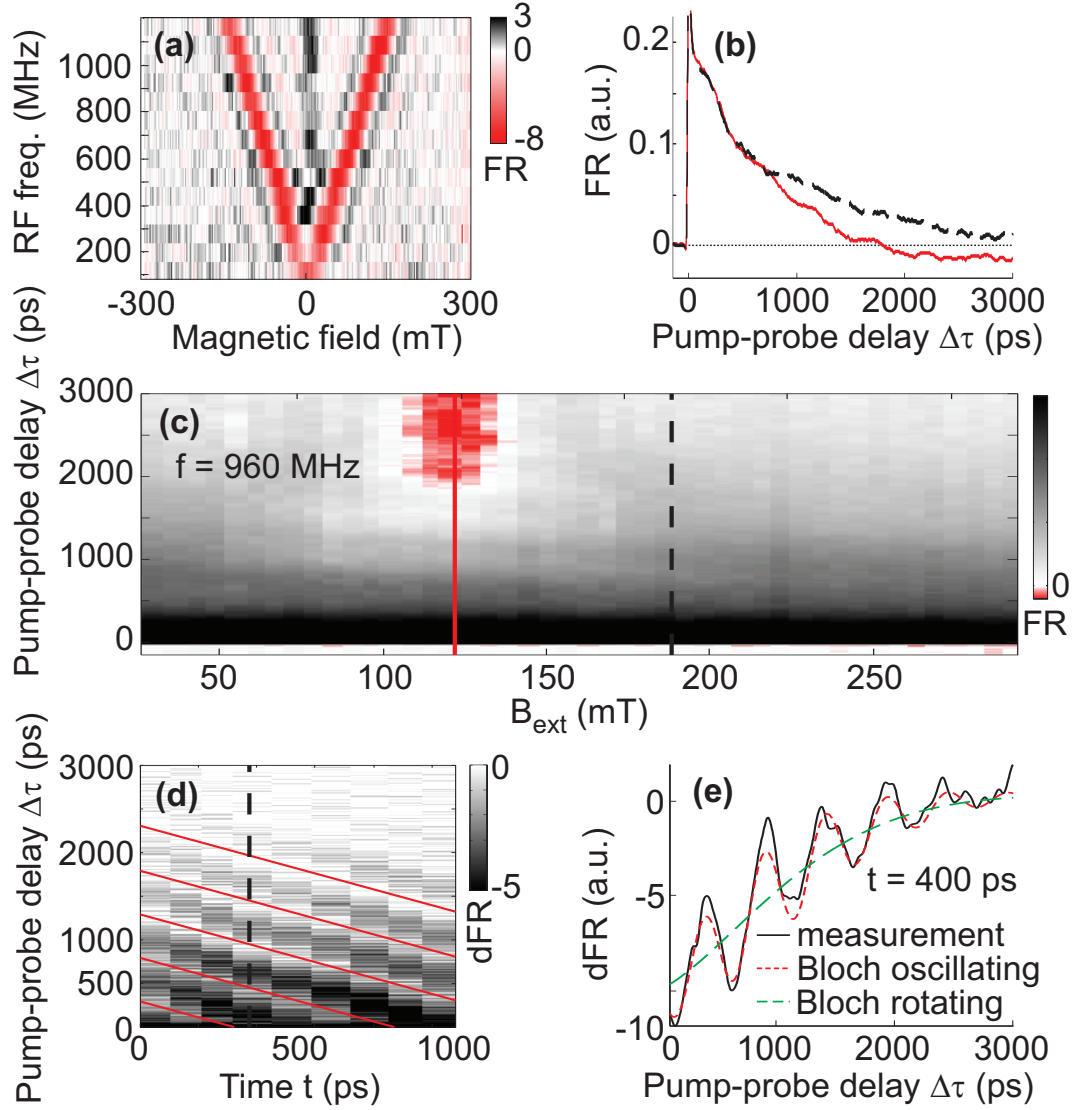


Figure 5.10: Spin resonance induced by an oscillating spin-orbit field. **(a)** TRFR signal at $\Delta\tau = 3$ ns for varying external magnetic fields B_z and electric field frequencies f . Resonance is observed with $|g| = 0.57$. **(b)** TRFR scans on (red line) and off (black line) resonance. **(c)** TRFR scans $\Theta_F(\Delta\tau)$ at different B_z . On resonance, the spins precess coherently about the spin-orbit induced-tipping field. **(d)** Differential TRFR signal $\dot{\Theta}_F(\Delta\tau + t)$ on resonance ($f = 960$ MHz), red lines are guides to the eye at $\Delta\tau = t$. **(e)** Measured $\dot{\Theta}_F(\Delta\tau) \propto \dot{S}_z(\Delta\tau)$ (solid line) and Bloch simulations with linearly oscillating (dotted) and rotating tipping field (dashed), at $f = 960$ MHz and $t = 400$ ps (solid line in **(d)**).

5.4.2 Comparison with Bloch equations

In ESR, one assumes a tipping field that oscillates circularly in the x/y plane, resulting in a monotonous decrease of the spin polarization along z during the first $\pi/2$ Rabi oscillation. The spin dynamics can then be solved analytically in the “rotating frame”. In EDSR, the Rabi oscillation on resonance is not steady with time (Fig. 5.10b), because the tipping field oscillates linearly on the y -axis instead. The precession of a spin is described by the Bloch equations (neglecting spin relaxation)

$$\dot{\mathbf{S}} = \frac{g\mu_B}{\hbar} \mathbf{B} \times \mathbf{S}, \quad (5.18)$$

from which we find $\dot{S}_z(t') = g\mu_B B_y(t') S_x(t')/\hbar$, where the dot denotes the time derivative and $t' = \Delta\tau + t$. The tipping field $B_y(t') \propto \sin(2\pi f t')$ and with it $\dot{S}_z(t')$ vanish twice per electric field period $1/f$, resulting in a stepwise decrease of S_z (on resonance, $S_x(t')$ and $B_y(t')$ vanish simultaneously). This is shown in Fig. 5.10d, where the time derivative of the Faraday signal $\dot{\Theta}_F(t') \propto \dot{S}_z(t')$ is plotted for different $\Delta\tau$ and t and for B_z on resonance. Apart from decaying with time, it is periodic in both $\Delta\tau$ and t , with period $1/2f$. The stepwise decrease of S_z can be reproduced by a numerical solution of the Bloch equations including a spin-relaxation term

$$\begin{aligned} \dot{S}_x &= \gamma(S_y B_z - S_z B_y) - S_x/T_2 \\ \dot{S}_y &= \gamma(S_z B_x - S_x B_z) - S_y/T_2 \\ \dot{S}_z &= \gamma(S_x B_y - S_y B_x) - (S_x - S_0)/T_1, \end{aligned} \quad (5.19)$$

where $\gamma = g\mu_B/\hbar$, T_1 is the longitudinal, T_2 the transverse spin lifetime, and S_0 the equilibrium spin polarization in z -direction. With $T_1 = T_2 = 1$ ns, $S_0 = 0$, $B_z = 120$ mT, $B_x = 0$ and $B_y(t) = 34$ mT $\sin(2\pi f t)$, we obtain good agreement with the measured \dot{S}_z , shown in Fig. 5.10e, together with the corresponding solution with a rotating tipping field. For the latter, the tipping field magnitude has to be reduced by a factor 2 [116].

Chapter 6

Outlook

6.1 Summary

In chapter 3, we have discussed the possibility to influence electron spins with magnetic stray fields. We have measured the average electron spin precession frequency ν of an ensemble of electron spins below arrays of ferromagnetic stripes. In a first step, we found ν to be enhanced by the magnetic stray field. Later, in chapter 4, we were able to tune this enhancement with an external gate voltage applied to the stripes. This voltage could even be modulated on gigahertz frequencies to control ν on a nanosecond timescale.

In chapter 5, we were able to separate the Rashba and Dresselhaus contributions to the spin-orbit interaction. We further used the spin-orbit magnetic fields as tipping field and were able to trigger electron spin resonance with electric fields.

6.2 Open questions

A spintronic device, like the Datta–Das spin–transistor ([47], c.f. Fig. 1.2), contains, additionally to the spin–manipulation functionality, a spin injection (Sect. 1.2) and a spin detection mechanism (Sect. 1.3). The purely optical spin polarization and probing techniques used in our experiments could be replaced by or combined with electrical spin injection and detection, possibly along with a reduction of the number of probed spins, currently an ensemble of roughly 10^4 electron spins [c.f. Eq. (A.2)].

Furthermore, the spin is moved within a spintronic device from source to drain. Spin packets drifting in an electric field have been investigated under the influence of spin-orbit interaction [71] or fields resulting from strain [108]. Spatial interference of spins has been demonstrated in an experiment where the spins travel through a ring structure and a phase difference between the two arms is induced by the effective

magnetic field from polarized nuclei in one arm [117]. Experiments that ‘follow’ an ensemble of initially polarized electron spins in space, subjected to magnetic stray fields or to spin-orbit coupling, would be a natural extension to the experiments presented in this thesis.

There is plenty of theoretical literature about spin-orbit coupling and in many experiments, spin-orbit coupling manifests in a rather indirect way (for example in beatings of SdH-oscillations or in (anti-)localization peaks). Our method of determining the Rashba and Dresselhaus coupling constants (chapter 5) provides direct access to the spin-orbit magnetic fields. Given that spin-orbit interaction is of crucial importance for spintronic applications, other materials (n - and p -type) with different Rashba and Dresselhaus coupling constants remain to be investigated, leading to a better understanding of the importance of Rashba and Dresselhaus couplings in different systems.

6.3 Suggestions for further experiments

6.3.1 Imaging magnetic stray fields

The influence of magnetic stray fields on the spin polarization of moving spins could be observed on thin epilayers, by passing currents close by ferromagnetic gates. Their magnetization and stray field can be changed by a small external magnetic field. The initial spin polarization could be generated optically or by electrical spin injection. The observation of the spin polarization would rely on a weak probe pulse, as described in chapter 2. The optical detection of spins has the advantage of providing two-dimensional resolution, down to $\approx 1 \mu\text{m}$ by using microscope objectives.

Such experiments could also be performed in a ring structure, where one arm is influenced by the stray field of a close-by ferromagnetic gate electrode, similar to [117]. The stray field of a this electrode could be switched on or off with a small external magnetic field and would change the spin-interference at the output of the ring. In contrast to nuclear fields, magnetic stray fields remain unchanged at room-temperature, and, provided that samples with spin lifetimes on the order of nanoseconds at room temperature are available (e.g., GaAs(110) QWs [46]), could allow for pioneering room-temperature spintronics experiments.

6.3.2 Spin-orbit-interaction-related experiments

Spin-orbit coupling in different materials

The method presented in Sect. 5.2 allows to unambiguously determine Rashba and Dresselhaus magnetic fields with high precision. It can in principle be used on any

semiconductor sample, even on insulating ones, where optical access to the electron spin precession is provided. The samples used in chapter 5 exhibit rather weak spin-orbit coupling. New samples could provide for much larger spin-orbit magnetic fields, especially by increasing the Rashba contribution according to Eq. (5.2). In particular, this would lead to higher tipping-fields in the EDSR-measurements (Sect. 5.4) and to the observation of several spin-flip cycles during the limited spin lifetime.

Secondly, experiments with GaAs(110) QWs could allow the measurement of spin-orbit coupling at room-temperature and give more insight in the suppression of the spin-orbit-induced spin relaxation in the DP-mechanism.

Spin-orbit tuning by electric fields

Samples with a contactable back and front gate and a QW sandwiched in between could exhibit a tunable Rashba spin-orbit field as a function of the voltage between front and back gate, see Eq. (5.2). In order to achieve high electric fields, the distance between front and back gate should be kept small, otherwise, the electric fields applicable might be too weak (c.f. appendix C). At the same time, a small distance will screen the *lateral* electric fields which induce the in-plane motion (and drift wave vector k) of the electrons. Therefore, it might be advantageous to replace the lateral gate electrodes by ohmic contacts and to induce a current in the QW. It remains to be investigated whether this current can be applied at a well-defined angle φ as the case for an in-plane electric field from gate electrodes.

k^3 -Dresselhaus term

As an extension to the measurements in Sect. 5.2, the cubic Dresselhaus term, see appendix B, and in particular Eq. (B.3), could be measured in bulk samples, or in a GaAs/AlGaAs 2DEG. The latter system was measured by Miller et al. [103]. In this work, Rashba, as well as linear and cubic Dresselhaus terms were estimated from weak localization and antilocalization measurements. Application of our direct measurement method could verify these estimates and give more precise values for the coupling constants α , β and γ .

Rashba and Dresselhaus interplay for $\alpha = \beta$

In Sect. 5.3, we have shown measurements that mapped the spin-orbit magnetic field in a spatially inhomogeneous a.c. electric field. In a continuation of these experiments, such two-dimensional scans could be performed on electron ensembles moving in different directions. By engineering α and β , the k -dependence of the spin-orbit magnetic field is influenced. Especially for $\alpha = \beta$, see Fig. 6.1a, the

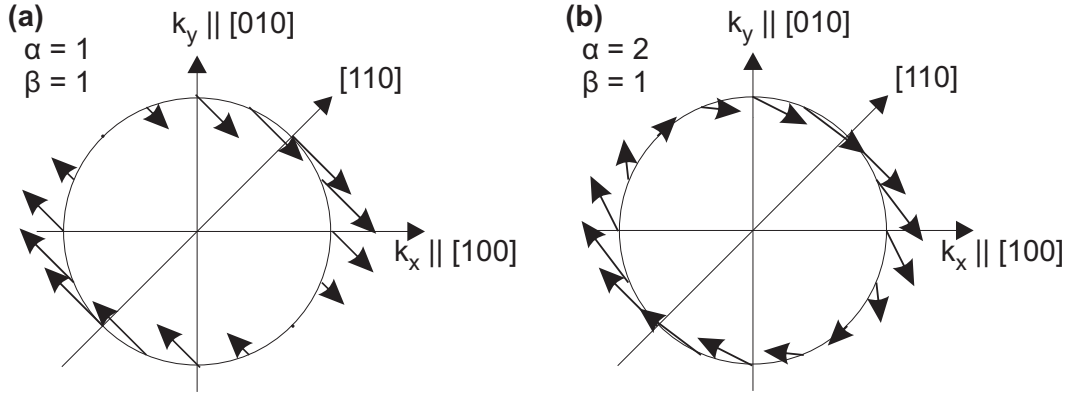


Figure 6.1: Orientation and magnitude of the sum of Rashba and Dresselhaus magnetic fields as a function of the wave vector \mathbf{k} for the cases (a) $\alpha = \beta$, and (b) $\alpha = 2\beta$.

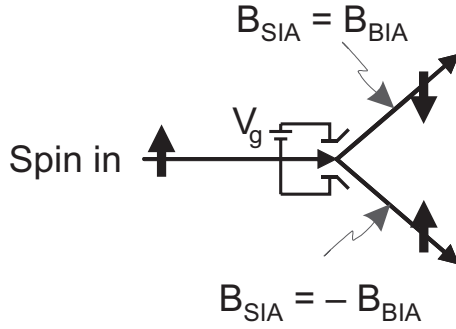


Figure 6.2: A simple spintronic device, exploiting the interplay between Rashba and Dresselhaus spin-orbit fields for the case $\alpha = \beta$.

Rashba and Dresselhaus fields cancel for \mathbf{k} in the $[1\bar{1}0]$ and $[\bar{1}10]$ directions. This leads to interesting effects, like the suppression of spin relaxation for spins moving along these directions. Additionally, the spin orbit field points along these two directions for all other \mathbf{k} , and therefore, this spin orientation is conserved. It has recently been proposed [118] that in such a system, if inducing an in-plane electron motion at a frequency f in resonance with an in-plane magnetic field, similar to the setup in Sect. 5.2, a non-vanishing spin-polarization perpendicular to the QW plane is expected. This S_z could be measured with TRFR.

A simple device

Such a \mathbf{k} -dependent magnetic field could be used to built a simple spintronic-device, analogous to a controlled NOT-gate (Fig. 6.2) for the case $\alpha = \beta$. A polarized spin enters this device, and a gate voltage V_g routs it into one of two paths, oriented at an angle of 90° to each other. On the lower path, the spin-orbit fields cancel (corresponding to the $[1\bar{1}0]$ -direction in Fig. 6.1a), while on the upper path, a nonzero spin-orbit field flips the spin orientation.

Appendices

A Time-resolved photoluminescence measurements

In Fig. A.1, we present time-resolved photoluminescence (TRPL) measurements at $T = 40$ K. The sample has been illuminated by a pulsed pump laser (repetition rate 80 MHz, pulse width 2 ps) at a wavelength of 750 nm, with a cw-power of 4 mW. The laser is focused on a grating with focus diameter 15 μm . We collect the light emitted by the sample and feed it through an optical fibre into a streak camera, which monitors the energy of the photons as a function of time.

Figure A.1a shows the time- and energy-dependence of the PL. In the energy-domain, two distinct peaks can be attributed to the PL of the QW at 1.42 eV and the GaAs-substrate at 1.51 eV. When applying a gate voltage to the grating (right panel), the intensity and the lifetime of the GaAs-peak does not change, but the QW-peak is reduced in both intensity and lifetime.

The PL integrated over time as a function of applied symmetric gate voltage V_g is shown in Fig. A.1b. As already mentioned, the intensity of the GaAs-peak below a Fe or Au grating does not change when gating the grating. The GaAs-peak is dominated by contributions from the GaAs-substrate and not the GaAs cap layer, since the absorption length (several μm [58, 119]) exceeds the cap thickness (20 nm) by far. Most of the probed substrate is thus far away from the electric field induced by the grating and its luminescence is therefore expected not to change with V_g .

The QW-peak, however, is strongly reduced in PL intensity when applying a gate voltage. The smaller the grating, the stronger this suppression: for $p = 6$, the PL intensity at $V_g = 2$ V is reduced by 20 % compared to $V_g = 0$ V. For $p = 1$, the suppression amounts to 80%.

We attribute this to an increased non-radiative recombination. Assuming no non-radiative recombination at $V_g = 0$, we can calculate the radiative and the non-radiative lifetime, see Fig. A.1c. The non-radiative lifetime $\tau_{\text{non-rad}}$ decreases strongly with V_g , whereas the radiative lifetime τ_{rad} increases slightly, especially for the small gratings, however, to a much smaller extent than already observed on a similar structure [120].

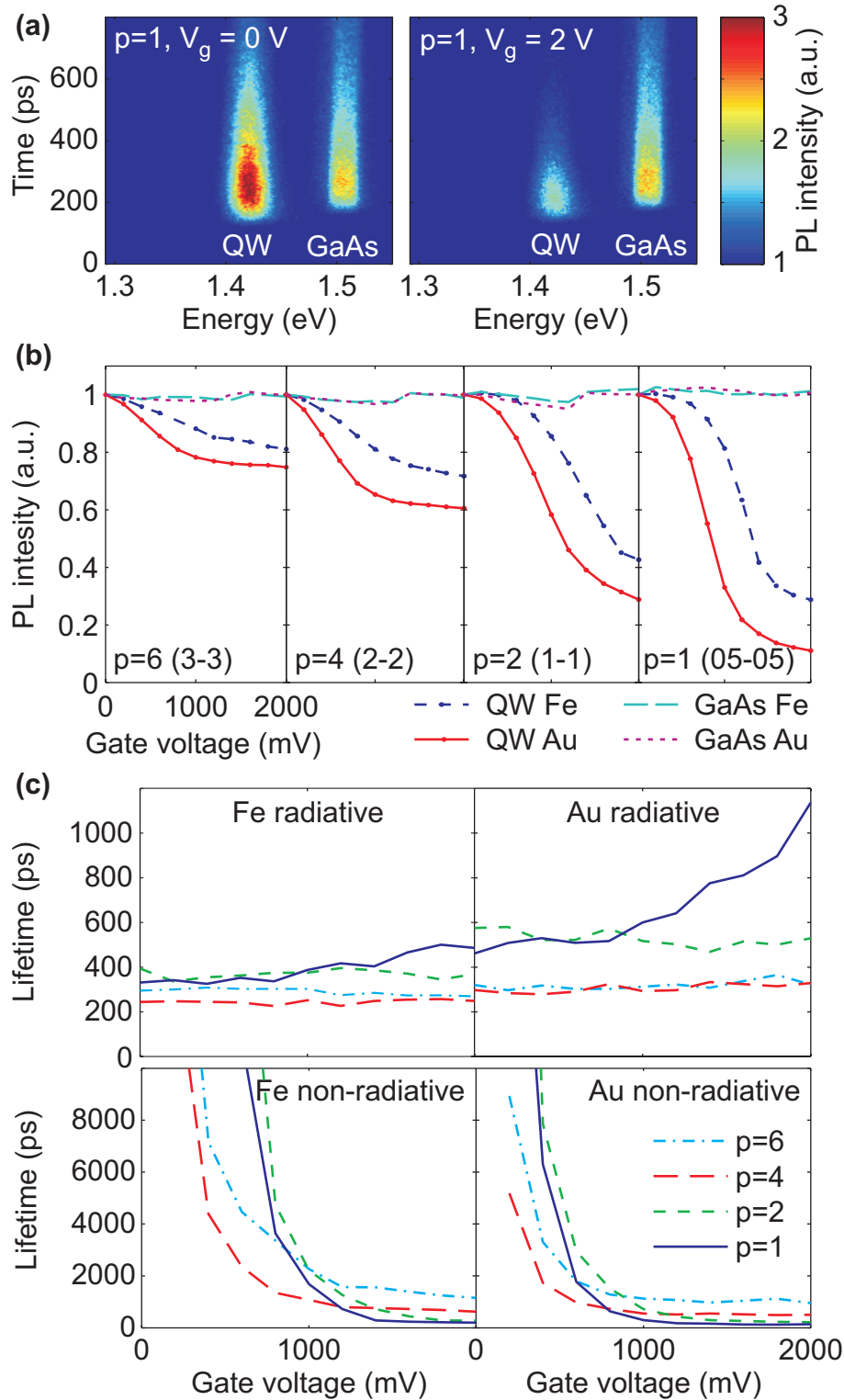


Figure A.1: (a) Time-resolved photoluminescence measured with a streak camera. PL of both the QW (1.42 eV) and the GaAs substrate (1.51 eV) are visible. (b) PL intensity integrated over time as a function of gate voltage applied to four different grating geometries. (c) Calculated radiative and non-radiative lifetimes below Fe and Au gratings.

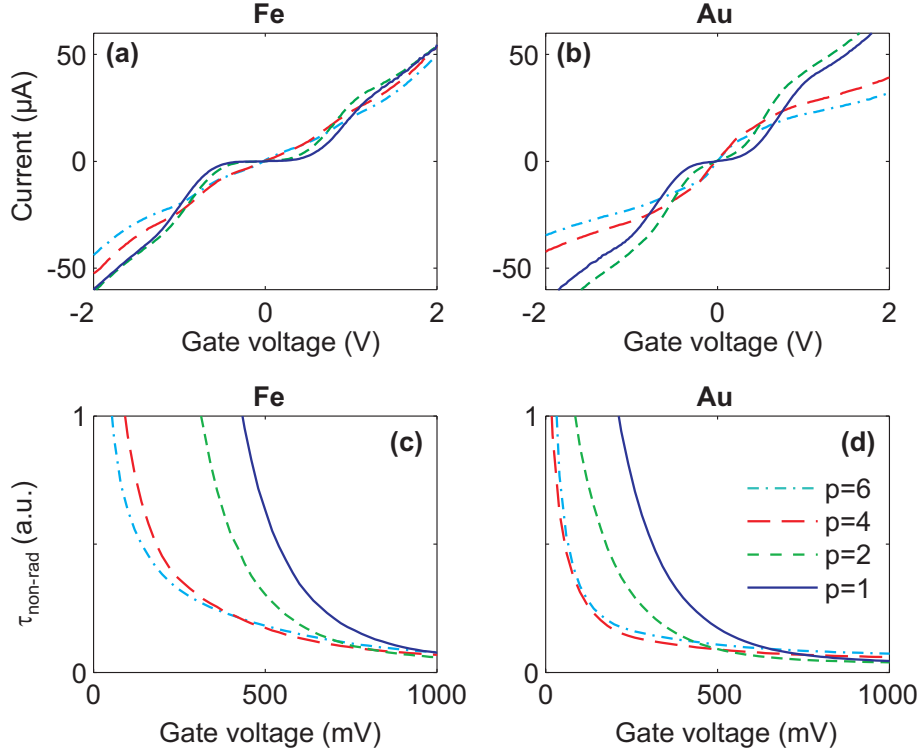


Figure A.2: **(a,b)** Current through Fe and Au gratings as a function of gate voltage. Gratings are illuminated in the center with pulsed laser light at a wavelength of 750 nm and $P = 4$ mW. **(c,d)** Qualitative estimate of the non-radiative lifetime.

The increased non-radiative recombination is explained by the rather high currents I (on the order of $10 \mu\text{A}$, see Fig. A.2a and b) that flow between the gates if the grating is illuminated. Therefore, electrons disappear into the gates before they recombine. If only optically excited electrons contributed to I , the non-radiative recombination rate would be given by

$$\tau_{\text{non-rad}}^{-1} = I/e. \quad (\text{A.1})$$

This, however, is only valid for a non-doped QW. In a doped QW, the situation is more complex and detailed knowledge about the fraction of optically excited and equilibrium electrons that participate in the current I is necessary in order to estimate $\tau_{\text{non-rad}}$. From Eq. (2.7), with $P = 0.5$ mW, $p = 0.001$ and from a rough estimate of the sheet density $n \approx 2 \times 10^{16} \text{ m}^{-2}$ (c.f. Sect. 2.5.2), we obtain for the optically excited electrons N_{opt} and the equilibrium electrons within the laser focus N_d ,

$$\begin{aligned} N_{\text{opt}} &\approx 10^4 \\ N_d &\approx (15 \mu\text{m})^2 n \approx 5 \times 10^6. \end{aligned} \quad (\text{A.2})$$

The current through an illuminated grating is thus dominated by N_d . The fact that a considerable current is only observed under illumination is attributed to the

reverse-biased Schottky barrier between the negatively charged bar and the QW. This barrier's resistance is reduced under illumination.

Nevertheless, we can qualitatively estimate $\tau_{\text{non-rad}}$ with Eq. (A.1). In Fig. A.2a and b, we show the I/V-characteristics of illuminated Fe and Au gratings. The resistance of a grating is on the order of 500 k Ω . In Fig. A.2c and d the qualitative estimates of $\tau_{\text{non-rad}}$ are given, obtained by Eq. (A.1) by assuming proportionality instead of equality. The non-radiative lifetime looks similar to the one calculated from optical measurements in Fig. A.1c. Note that the current through the gratings in Fig. A.2a and b is reduced by about one order of magnitude when illuminating the grating at a wavelength of 870 nm with a power $P = 0.5$ mW (as in TRFR-measurements).

On the small gratings ($p = 1, 2$), higher gate voltages are necessary to reduce $\tau_{\text{non-rad}}$ than on the large gratings. Assuming that a higher electric field between the bars leads to more electrons that recombine non-radiatively (since they are drawn into the bars), this is consistent with the behavior of the on-set gate voltage V_g^{on} discussed in Sect. 4.1.3 and could again be explained by the dependence of the electric field in the QW on the grating geometry, Eq. (4.2).

B Spin-orbit splitting with k^3 -dependence

Equation (5.10) described the total magnetic field including Rashba and Dresselhaus spin-orbit contributions linear in k . In bulk samples, and sometimes even in 2DEGs [103], cubic Dresselhaus terms (c.f. Eq. 5.4) are important. Here, we give the equivalent expression for Eq. (5.10), including linear and cubic spin-orbit contributions. The spin-orbit magnetic fields are given by

$$\begin{aligned}\mathbf{B}_{\text{SIA}} &= \frac{\alpha}{g\mu_B} \begin{pmatrix} k_y \\ -k_x \end{pmatrix} \\ \mathbf{B}_{\text{BIA},1} &= \frac{\beta}{g\mu_B} \begin{pmatrix} k_x \\ -k_y \end{pmatrix} \\ \mathbf{B}_{\text{BIA},3} &= \frac{\gamma}{g\mu_B} \begin{pmatrix} k_x k_y^2 \\ -k_y k_x^2 \end{pmatrix}.\end{aligned}\tag{B.1}$$

The geometrical dependence of these fields on the direction of k is shown in Fig. 5.1 and Fig. B.1. Note that for consistency with literature about the k^3 -Dresselhaus term, we chose x, y along [100], [010]. Analogously to the procedure in Sect. 5.2.2, the total field is given by

$$\mathbf{B}_{\text{tot}} = B_{\text{ext}} \begin{pmatrix} \cos \theta \\ \sin \theta \end{pmatrix} + \frac{1}{g\mu_B} \left(\alpha k(t) \begin{pmatrix} \sin \varphi \\ -\cos \varphi \end{pmatrix} + \beta k(t) \begin{pmatrix} \cos \varphi \\ -\sin \varphi \end{pmatrix} + \gamma k^3(t) \begin{pmatrix} \cos \varphi \sin^2 \varphi \\ -\sin \varphi \cos^2 \varphi \end{pmatrix} \right),\tag{B.2}$$

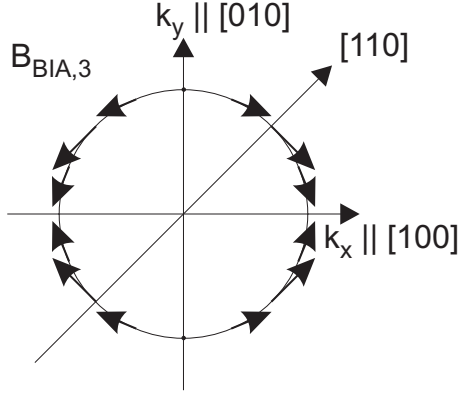


Figure B.1: k^3 -Dresselhaus magnetic field for different orientations of the k -vector on a unit circle.

where φ and θ are now the angles included with the $[100]$ axis. By rotating $\varphi' \rightarrow \varphi + 45^\circ$, and equivalently for θ , we obtain angles φ' and θ' with the $[1\bar{1}0]$ -axis, corresponding to the angles used in chapter 5.

After somewhat lengthy calculations, we find

$$\begin{aligned}
|\mathbf{B}_{\text{tot}}(t)|^2 &= B_{\text{ext}}^2 \\
&+ k(t) 2B_{\text{ext}} [\beta \cos(\theta + \varphi) - \alpha \sin(\theta - \varphi)] \\
&+ k^2(t) [\alpha^2 + \beta^2 + 2\alpha\beta \sin(2\varphi)] \\
&+ k^3(t) \frac{1}{2} B_{\text{ext}} \gamma [\cos(\theta + \varphi) - \cos(\theta - 3\varphi)] \\
&+ k^4(t) \left(\alpha\gamma \sin(2\varphi) + \frac{1}{2}\beta\gamma [1 - \cos(4\varphi)] \right) \\
&+ k^6(t) \frac{1}{8} \gamma^2 [1 - \cos(4\varphi)],
\end{aligned} \tag{B.3}$$

where we have included the factor $1/g\mu_B$ into the coupling constants, i.e. $\alpha \rightarrow \alpha/g\mu_B$ and equally for β and γ . Then, α and β are in units of T·m, and γ in T·m³. In the experiment, each k^n -term induces oscillations with a frequency $n \cdot f$ in $|\mathbf{B}_{\text{tot}}(t)|^2$. Those terms can be measured (provided they are large enough), by sweeping the laser-gate delay t in small steps.

C Tunability of the spin-orbit interaction?

The Rashba spin-orbit magnetic field is caused by electric fields that result from the structural asymmetry in a heterostructure. These fields point along the direction of growth, i.e. perpendicular to the QW plane in our samples. By applying an external electric field in the same direction, it has been shown [94, 98, 104, 105] that the Rashba coupling constant α , and with it B_{SIA} , can be tuned.

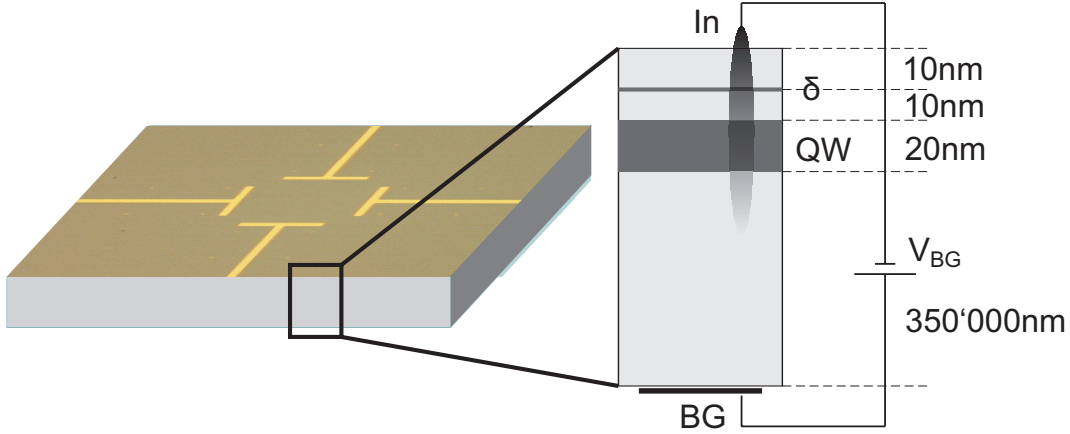


Figure C.1: Sketch of the back gate on sample 1. Voltages of around 100 V can be applied between an annealed In contact on the surface and a transparent back gate on the sample’s back side.

From the band structure of our QWs (Sect. 2.11) we estimate these ‘intrinsic’ electric fields in the interface of the QW (confinement $E_{\text{QW}} \approx 50$ meV, width $d \approx 20$ nm) to be on the order E_{QW}/d , equal to a few MV/m. Using a back gate on our sample, as shown in Fig. C.1, we are able to apply a voltage V_{BG} on the order 100 V between the transparent back gate (10 nm Au) and annealed In contacts on the sample surface. As mentioned before in Sect. 2.5.2, for this sample, it is unclear if only the QW, only the δ -doping layer or both are contacted with In ohmic contacts. Still, we can assume that by applying a voltage the QW is subjected to an electric field. The substrate P919 is 350 μm thick and therefore, an external electric field on the order of 0.3 MV/m is expected, about one order of magnitude smaller than the intrinsic electric field. On the one hand, a thinner sample would be advantageous to achieve a larger electric field. On the other hand, the back gate has to be farther away than the distance between the gate electrodes, since otherwise, the in-plane electric field between the gate electrodes would get diverted to the back gate and thereby screened.

Figure C.2a and b shows B_{SIA} and B_{BIA} as measured using the same technique as described in Sect. 5.2 as a function of back gate voltage V_{BG} . The three traces represent three cool-downs. Clearly, both B_{SIA} and B_{BIA} change with V_{BG} . The unexpected change of B_{BIA} with negative V_{BG} is attributed to a background effect, possibly originating from the changing electron density in the QW [104]. This background effect is expected to act on both spin-orbit fields and we therefore show their ratio in Fig. C.2c. As discussed in Sect. 5.1.1, the Rashba spin-orbit coupling in the conduction band is determined by the *conduction band* wave function’s expectation value of the electric field $\langle \mathcal{E}_z^v \rangle_c$ in the *valence band*. This is illustrated in Fig. C.3. The electron wave function in the conduction band of the QW (Fig. C.3a) has been placed in z -direction such that its expectation value of the electric field in the conduction band $\langle \mathcal{E}_z^c \rangle_c$ vanishes. The expectation value of the electric field in

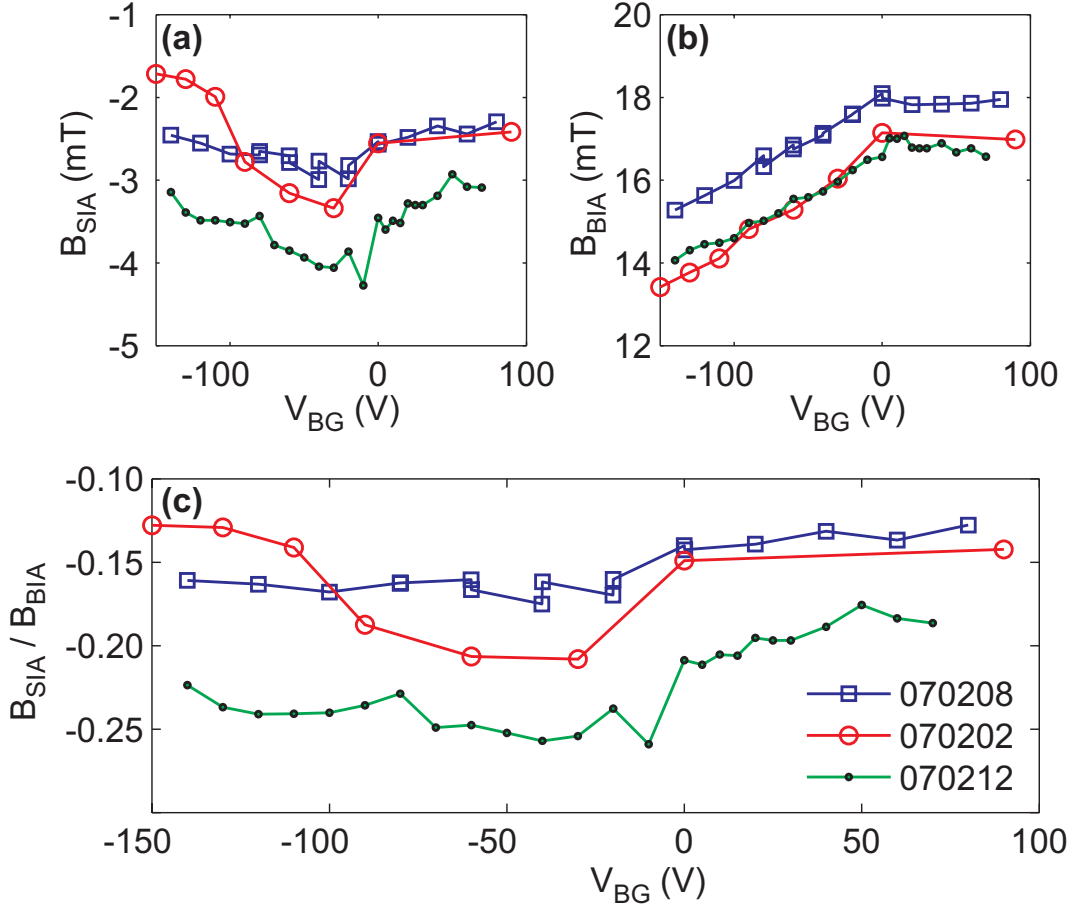


Figure C.2: (a) Rashba and (b) Dresselhaus magnetic fields and (c) their ratio as a function of back gate voltage V_{BG} . Data for three different cool-downs of the same sample.

the valence band, however, does not vanish for the conduction-band wave function, see Fig. C.3b, resulting in a finite Rashba coupling. By applying an external electric field in z -direction, the wave function is moved within the QW to a new equilibrium position, where $\langle \mathcal{E}_z^c \rangle_c = 0$. Again, $\langle \mathcal{E}_z^v \rangle_c \neq 0$. Figure C.3c shows the result of a numerical simulation, where the external electric field was swept. We determined the equilibrium position for a Gaussian-shaped wave function, defined by $\langle \mathcal{E}_z^c \rangle_c = 0$. Then, $\langle \mathcal{E}_z^v \rangle_c$ was calculated and plotted. Of course, the details depend on the shape of the wave function, but in general a monotonic increase in $\langle \mathcal{E}_z^v \rangle_c$, and so also in the Rashba spin-orbit magnetic field, was calculated.

In the normalized measurements (Fig C.2c), such a behavior was observed for the blue trace ‘070208’, and possibly also for the green trace ‘070212’ between $V_{BG} = -50 \dots +50$ V. The red trace ‘070202’ shows a non-monotonic dependence of the Rashba term on the external electric field. This observation might be explained by additional effects that stem from the doping layer, which, as mentioned, prohibits

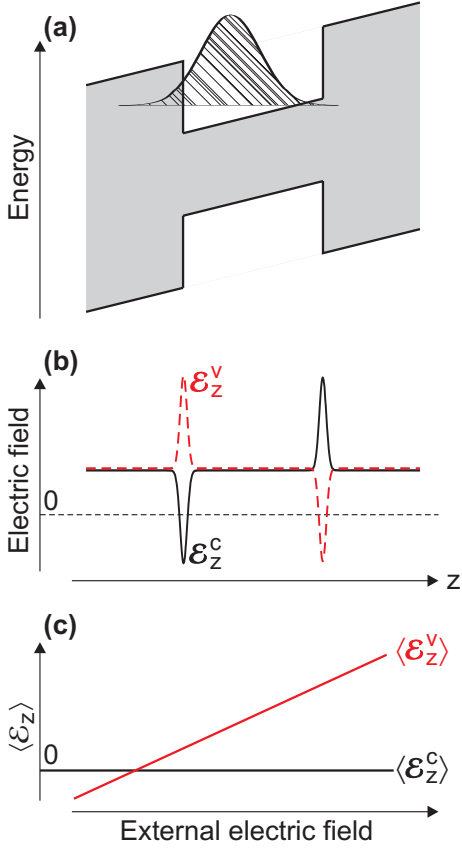


Figure C.3: (a) Conduction and valence band structure of a QW and (b) the resulting electric fields in the conduction and the valence band $\mathcal{E}_z^{c,v}$. The electron wave function in the conduction band arranges in z -direction, such that $\langle \mathcal{E}_z^c \rangle_c = 0$. In general, the relevant electric field in the valence band, however, $\langle \mathcal{E}_z^v \rangle_c \neq 0$. (c) An external electric field does not change $\langle \mathcal{E}_z^c \rangle_c$, but has a linear influence on $\langle \mathcal{E}_z^v \rangle_c$ (simulated data).

that the QW is properly contacted.

In summary, the measurements presented in this section indicate that tuning of the spin-orbit coupling with external gates is possible and can be measured. However, better samples with proper contacts to the QW are needed for further conclusions.

A further limitation of such measurements is the fact that the in-plane electric fields that induce the in-plane motion of the electrons should not be shielded. This requires the distance between a front and a back gate to be larger than the distance between the in-plane gate electrodes and limits the electric field that can be applied.

D Verification of the sample magnetization

To verify that the evaporated Fe of the samples used in chapter 3 and 4 is of good magnetic quality, we measured its magnetic moment in a *Vibrating Sample Magnetometer*. The magnetic sample is brought into sinusoidal motion in a homogeneous external magnetic field B_{ext} . Pick-up coils detect the change in magnetic flux that results from the sample's motion. By varying B_{ext} , the sample magnetization $M(B_{\text{ext}})$

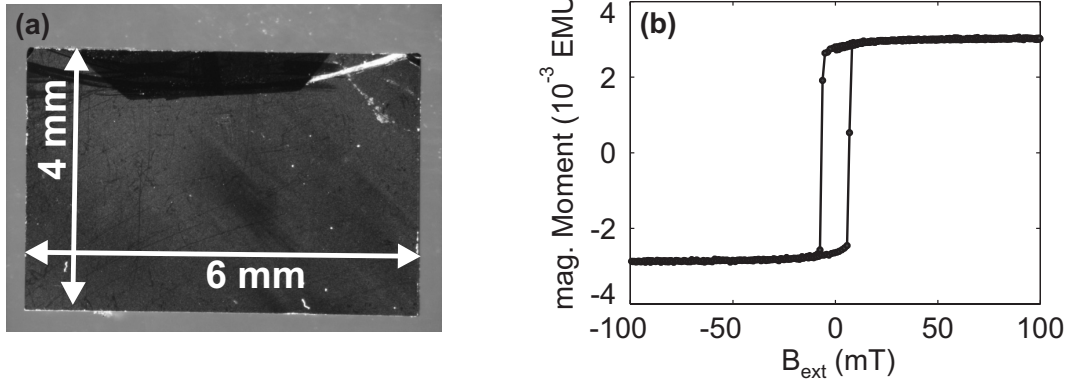


Figure D.4: (a) Sample used to measure the magnetization of evaporated Fe. (b) Measured magnetic moment, proportional to the sample magnetization, as a function of the applied external field.

can be measured.

Figure Da shows the sample, a 24.0 mm^2 large piece from wafer P805, onto which 10 nm Ti, 80 nm Fe and 10 nm Al were evaporated. The dark upper region is caused by the clamp that fixes the sample during the evaporation. In total, 21.8 mm^2 have been covered by 80 nm Fe, resulting in a volume of $V = 1.74 \times 10^{-6} \text{ cm}^3$. The magnetization per volume is the measured magnetic moment M_{EMU} , shown in Fig. Db, divided by the volume. It amounts to $M_s = 4\pi M_{\text{EMU}}/V = 21.6 \text{ kGauss}$ and compares well to the value $M_s = 21.4 \text{ kGauss}$ found in literature.

The coercive field of the film of $\approx 5 \text{ mT}$ is rather high and attributed to impurities on the substrate prior to the Fe evaporation. Such impurities can also lead to the observed slight ‘bending’ of the magnetic moment close to $B_{\text{ext}} = 0$ before the film switches its magnetization. Some magnetic moments have already rotated their orientation parallel to B_{ext} , but a further increase in B_{ext} is needed to make the magnetization along B_{ext} propagate through the film.

E List of samples

Abbreviations:

id. interdigitated
 std. gratings standard gratings: 3-3, 2-2, 1-1, 0.5-0.5
 trans. transparent

Name	Substrate	Description	Processed	First measured	Figures
4a	bulk n-GaAs	Gratings 3-1, 2-2, 2-1, 1-1; 10min RIE	13.09.04	15.09.04	
4b	040513A	Grating 1-1; 10min RIE	13.09.04	01.10.04	
5a	040513A	Gratings 2-1 Fe, 0.5-0.5 Au	05.11.04	13.12.04	
6a	040513A	Id. gratings, 7nm RIE	17.11.04	23.11.04	
6b	040513A	Id. gratings, 15nm RIE	17.11.04	06.12.04	
6c	040513A	Id. gratings, 50nm RIE	17.11.04	20.12.04	
8a	040513A	Id. gratings, partly ok	17.01.05	14.02.05	
8b	040513A	Id. gratings	17.01.05	18.01.05	
9b	P765	Id. gratings, non-polished sample back side	17.01.05	17.01.05	
10d	P765	Id. gratings, no Al cap	14.03.05	24.03.05	
14a	P805	Std. id. gratings: 3-3, 2-2, 1-1, 0.5-0.5, 10nm Ti, 80nm Fe or Au, 10nm Al	22.04.05	20.05.05	3.5, 3.6b, 3.8, 3.9, 3.12, 3.14, 3.16, 4.2, 4.3, A.1, A.2
14b	P805	Std. id. gratings	22.04.05	16.05.05	3.11, 4.1b
14c	P805	Std. id. gratings, mixed Fe/Au	22.04.05	06.06.05	4.2, 4.3
15a	P805	Trans. pads (100 × 100 μm); 7nm Ti, 7nm Au	22.04.05	25.04.05	
15b	P805	Trans. pads (100 × 100 μm); 7nm Ti, 7nm Fe, 2nm Al	22.04.05	25.04.05	
15c	P805	Trans. pads (100 × 100 μm); 7nm Fe, 2nm Al	22.04.05	11.05.05	
15d	P805	Trans. pads (100 × 100 μm); 7nm Fe	22.04.05	11.05.05	3.10
16a	P838	Std. id. gratings, partly ok	22.04.05		
17b	P838	Trans. pads (100 × 100 μm); 7nm Ti, 7nm Fe, 2nm Al	22.04.05		
17c	P838	Trans. pads (100 × 100 μm); 7nm Fe, 2nm Al	22.04.05		
17d	P838	Trans. pads (100 × 100 μm); 7nm Au	22.04.05		

18a	P805	Id. gratings, a = 2b	29.06.05	08.08.05	3.14
18b	P805	Id. gratings, a = 2b, mixed FeAu	29.06.05		
19a	P805	Id. gratings, a = 3b	29.06.05	10.08.05	3.14, 4.6
19b	P805	Id. gratings, a = 3b, mixed FeAu	29.06.05		
20d	P805	Horizontal and vertical gratings, all Fe, 3-3 and 2-2	29.06.05	03.08.05	3.15, 4.5
21a	P919	Std. id. gratings	29.06.05	23.08.05	2.13, 4.8, 4.9, 4.10
23a	P805	Horizontal and vertical gaps, 3, 2, 1, 0.5 μm , Fe	17.11.05	21.11.05	
23b	P805	Horizontal and vertical gaps, 3, 2, 1, 0.5 μm , Au	17.11.05		
24a	P805	Std. id. gratings, Ni instead of Fe	23.11.05	23.11.05	
25a	P805	Std. id. gratings, 27min RIE etch (90nm), NMP liftoff	13.01.06	23.01.06	3.17
25b	P805	Std. id. gratings, 27min RIE etch (90nm), Aceton liftoff	13.01.06	25.01.06	
25c	P805	Std. id. gratings, 27min RIE etch (90nm), mixed FeAu	13.01.06	09.02.06	
26a	ES865	Trans. top gate (3nm Ti, 7nm Au) and ohmic contacts to QW	14.06.06	22.06.06	
26b	ES866	Trans. top gate (3nm Ti, 7nm Au) and ohmic contacts to QW	14.06.06	21.06.06	2.17
27e	ES887	Std. id. gratings, only 2-2 working	18.10.06	01.11.06	
27f	ES887	Std. id. gratings, ICP etched, partly ok	18.10.06	02.11.06	
29b	P805	Std. id. gratings, ICP etched, partly ok	18.10.06	03.11.06	3.17
29g	P919	SO 4 gates, distance 100 μm	18.10.06	20.10.06	
30a	P919	SO 4 gates, $\theta = 0, 90^\circ$	07.11.06	13.11.06	5.2, 5.4 (sample 1), 5.10
30b	P919	SO 4 gates, $\theta = -45^\circ$	07.11.06	11.12.06	
30c	P919	SO 4 gates, $\theta = +45^\circ$	07.11.06	05.12.06	5.3, 5.8
30cBG	P919	30c with back gate	31.01.07	01.02.07	C.3
31a	ES887	SO 4 gates, $\theta = 180, 90^\circ$	20.11.06	27.11.06	5.4 (sample 3)
31b	P919	SO 4 gates, $\theta = 180, 90^\circ$	20.11.06	24.11.06	
31c	P805	SO 4 gates, $\theta = 180, 90^\circ$	20.11.06	29.11.06	5.4 (sample 2), 5.7

Publications

Measurement of Rashba and Dresselhaus spin-orbit magnetic fields

Lorenz Meier, Gian Salis, Ivan Shorubalko, Emilio Gini, Silke Schön and Klaus Ensslin

Nature Physics (2007)

Gate tunability of stray-field-induced electron spin precession in a GaAs/InGaAs quantum well below an interdigitated magnetized Fe grating

L. Meier, G. Salis, C. Ellenberger, E. Gini, and K. Ensslin

Phys. Rev. B **74**, 245318 (2006)

Stray-field induced modification of coherent spin dynamics

L. Meier, G. Salis, C. Ellenberger, E. Gini, and K. Ensslin

Appl. Phys. Lett. **88**, 172501 (2006)

Charge detection in quantum dots

R. Schleser, E. Ruh, L. Meier, A. Fuhrer, T. Ihn, K. Ensslin, D. D. Driscoll, A. C. Gossard, and W. Wegscheider

“Quantum Information and Decoherence in Nanosystems”, edited by C. Glattli, M. Sanquer and J. T. Thanh Van, THE GIOI Publishers, p. 161, 2005

Quantum physics in quantum rings

Thomas Ihn, Andreas Fuhrer, Lorenz Meier, Martin Sigrist, and Klaus Ensslin

Europhysics News 36, 78 (2005)

Single-Electron Effects in a Coupled Dot-Ring System

L. Meier, A. Fuhrer, T. Ihn, K. Ensslin, W. Wegscheider, and M. Bichler

Phys. Rev. B **69**, 241302 (2004)

Quantum Rings as Phase Coherent Detectors

A. Fuhrer, M. Sgrist, L. Meier, T. Ihn, K. Ensslin, W. Wegscheider and M. Bichler

Physica E 25, 303 (2004)

Masking by fast gratings

Meier, L., & Carandini, M.

Journal of Vision, 2(4):2, 293-301 (2002)

Bibliography

- [1] *International technology roadmap for semiconductors*, <http://www.itrs.net/>.
- [2] G. E. Moore, *Electronics Magazine* **38** (1965).
- [3] W. Pauli, *Z. Physik* **31**, 765ff (1925).
- [4] H.-A. Engel, P. Recher, and D. Loss, *Solid State Comm.* **119**, 229 (2001).
- [5] D. D. Awschalom, D. Loss, and N. Samarth, *Semiconductor spintronics and quantum computation*, Nanoscience and technology (Springer, 2002).
- [6] J. M. Elzerman, R. Hanson, L. H. W. V. Beveren, B. Witkamp, L. M. K. Vandersypen, and L. P. Kouwenhoven, *Nature* **430**, 431 (2004).
- [7] F. H. L. Koppens, J. A. Folk, J. M. Elzerman, R. Hanson, L. H. W. van Beveren, I. T. Vink, H. P. Tranitz, W. Wegscheider, L. P. Kouwenhoven, and L. M. K. Vandersypen, *Science* **309**, 1346 (2005).
- [8] F. H. L. Koppens, C. Buizert, K. J. Tielrooij, I. T. Vink, K. C. Nowack, T. Meunier, L. P. Kouwenhoven, and L. M. K. Vandersypen, *Nature* **442**, 766 (2006).
- [9] J. Berezovsky, M. H. Mikkelsen, O. Gywat, N. G. Stoltz, L. A. Coldren, and D. D. Awschalom, *Science* **314**, 1916 (2006).
- [10] M. Atatüre, J. Dreiser, A. Badolato, and A. Imamoglu, *Nature Phys.* **3**, 101 (2007).
- [11] M. N. Baibich, J. M. Broto, A. Fert, F. N. Van Dau, F. Petroff, P. Eitenne, G. Creuzet, A. Friederich, and J. Chazelas, *Phys. Rev. Lett.* **61**, 2472 (1988).
- [12] G. Binasch, P. Grünberg, F. Saurenbach, and W. Zinn, *Phys. Rev. B* **39**, 4828 (1989).
- [13] B. Dieny, V. S. Speriosu, S. S. P. Parkin, B. A. Gurney, D. R. Wilhoit, and D. Mauri, *Phys. Rev. B* **43**, 1297 (1991).

- [14] M. Jullière, Phys. Lett. A **54** (1975).
- [15] J. S. Moodera, L. R. Kinder, T. M. Wong, and R. Meservey, Phys. Rev. Lett. **74**, 3273 (1995).
- [16] D. Loss and D. P. DiVincenzo, Phys. Rev. A **57**, 120 (1998).
- [17] P. Shor, Foundations of Computer Science, 1994 Proceedings., 35th Annual Symposium on pp. 124–134 (1994).
- [18] R. de Sousa and S. Das Sarma, Phys. Rev. B **67**, 033301 (2003).
- [19] J. Preskill, Royal Society of London Proceedings Series A **454**, 385 (1998).
- [20] I. Žutić, J. Fabian, and S. Das Sarma, Rev. Mod. Phys. **76**, 323 (2004).
- [21] S. A. Wolf, D. D. Awschalom, R. A. Buhrman, J. M. Daughton, S. von Molnar, M. L. Roukes, A. Y. Chtchelkanova, and D. M. Treger, Science **294**, 1488 (2001).
- [22] D. D. Awschalom and M. E. Flatté, Nature Phys. **3**, 153 (2007).
- [23] G. Lampel, Phys. Rev. Lett. **20**, 491 (1968).
- [24] F. Meier, *Optical orientation* (North-Holland, 1984).
- [25] M. I. Dyakonov and V. I. Perel, in *Optical Orientation*, edited by F. Meier and B. Zakharchenya (North-Holland, 1984), pp. 11–71.
- [26] A. G. Aronov and G. E. Pikus, Soviet Physics - Semiconductors **10**, 698 (1976).
- [27] C.-M. Hu, J. Nitta, A. Jensen, J. B. Hansen, and H. Takayanagi, Phys. Rev. B **63**, 125333 (2001).
- [28] G. Schmidt, D. Ferrand, L. W. Molenkamp, A. T. Filip, and B. J. van Wees, Phys. Rev. B **62**, R4790 (2000).
- [29] M. Oestreich, J. Hubner, D. Hagele, P. J. Klar, W. Heimbrodtt, W. W. Ruhle, D. E. Ashenford, and B. Lunn, Appl. Phys. Lett. **74**, 1251 (1999).
- [30] R. Fiederling, M. Keim, G. Reuscher, W. Ossau, G. Schmidt, A. Waag, and L. W. Molenkamp, Nature **402**, 787 (1999).
- [31] Y. Ohno, D. K. Young, B. Beschoten, F. Matsukura, H. Ohno, and D. D. Awschalom, Nature **402**, 790 (1999).
- [32] H. Ohno, Science **281**, 951 (1998).
- [33] S. F. Alvarado and P. Renaud, Phys. Rev. Lett. **68**, 1387 (1992).

- [34] X. Jiang, R. Wang, R. M. Shelby, R. M. Macfarlane, S. R. Bank, J. S. Harris, and S. S. P. Parkin, *Phys. Rev. Lett.* **94**, 056601 (2005).
- [35] G. Salis, R. Wang, X. Jiang, R. M. Shelby, S. S. P. Parkin, S. R. Bank, and J. S. Harris, *Appl. Phys. Lett.* **87**, 262503 (2005).
- [36] R. R. Parsons, *Phys. Rev. Lett.* **23**, 1152 (1969).
- [37] X. Lou, C. Adelmann, S. A. Crooker, E. S. Garlid, J. Zhang, K. S. M. Reddy, S. D. Flexner, C. J. Palmstrom, and P. A. Crowell, *Nature Phys.* **3**, 197 (2007).
- [38] J. Fabian and S. D. Sarma (AVS, 1999), vol. 17, pp. 1708–1715.
- [39] Y. Yafet, in *Solid State Physics, Vol. 14*, edited by F. Seitz and D. Turnbull (Academic Press, New York, 1963).
- [40] R. J. Elliott, *Phys. Rev.* **96**, 266 (1954).
- [41] M. I. D’Yakonov and V. I. Perel’, *Sov. Phys. Solid State* **13**, 3023 (1971).
- [42] G. Bir, A. Aronov, and G. Pikus, *Soviet Physics JETP* **42**, 705 (1975).
- [43] J. M. Kikkawa and D. D. Awschalom, *Phys. Rev. Lett.* **80**, 4313 (1998).
- [44] R. I. Dzhioev, K. V. Kavokin, V. L. Korenev, M. V. Lazarev, B. Y. Meltser, M. N. Stepanova, B. P. Zakharchenya, D. Gammon, and D. S. Katzer, *Phys. Rev. B* **66**, 245204 (2002).
- [45] A. Malinowski, R. S. Britton, T. Grevatt, R. T. Harley, D. A. Ritchie, and M. Y. Simmons, *Phys. Rev. B* **62**, 13034 (2000).
- [46] Y. Ohno, R. Terauchi, T. Adachi, F. Matsukura, and H. Ohno, *Phys. Rev. Lett.* **83**, 4196 (1999).
- [47] S. Datta and B. Das, *Appl. Phys. Lett.* **56**, 665 (1990).
- [48] H. W. Jiang and E. Yablonovitch, *Phys. Rev. B* **64**, R41307 (2001).
- [49] G. Salis, Y. Kato, K. Ensslin, D. C. Driscoll, A. C. Gossard, and D. D. Awschalom, *Nature* **414**, 619 (2001).
- [50] J. Jackson, *Classical Electrodynamics* (Wiley, 1998).
- [51] G. Dresselhaus, *Phys. Rev.* **100**, 580 (1955).
- [52] E. Rashba, *Soviet Physics - Solid State* **2**, 1109 (1960).
- [53] Y. A. Bychkov and E. I. Rashba, *J. Phys. C* **17**, 6039 (1984).
- [54] J. Schliemann, J. C. Egues, and D. Loss, *Phys. Rev. Lett.* **90**, 146801 (2003).

- [55] L. Viña, L. Muñoz, E. Pérez, J. Fernández-Rossier, C. Tejedor, and K. Ploog, *Phys. Rev. B* **54**, R8317 (1996).
- [56] A. V. Kimel, F. Bentivegna, V. N. Gridnev, V. V. Pavlov, R. V. Pisarev, and T. Rasing, *Phys. Rev. B* **63**, 235201 (2001).
- [57] M. Oestreich and W. W. Rühle, *Phys. Rev. Lett.* **74**, 2315 (1995).
- [58] D. A. B. Miller, D. S. Chemla, D. J. Eilenberger, P. W. Smith, A. C. Gossard, and W. T. Tsang, *Appl. Phys. Lett.* **41**, 679 (1982).
- [59] L. van der Pauw, *Philips Tech. Rev* **20**, 220 (1958).
- [60] U. Wahlen, RIE-Ätzen von dünnen Streifen in GaAs, Semesterarbeit ETH Zürich (2007).
- [61] R. Engel-Herbert and T. Hesjedal, *J. Appl. Phys.* **97**, 074504 (2005).
- [62] Y. Martin and H. K. Wickramasinghe, *Appl. Phys. Lett.* **50**, 1455 (1987).
- [63] A. M. Chang, H. D. Hallen, L. Harriott, H. F. Hess, H. L. Kao, J. Kwo, R. E. Miller, R. Wolfe, J. van der Ziel, and T. Y. Chang, *Appl. Phys. Lett.* **61**, 1974 (1992).
- [64] H. Schömig, A. Forchel, S. Halm, G. Bacher, J. Puls, and F. Henneberger, *Appl. Phys. Lett.* **84**, 2826 (2004).
- [65] M. Sakuma, K. Hykomi, I. Souma, A. Murayama, and Y. Oka, *Appl. Phys. Lett.* **85**, 6203 (2004).
- [66] M. Sakuma, K. Hyomi, I. Souma, A. Murayama, and Y. Oka, *J. Appl. Phys.* **94**, 6423 (2003).
- [67] J. Kossut, I. Yamakawa, A. Nakamura, G. Cywiński, K. Fronc, M. Czczcott, J. Wróbel, F. Kyrychenko, T. Wojtowicz, and S. Takeyama, *Appl. Phys. Lett.* **79**, 1789 (2001).
- [68] P. Redliński, T. Wojtowicz, T. G. Rappoport, A. Libal, J. K. Furdyna, and B. Jankó, *Phys. Rev. B* **72**, 085209 (2005).
- [69] P. A. Crowell, V. Nikitin, D. D. Awschalom, F. Flack, N. Samarth, and G. A. Prinz, *J. Appl. Phys.* **81**, 5441 (1997).
- [70] Y. Kato, R. C. Myers, D. C. Driscoll, A. C. Gossard, J. Levy, and D. D. Awschalom, *Science* **299**, 1201 (2003).
- [71] Y. Kato, R. C. Myers, A. C. Gossard, and D. D. Awschalom, *Nature* **427**, 50 (2004).

- [72] Y. Tokura, W. G. van der Wiel, T. Obata, and S. Tarucha, Phys. Rev. Lett. **96**, 047202 (2006).
- [73] <http://math.nist.gov/oommf/>.
- [74] <http://www.activestate.com/Products/ActiveTcl/>.
- [75] T. Gilbert, Phys. Rev. **100**, 1243 (1955).
- [76] D. Craik and R. Tebble, *Ferromagnetism and ferromagnetic domains*, vol. IV of *Selected topics in solid state physics* (North-Holland, 1965).
- [77] D. Paget, G. Lampel, B. Sapoval, and V. I. Safarov, Phys. Rev. B **15**, 5780 (1977).
- [78] J. M. Kikkawa and D. D. Awschalom, Science **287**, 473 (2000).
- [79] G. Salis, D. D. Awschalom, Y. Ohno, and H. Ohno, Phys. Rev. B **64**, 195304 (2001).
- [80] R. K. Kawakami, Y. Kato, M. Hanson, I. Malajovich, J. M. Stephens, E. Johnston-Halperin, G. Salis, A. C. Gossard, and D. D. Awschalom, Science **294**, 131 (2001).
- [81] R. J. Epstein, I. Malajovich, R. K. Kawakami, Y. Chye, M. Hanson, P. M. Petroff, A. C. Gossard, and D. D. Awschalom, Phys. Rev. B **65**, 121202 (2002).
- [82] J. Stephens, R. K. Kawakami, J. Berezovsky, M. Hanson, D. P. Shepherd, A. C. Gossard, and D. D. Awschalom, Phys. Rev. B **68**, 041307 (2003).
- [83] C. Ciuti, J. P. McGuire, and L. J. Sham, Appl. Phys. Lett. **81**, 4781 (2002).
- [84] J. P. McGuire, C. Ciuti, and L. J. Sham, Phys. Rev. B **69**, 115339 (2004).
- [85] T. W. Ebbesen, H. T. Lezec, H. F. Ghaemi, T. Thio, and P. A. Wolff, Nature **391**, 667 (1998).
- [86] U. Schröter and D. Heitmann, Phys. Rev. B **58**, 15419 (1998).
- [87] I. Y. Gerlovin, Y. K. Dolgikh, S. A. Eliseev, V. V. Ovsyankin, Y. P. Efimov, I. V. Ignatiev, V. V. Petrov, S. Y. Verbin, and Y. Masumoto, Phys. Rev. B **69**, 035329 (2004).
- [88] F. A. Baron, A. A. Kiselev, H. D. Robinson, K. W. Kim, K. L. Wang, and E. Yablonovitch, Phys. Rev. B **68**, 195306 (2003).
- [89] E. L. Ivchenko, A. A. Kiselev, and M. Willander, Solid State Comm. **102**, 375 (1997).

- [90] B. J. van Wees, H. van Houten, C. W. J. Beenakker, J. G. Williamson, L. P. Kouwenhoven, D. van der Marel, and C. T. Foxon, *Phys. Rev. Lett.* **60**, 848 (1988).
- [91] R. Winkler, *Spin-Orbit Coupling Effects in Two-Dimensional Electron and Hole Systems*, vol. 191/2003 of *Springer Tracts in Modern Physics* (Springer, 2003).
- [92] G. Lommer, F. Malcher, and U. Rossler, *Phys. Rev. Lett.* **60**, 728 (1988).
- [93] J. Luo, H. Munekata, F. F. Fang, and P. J. Stiles, *Phys. Rev. B* **41**, 7685 (1990).
- [94] J. Nitta, T. Akazaki, H. Takayanagi, and T. Enoki, *Phys. Rev. Lett.* **78**, 1335 (1997).
- [95] T. Schapers, G. Engels, J. Lange, T. Klocke, M. Hollfelder, and H. Luth, *J. Appl. Phys.* **83**, 4324 (1998).
- [96] B. Das, D. C. Miller, S. Datta, R. Reifenberger, W. P. Hong, P. K. Bhattacharya, J. Singh, and M. Jaffe, *Phys. Rev. B* **39**, 1411 (1989).
- [97] G. Engels, J. Lange, T. Schäpers, and H. Lüth, *Phys. Rev. B* **55**, R1958 (1997).
- [98] C.-M. Hu, J. Nitta, T. Akazaki, H. Takayanagi, J. Osaka, P. Pfeffer, and W. Zawadzki, *Phys. Rev. B* **60**, 7736 (1999).
- [99] P. Pfeffer and W. Zawadzki, *Phys. Rev. B* **59**, R5312 (1999).
- [100] S. Brosig, K. Ensslin, R. J. Warburton, C. Nguyen, B. Brar, M. Thomas, and H. Kroemer, *Phys. Rev. B* **60**, R13989 (1999).
- [101] T. Koga, J. Nitta, T. Akazaki, and H. Takayanagi, *Phys. Rev. Lett.* **89**, 046801 (2002).
- [102] S. D. Ganichev, V. V. Bel'kov, L. E. Golub, E. L. Ivchenko, P. Schneider, S. Giglberger, J. Eroms, J. D. Boeck, G. Borghs, W. Wegscheider, et al., *Phys. Rev. Lett.* **92**, 256601 (2004).
- [103] J. B. Miller, D. M. Zumbühl, C. M. Marcus, Y. B. Lyanda-Geller, D. Goldhaber-Gordon, K. Campman, and A. C. Gossard, *Phys. Rev. Lett.* **90**, 076807 (2003).
- [104] D. Grundler, *Phys. Rev. Lett.* **84**, 6074 (2000).
- [105] J. P. Heida, B. J. van Wees, J. J. Kuipers, T. M. Klapwijk, and G. Borghs, *Phys. Rev. B* **57**, 11911 (1998).

- [106] T. Matsuyama, R. Kürsten, C. Meißner, and U. Merkt, *Phys. Rev. B* **61**, 15588 (2000).
- [107] V. Kalevich and V. Korenev, *JETP Lett.* **52**, 230 (1990).
- [108] S. A. Crooker and D. L. Smith, *Phys. Rev. Lett.* **94**, 236601 (2005).
- [109] Y. K. Kato, R. C. Myers, A. C. Gossard, and D. D. Awschalom, *Phys. Rev. Lett.* **93**, 176601 (2004).
- [110] H.-A. Engel, E. I. Rashba, and B. I. Halperin, *Phys. Rev. Lett.* **98**, 036602 (2007).
- [111] S. Ganichev and W. Prettl, *J. Phys.: Condens. Matter* **15**, R935 (2003).
- [112] A. Bournel, *Ann. Phys. Fr* **25**, 1 (2000).
- [113] R. Lassnig, *Phys. Rev. B* **31**, 8076 (1985).
- [114] N. W. Ashcroft and D. N. Mermin, *Solid State Physics* (Brooks Cole, 1976), ISBN 0030839939.
- [115] M. Duckheim and D. Loss, *Nature Phys.* **2**, 195 (2006).
- [116] F. Bloch and A. Siegert, *Phys. Rev.* **57**, 522 (1940).
- [117] Y. K. Kato, R. C. Myers, A. C. Gossard, and D. D. Awschalom, *Appl. Phys. Lett* **86**, 162107 (2005).
- [118] M. Duckheim and D. Loss, *Phys. Rev. B* **75**, 201305(R) (2007).
- [119] D. A. B. Miller, D. S. Chemla, T. C. Damen, A. C. Gossard, W. Wiegmann, T. H. Wood, and C. A. Burrus, *Phys. Rev. B* **32**, 1043 (1985).
- [120] S. Zimmermann, A. Wixforth, J. P. Kotthaus, W. Wegscheider, and M. Bichler, *Science* **283**, 1292 (1999).

Acknowledgements

It started with an empty lab in Rüschtikon and ended with this small book. During the time in-between, many people have contributed to the results presented in this thesis and they have helped to make the three years I have spent with this work to be three pleasant and interesting years. First of all, I thank *Gian Salis* for being an enthusiastic and patient supervisor whom I could ask anytime what was on my mind and with whom I remember countless discussions in our office L220, be they about physics, politics or mountains... I thank *Klaus Ensslin* for offering me the possibility of getting back to nano-science after my short excursion into the world of kilovolts and megawatts. It was always with pleasure that I went to his office on Höggerberg, to discuss new results and failures, and I returned with plenty of new ideas, insights and fresh motivation to the lab in Rüschtikon. I thank *Atac Imamoglu* for accepting to co-examine this thesis.

I thank *Christoph Ellenberger* for countless hours at the e-beam. He always found a free time-slot in the booking system and his personal schedule to write new samples for me. I thank *Ivan Shorubalko* who took over this job afterwards, with as much commitment. I thank *Renaud Leturcq* for many evaporations and I thank *Boris Grbic* for processing Hall bar samples to characterize newly grown wafers. I thank *Thomas Ihn*, who sometimes was my last rescue in understanding mysterious measurements. And I thank *Paul Studerus*, without his help in designing the electronics and his common sense, which is still valid at GHz-frequencies, these measurements would not have been possible. I thank all the members of the Nanophysics group who are responsible for the fact that I always enjoyed coming to Höggerberg. In particular, I thank *Davy Graf*, *Boris Grbic* and *Arnd Gildemeister* for the good time together when writing down the theses.

I thank the people from the ETH-cleanroom ‘FIRST’ for assistance, the experiments presented would not have been possible without the wafers grown by *Emilio Gini* (MOCVD), *Silke Schön*, *Stefan Fälth* and *Antonio Badolato* (MBE). I thank *Otte Homan* for help in many small concerns and questions, *Patric Strasser* for introducing me to ICP etching, and *Ueli Wahlen* for the etching-recipe he developed during his semester thesis.

In Rüschtikon, I thank *Martin Witzig* for bonding my samples and providing the lab with electronic devices often within minutes. I thank *Meinrad Tschudy* for the

evaporation of Fe, *Niko Moll* for the optical simulations of the QW illuminations, and *Rainer Mahrt*, besides optical advice, for a few screws that I was allowed to borrow from his lab.

I thank *Pierre-Olivier Jubert* for the introduction in OOMMF he gave to me and for the first simulations he calculated. And I thank my manager *Rolf Allenspach* for giving un-biased advice, even on his manager-free days, as well as for quickly approving almost all of my material requests.

I thank *International Business Machines* for providing the lab space with plenty of expensive equipment, a very good cafeteria and regularly new buzzwords.

Finally, I thank the *LutherWG* for being a place I always looked forward going home to, and in particular *Patrick Maletinsky* for the kitchen discussions and for his feedback on some of my manuscripts.

And I thank Sarah ♡

Curriculum Vitae

Name: Lorenz Meier
born: March 11, 1977 in Uzwil (SG)
citizen of Bülach (ZH)

Contact: lome@gmx.ch

- 1984-1990 Primary School in Henau (SG)
- 1990-1992 Secondary School in Uzwil (SG)
- 1992-1997 Kantonsschule St. Gallen, Matura Typ C
- 1994-2003 Employment at the tax administration of the canton of St. Gallen (part time 20-30%). Programming of software for tax calculation and staff management. Tax revenue simulations.
- 10/1997-03/2003 Physics studies at ETH Zurich and at Lund's Universitet, Sweden (08/1999-03/2001)
Diploma thesis: *Single-Electron Effects in a Coupled Quantum Ring – Quantum Dot System* in the group of Prof. K. Ensslin
- 07/2003-02/2004 Swiss Federal Railways (SBB), Infrastructure Division, I-ETCS. Implementation and test of the braking parameters for a new high speed train line running with the European Train Control System.
- 03/2004-06/2007 PhD thesis in a joint research project between the IBM Zurich Research Lab and the Laboratory for Solid State Physics at ETH.

This thesis presents experimental data on the manipulation of quantum-well electron spins. On the one hand, spin manipulation by the use of magnetic stray fields from small, magnetized Fe gates is considered. Such stray fields are strongly inhomogeneous and can reach values of the order of 1 Tesla. On the other hand, the manipulation of spins with electric fields is investigated. Through the effect of spin-orbit interaction, moving electrons perceive electric as magnetic fields, which couple to the spin.

This work was supported by the IBM Zurich Research Laboratory, the Laboratory for Solid State Physics at ETH Zurich and the National Center of Competence in Research “Nanoscale Science” (NCCR nano).

